

**Volatile degassing and plinian eruption  
dynamics of the mafic Fontana Tephra,  
Nicaragua**

Kumulative Dissertation  
zur Erlangung des Doktorgrades  
der Mathematisch-Naturwissenschaftlichen Fakultät  
der Christian-Albrechts-Universität  
zu Kiel

Heidi Wehrmann

Kiel 2005

Referent: PD Dr. Armin Freundt

Korreferent: Prof. Dr. Kaj Hoernle

Tag der mündlichen Prüfung: 30.05.2005

Zum Druck genehmigt

Der Dekan

## Preface

This thesis comprises three independent publications that are submitted for publication, or in preparation for submission to international journals or special papers. They may therefore be subject to revision. Each publication contains its own abstract, introduction, description of methods, data presentation, discussion, conclusion, and reference list. The three papers are:

1. Fontana Tephra: a basaltic plinian eruption in Central Nicaragua;  
by Heidi Wehrmann, Costanza Bonadonna, Armin Freundt, Bruce F. Houghton, Steffen Kutterolf; submitted to Rose, W.I. (ed.): Volcanic Hazards in Central America, Geologic Society of America Special Paper
2. Water, halogen, and sulphur degassing of the basaltic-andesitic Fontana Tephra, Nicaragua;  
by Heidi Wehrmann, Armin Freundt, Steffen Kutterolf, Michael Wiedenbeck, Hans-Ulrich Schmincke; prepared for submission to Journal of Volcanology and Geothermal Research
3. Bromine and iodine in volcanic glasses determined by Synchrotron-XRF: origin and partitioning in basaltic-andesitic and rhyolitic arc magma systems;  
by Heidi Wehrmann and Armin Freundt; submitted to Chemical Geology

For these publications I carried out comprehensive field work in Nicaragua during four campaigns of durations between two weeks and three months, including extensive isopach and isopleth mapping, stratigraphic compilations, and sampling; did sample preparation and conducted measurement campaigns for electron microprobe analyses, ion microprobe analyses, X-ray fluorescence analyses, synchrotron-X-ray fluorescence analyses, ICP-MS analyses; processed the data; and prepared the manuscripts. While this thesis is focussed on the mafic Fontana Tephra, I am also preparing a publication on the physical and chemical aspects of the rhyolitic Upper Apoyeque Tephra.

Next to the work presented in this thesis, I cooperated with other members of the Sonderforschungsbereich 574, subproject C4, in establishing a regional stratigraphic framework of widespread tephras in west-central Nicaragua and mapping

of these deposits. I thereby contributed to the following submitted papers and to publications in preparation:

1. Onshore to offshore tephrostratigraphy and marine ash layer diagenesis in Central America;  
by Steffen Kutterolf, Ulrike Schacht, Heidi Wehrmann, Armin Freundt, Tobias Mörz; In: Alvarado, G. and Buntschuh, J. (eds.) (2004): Central America - Geology, Resources, and Hazards. Balkema (Lisse, Niederlande, Tokio, Japan)
2. Tsunami generated by a compositionally zoned plinian eruption at Chiltepe Peninsula, Lake Managua (Xolotlan), Nicaragua;  
by Armin Freundt, Steffen Kutterolf, Heidi Wehrmann, Hans-Ulrich Schmincke, Wilfried Strauch; submitted to Journal of Volcanology and Geothermal Research
3. 40,000 years of highly explosive eruptions around Managua, Nicaragua: time sequence, eruption dynamics, and hazard implications;  
by Steffen Kutterolf, Armin Freundt, Heidi Wehrmann, Wendy Perez, Hans-Ulrich Schmincke, Wilfried Strauch; in prep.

## Abstract

Fontana Tephra, erupted in the Late-Pleistocene from the Masaya area, west-central Nicaragua at the Central American subduction zone, is a widespread basaltic-andesitic scoria fallout fan reaching several metres thickness. Eruptive episodes of plinian fallout activity, alternating with phreatomagmatically-affected plinian and subplinian phases are reflected in a sequence of beds of the deposit. For the plinian eruptive phases, volumes, eruption column heights, and wind speeds were calculated for three different vent scenarios, since the exact vent site could not be localised. The minimum estimate of the total erupted tephra volume amounts to 1.4 to 1.8 km<sup>3</sup> (1.1 to 1.4 Gt DRE). This is much lower than in previous studies which were based on less detailed mapping and affected by erroneous stratigraphic correlations. Comparison of tephra dispersal parameters with theoretical modelling results suggest eruption column heights between 24 and 30 km. As different approaches to determine column heights produce compatible results, these models, although originally designed for rhyolitic plinian eruptions, appear to be applicable to mafic plinian eruptions.

The petrologic method determines the mass fraction of volatiles degassed during eruption as the concentration difference between undegassed melt inclusions in minerals and degassed matrix glass. Volatile concentrations in those melt inclusions and matrix glasses were measured by Secondary Ion Mass Spectrometry (SIMS) and synchrotron-XRF (SyXRF). These are the most precise, and for some elements the only methods but are very time-consuming and require previous electron microprobe analyses. The number of samples analysed is limited by the available measurement times. Scaling the analytical results to the erupted magma masses yields emission of volatiles during the plinian and subplinian phases of the Fontana eruption of 7 Mt H<sub>2</sub>O, 30 kt F, 160 kt Cl, 280 kt S (by SIMS), and 32 kt I (by SyXRF). The gas release varies in the successive eruptive episodes, but shows an overall increase towards later phases of the eruption. The F and Cl release correlates with the water degassing, allowing to calculate fluid-melt distribution coefficients ( $D^{f/m}$ ) - which were, in other studies, mostly determined experimentally - directly in this natural system using the analytical results. For the eruptive phases,  $D^{f/m}$  is 12–18 for F and 7–30 for Cl; while I shows a  $D^{f/m}$ -value of c. 1700 for the entire eruption.

Degassing of scoria practically terminates upon magma fragmentation in the conduit. Scoria vesicularities of 68–72 % yield a fragmentation pressure of 4.5–5.3 MPa (165–195 m depth) when assuming equilibrium degassing, whereas the residual melt water contents of 0.2–0.5 wt.% point to considerably lower fragmentation pressures of 0.8–4.0 MPa (30–150 m depth). This offset suggests a retarded disequilibrium degassing during magma ascent in the conduit, invoked by a predominantly homogeneous bubble nucleation, for which a substantial volatile supersaturation is required. The scarcity of suitable microlites in the melt, which would have acted as bubble nucleation sites, supports this delayed water exsolution. The late, catastrophic bubble nucleation and expansion may have been the reason for the mafic Fontana magma to erupt in its unusual plinian style. Such an eruptive style is more typical of felsic magmas where it is attributed to overpressure building up as bubble expansion is hindered by high viscosity. Such a model is clearly not applicable to the low viscosity mafic Fontana magma.

Insight into material transfer through the Central American subduction zone is provided by SyXRF measurement results of glasses of Fontana Tephra and the younger rhyolitic Upper Apoyeque Tephra. Both tephtras show high concentrations of Br and I. As the Earth's mantle is too depleted in these elements to explain the high observed concentrations in the melt, it is inferred that they are derived predominantly from a marine sediment source. Hence the high concentrations of heavy halogens, and their covariance with high Ba-La ratios, which are proxies of slab-sediment contribution, indicate significant input of marine sediments into the Central Nicaraguan segment of the subduction zone, where they strongly contaminate the mantle-wedge source of the magma.

## **Zusammenfassung**

Diese Dissertation beleuchtet in erster Linie den spätpleistozänen Vulkanausbruch der basaltisch-andesitischen Fontana Tephra, im Hinblick auf Eruptionsstile und -parameter, Gasfreisetzungsprozesse und deren Interaktion mit Schlotverhältnissen. Darüber hinaus beinhaltet sie einige Aspekte über den Kreislauf schwerer Halogene durch die Mittelamerikanische Subduktionszone, die - neben Fontana Tephra - auch an der rhyolitischen Oberen Apoyeque Tephra manifestiert werden.

Die basaltisch-andesitische Fontana Tephra entstand im späten Pleistozän durch einen hochexplosiven, plinianischen Vulkanausbruch in der Gegend von Masaya im westlichen Mittelnicaragua. Dieses Gebiet gehört zu der Mittelamerikanischen Subduktionszone, in der sich die Kokosplatte unter die Karibische Platte schiebt. Diese erosive Subduktionszone gehört zu den aktivsten der Erde. Die Fontanaeruption bestand aus mehreren Phasen plinianischer und subplinianischer Falloutaktivität, von denen zahlreiche Schübe zu variablem Grad phreatomagmatisch beeinflusst waren. Da die Geländedaten keine exakte Lokalisierung des Vulkanzentrums zulassen, wurden Volumina eruptierter Tephra der einzelnen plinianischen Fallschichten, sowie die zugehörigen Eruptionssäulenhöhen und Windgeschwindigkeiten während der Eruption für drei verschiedene Szenarien möglicher bzw. theoretischer Schlotlokalitäten berechnet. Das eruptierte Volumen liegt zwischen mindestens 1,4 und 1,8 km<sup>3</sup>. Die Eruptionssäulen erreichten 24 bis 30 km Höhe während der plinianischen Phasen. Diese Berechnung beruht auf Vergleichen der Ablagerungsfächergeometrien der maximalen Korngrößen mit bestehenden Tephraverteilungsmodellen. Diese Modelle sind ursprünglich für rhyolitische plinianische Eruptionen entwickelt worden. Dass die Ergebnisse verschiedener dieser Modelle im Rahmen der erzielbaren Genauigkeit übereinstimmen, zeigt, dass sie auch für mafische plinianische Eruptionen anwendbar sind.

Zur Quantifizierung der Gase, die während der Fontanaeruption freigesetzt wurden, sowie um Einblicke in die damit verbundene Prozesse zu erhalten, wurden Volatile in Schmelzinklusiven in Mineralen und in Matrixgläsern der Schlackeklasten gemessen: Wasser-, Fluor-, Chlor- und Schwefelkonzentrationen wurden per Sekundärionenmassenspektrometrie (SIMS) bestimmt, Brom und Jod durch Synchrotronröntgenfluoreszenz (SyXRF). Diese Methoden sind die präzisesten bzw.

für einige Elemente die einzig möglichen. Sie erfordern jedoch vorherige Elektronenmikrosondenanalysen und sind sehr zeitaufwändig, daher ist die Anzahl der analysierten Proben durch die verfügbare Messzeit begrenzt.

Während der plinianischen und subplinianischen Phasen der Fontanaeruption wurden ungefähr 7 Mt H<sub>2</sub>O, 30 kt F, 160 kt Cl, 280 kt S und 32 kt I emittiert. Die Gasfreisetzung verläuft nicht gleichmäßig in den verschiedenen Eruptionsphasen, steigt tendenziell jedoch mit dem Fortschreiten der Eruption an. Die Freisetzung von F und Cl korreliert mit der Wasserfreisetzung. Daraus ergeben sich Partitionskoeffizienten von der Schmelze in die Fluidphase ( $D^{f/m}$ ) von 12–18 für F und 7–30 für Cl; I zeigt für die Gesamteruption einen  $D^{f/m}$ -Wert von etwa 1700.

Der Fragmentationsdruck im Schlot, abgeleitet von den residualen Wassergehalten im Matrixglas der Schlacke, fluktuierte zwischen 0,8 und 4,0 MPa, entsprechend einer Fragmentationstiefe von 30 und 150 m unter der Oberfläche. Im Gegensatz dazu impiziert die Porosität der Schlackeklasten von 68–72 % einen größeren Fragmentationsdruck von 4,5–5,3 MPa (165–195 m), sofern eine Gleichgewichtsentgasung stattfand. Diese Diskrepanz deutet auf eine verspätete Entgasung im Ungleichgewicht zu den Druckverhältnissen im Schlot hin, die durch eine homogenen Blasenbildung in Verbindung mit einer substanziellen Volatilenübersättigung erzwungen wurde. Die Theorie wird untermauert durch die geringe Menge von Mikroliten in der Schmelze, die geeignete Blasenkeime zur Verfügung gestellt hätten. Diese verzögerte, plötzliche Blasenbildung in Verbindung mit dem schnell aufsteigenden Magma war möglicherweise der Grund für das untypische plinianische Verhalten des mafischen Magmas der Fontanaeruption.

Einen Einblick in magmagenetische Prozesse an der Nicaraguanischen Vulkanfront wurde darüber hinaus durch Brom- und Jodkonzentrationen in Schmelzeinklusiven und Matrixgläsern sowohl von der Fontanaeruption, wie auch von der Eruption der rhyolitischen Oberen Apoyeque Tephra vom Chiltepe Vulkankomplex ermöglicht. Beide Tephras weisen hohe Konzentrationen der schweren Halogene auf. Da der Erdmantel im Hinblick auf diese beiden Elemente stark abgereichert ist, kann gefolgert werden, dass das Br und I aus marinen Sedimenten stammt, die generell Br und I in relativ hohen Konzentrationen enthalten. Die hohen Brom- und Jodgehalte, sowie deren Korrelation mit den Ba-La Verhältnissen, welche als



Indikatoren für Sedimentsubduktion gelten, deuten darauf hin, dass beträchtliche Mengen von Sediment durch das Nicaraguanische Segment der Mittelamerikanischen Subduktionszone recycled werden.

# Contents

<b>1</b>	<b>Introduction</b>	<b>1</b>
1.1	Introduction . . . . .	2
1.1.1	Location and geologic setting . . . . .	2
1.1.2	Subduction zone volcanism . . . . .	2
1.1.3	Climatic impact of explosive volcanism . . . . .	4
1.2	Objectives of this study . . . . .	4
1.2.1	Mafic plinian volcanism - poorly understood . . . . .	4
1.2.2	Element recycling through the subduction zone . . . . .	5
1.3	Thesis outline . . . . .	6
<b>2</b>	<b>Fontana Tephra: a basaltic plinian eruption in Nicaragua</b>	<b>10</b>
2.1	Introduction . . . . .	12
2.1.1	Mafic plinian volcanism . . . . .	12
2.1.2	Geologic setting and previous work on Fontana Tephra . . . . .	13
2.2	Fontana Tephra . . . . .	15
2.3	Distribution of depositional units . . . . .	20
2.4	Evolution of the Fontana eruption . . . . .	25
2.4.1	Variations in eruptive style . . . . .	25
2.4.2	Erupted volumes . . . . .	26
2.4.3	Eruption column heights and wind speeds . . . . .	28
2.5	Discussion and conclusion . . . . .	32
2.5.1	Applicability of eruption models . . . . .	32
2.5.2	Conclusions . . . . .	34
<b>3</b>	<b>Water, halogen, and sulphur degassing during the basaltic-andesitic plinian eruption of Fontana Tephra, Nicaragua</b>	<b>42</b>
3.1	Introduction . . . . .	44

3.1.1	Volatiles . . . . .	44
3.1.2	The Fontana eruption . . . . .	44
3.2	Methods . . . . .	45
3.2.1	Sampling and sample preparation . . . . .	45
3.2.2	Electron microprobe analyses (EMA) . . . . .	47
3.2.3	Secondary ion mass spectrometry (SIMS) . . . . .	47
3.3	Volatiles . . . . .	48
3.3.1	Melt composition and crystallinity . . . . .	48
3.3.2	Quantification of volatile release . . . . .	49
3.4	Volatile solubility and exsolution conditions . . . . .	52
3.4.1	Magma chamber conditions - temperature and pressure . . . . .	53
3.4.2	Water saturated reservoir? . . . . .	54
3.4.3	Fluorine release? . . . . .	55
3.4.4	Chlorine partitioning . . . . .	55
3.4.5	Excess sulphur? . . . . .	56
3.5	Eruption dynamics . . . . .	58
3.5.1	Homogeneous versus heterogeneous bubble nucleation . . . . .	58
3.5.2	Scoria porosity and fragmentation depth . . . . .	59
3.5.3	Residual water and fragmentation depth . . . . .	59
3.5.4	Causes of the plinian style of the basaltic-andesitic eruption . . . . .	62
3.6	Conclusions . . . . .	64
<b>4</b>	<b>Bromine and iodine concentrations in volcanic glasses determined by Synchrotron-XRF: origin and partitioning of heavy halogens in basaltic- andesitic and rhyolitic arc magma systems</b>	<b>70</b>
4.1	Introduction . . . . .	72
4.2	Geologic setting . . . . .	72
4.3	Methods . . . . .	73
4.3.1	Synchrotron X-ray fluorescence analyses (SyXRF) . . . . .	73
4.3.2	Sample preparation . . . . .	74
4.4	Data quality and results . . . . .	74
4.4.1	Limitations of the analytical method . . . . .	74
4.4.2	Possibility of sample contamination . . . . .	76
4.4.3	Br and I abundances . . . . .	77
4.5	Discussion . . . . .	78

4.5.1	Bromine and iodine exsolution . . . . .	78
4.5.2	Origin of bromine and iodine . . . . .	80
4.6	Conclusion . . . . .	83
<b>5</b>	<b>Summary and Conclusion</b>	<b>88</b>

# **Chapter 1**

## **Introduction**

## **1.1 Introduction**

This PhD project is primarily focussed on the basaltic-andesitic plinian eruption of Fontana Tephra in west-central Nicaragua. Principal attention is paid to aspects of eruptive style, tephra dispersal and physical eruption parameters; and dynamics and quantities of volatile release. Moreover, aspects of element partitioning and volatile cycles through the Central American subduction zone are elucidated, which, besides Fontana Tephra, are also manifested by the rhyolitic Upper Apoyeque Tephra.

### **1.1.1 Location and geologic setting**

Fontana Tephra and Upper Apoyeque Tephra have been erupted from vents in west-central Nicaragua: Fontana Tephra originated from a vent in the Masaya area, while the source of Upper Apoyeque Tephra is at the Chiltepe Volcanic Complex north of Managua (Figure 1.1). Recent stratigraphic work in this region placed these two tephtras in a sequence of about twelve highly explosive eruptions that occurred during the past c. 40 000 years. Because of the prevailing easterly winds, most of these tephra deposits are distributed to the west of the northwest-southeast trending Nicaraguan volcanic chain. The volcanic chain is part of the Central American Volcanic Arc (CAVA) that results from subduction of the Cocos Plate beneath the Caribbean Plate.

### **1.1.2 Subduction zone volcanism**

Subduction zone volcanism occurs where two tectonic plates converge and the incoming oceanic lithosphere is consumed into the Earth's mantle. At the Nicaraguan segment of the erosive Central American subduction zone, deep faults resulting from plate-bending prior to subduction are considered to facilitate pervasive infiltration of seawater into the crust and mantle (Ranero *et al.* 2003). When proceeding into greater depths, this highly serpentinised, steeply subducting lithosphere is progressively confronted with rising temperatures and pressures, and fluids can be transferred into the overlying mantle wedge (Rüpke *et al.* 2002), where they facilitate partial melting by lowering of the mantle solidus. The volcanism resulting from these processes is dominated by explosive activity, and great masses of volatiles are released by subduction zone volcanoes (Figure 1.2).

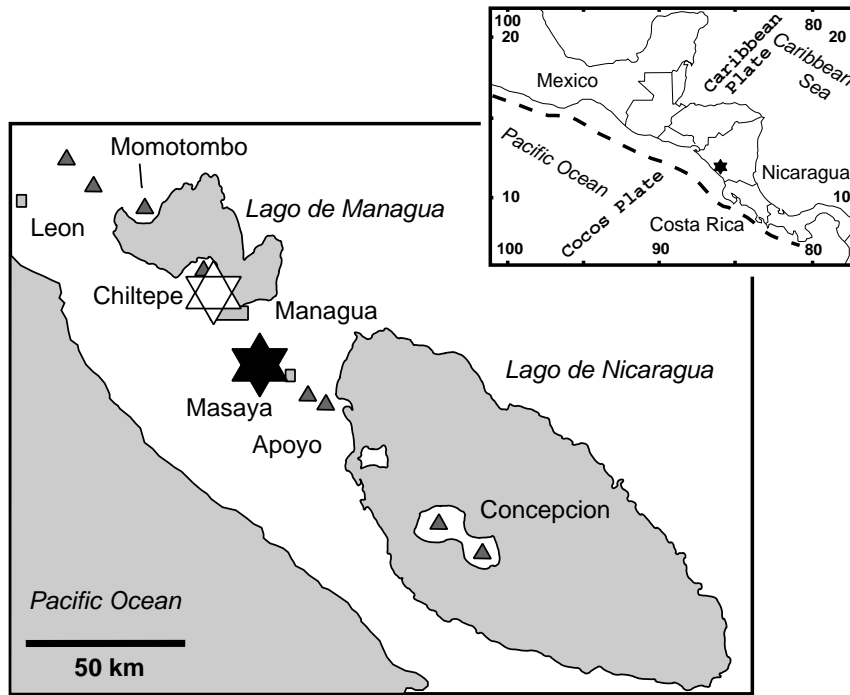


Figure 1.1: Map of west-central Nicaragua showing the Fontana Tephra vent location (black star), and the Upper Apoyeque Tephra vent location (open star). Major volcanic centres are marked by triangles. The inset map illustrates the position in the Central American Volcanic Arc; the dashed line indicates the trench.

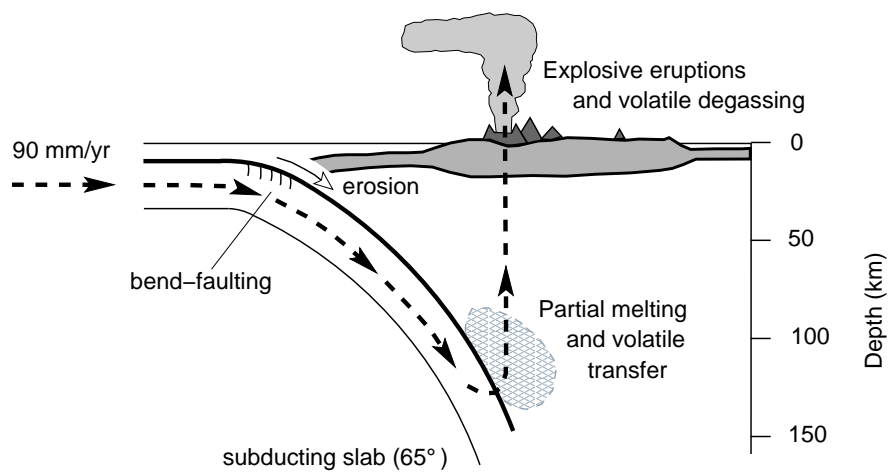


Figure 1.2: Cross-section of the erosive subduction zone at Nicaragua

### **1.1.3 Climatic impact of explosive volcanism**

Injection of volatile elements such as halogens and sulphur into the air leads to substantial shifts in the atmosphere's chemistry. Sulphur is rapidly converted into sulphuric acid aerosols, thus changing the insolation intensity. The aerosols reflect solar radiation back to space causing a negative radiative forcing, thereby leading to periods of global surface cooling following large-magnitude eruptions that emitted significant amounts of sulphur (e.g. Self *et al.* 1996; Robock in press.). Moreover, the ozone layer may be destroyed by catalytic effects of reactive halogen radicals (e.g. Brasseur 1992), of which especially the heavy halogens are known to be very efficient (Bureau *et al.* 2000; Solomon *et al.* 1994). These effects will be particularly strong when the volatiles are injected high into the stratosphere by plinian eruption columns of tens of km height. Volatile release by highly explosive volcanoes may therefore have a considerable impact on the global climate.

## **1.2 Objectives of this study**

### **1.2.1 Mafic plinian volcanism - poorly understood**

The Late-Pleistocene Fontana eruption is one of the few documented eruptions, where a mafic magma erupted in an unusual, plinian style. Such a combination has also been observed for example at the 1886 AD Tarawera eruption (Walker *et al.* 1984; Houghton *et al.* 2004), the 122 BC Etna eruption (Coltelli *et al.* 1998; Houghton *et al.* 2004), and the 6–2 ka BP Masaya eruptive sequence (Williams 1983; Perez and Freundt *subm.*). Recently, considerable advances have been made to understand these untypical eruptions of mafic magmas individually. However, no generally valid model has yet been established to account for this type of volcanic activity, and as only few cases of such volcanism exist, detailed investigations are essential to detect the various mechanisms possibly involved in governing the eruptive style. Plinian eruptions so far have been explained by effects of high volatile contents and high viscosities of felsic magmas (e.g. Sparks *et al.* 1994); both factors are generally not applicable to mafic magmas. Moreover, the resulting tephra dispersal patterns of mafic plinian eruptions have not yet been systematically integrated into eruption models, which would be of great use for assessing the far-reaching impact of explosive eruptions.



The most important questions, therefore, that are addressed in this study to investigate the Fontana eruption, are:

- Eruption physics
  - Was this a plinian eruption as previously stated?
  - How did it evolve?
  - What was the eruption's magnitude?
  - What were the physical eruption parameters?
  - Will there be a risk for people and property if a similar eruption happens again?
- Volatile degassing
  - Was the eruption driven by exsolution of large amounts of volatiles?
  - Were extraordinarily high temperatures involved in the eruption process?
  - Was the melt unusually viscous?
  - Was the fragmentation extremely violent?

### **1.2.2 Element recycling through the subduction zone**

The research project of which this dissertation emerged, is embedded in the Sonderforschungsbereich (SFB) 574 "Volatiles and fluids in subduction zones", hosted at the University of Kiel. General aims of the SFB 574 are to obtain a better understanding of the material transfer through subduction zones: input-output budgets, and the fate of various elements during their travel from the ocean floor at the fore-arc down the subducting slab, their melting at depth, their subsequent rise in ascending magma bodies and finally, their return back to the Earth's surface through volcanic eruptions.

From a volcanological point of view, such volatile cycling and quantification contains three aspects of interest: (1) volatiles in magmas may provide information about the source region at depth, (2) released volcanic gases may contribute to climate effects on a global scale, and (3) volatile abundances determine the explosivity

of magmas and therefore the volcanic hazards. Hence, within the frame of the SFB and with regard to global climate hazards, more objectives arise for this study:

- What amounts of volatiles have been released during the mafic Fontana and the felsic Upper Apoyeque eruptions?
- Do the volatile concentrations in the products of these eruptions yield any clues about the material input into the subduction zone?

### **1.3 Thesis outline**

The aims and topics of this PhD project as outlined above are presented in three separate articles in chapters two to four.

Chapter two is a paper (submitted to the Geologic Society of America Special Paper on Volcanic hazards in Central America (edited by William I. Rose)) that deals with physical aspects of the Fontana eruption. The tephra deposit is presented with lithologic characteristics, dispersal patterns, and volumes of several subunits. From the nature of the deposit, physical eruption parameters such as eruption column heights and wind velocities at the time of the eruption are inferred. Different models - to derive maximum column heights from the downwind and crosswind ranges of the maximum grain sizes; as well as to determine average column height with a plume sedimentation model - have been applied for this purpose. As these models were originally designed for rhyolitic plinian eruptions, aspects of their applicability to mafic tephtras are discussed. Finally, the tephra dispersal data have been used to comment on the volcanic hazard emerging for the local population.

Chapter three, prepared for submission to Journal of Volcanology and Geothermal Research, presents geochemical data of Fontana Tephra. Melt inclusions and matrix glasses have been studied with regard to major elements and volatiles. Major elements were determined by electron microprobe, while volatile elements, in particular water, fluorine, chlorine, and sulphur have been measured by secondary ion microprobe. The paper quantifies the volatile release of the different elements and their evolution during the successive phases of the eruption, i.e. their variation as the eruption proceeds. Fluid-melt partition coefficients for F and Cl are determined. H<sub>2</sub>O data, and mineral-melt equilibrium considerations, have been used to

determine magma chamber conditions such as pressure and temperature. Sulphur and light halogens are set into relation to the melt's major element composition, in terms of their solubility and corresponding exsolution behaviour. The volatile and porosity data indicate that degassing was controlled by homogeneous bubble nucleation. This first delayed, then massive degassing is proposed to be responsible for the intense fragmentation which, together with the high magma temperature, facilitated the plinian eruption style.

Chapter four, submitted to *Chemical Geology*, extends our knowledge of volcanic gas release to two volatile species that have rarely been investigated in volcanic glasses: the heavy halogens bromine and iodine. An advance has been made to determine the concentrations of Br and I in Fontana Tephra and Upper Apoyeque Tephra melt inclusions and matrix glasses, using a synchrotron-XRF instrument. Aspects of origin and partitioning of the heavy halogens are discussed.

In chapter five, the major findings of the three articles are summarised.

## **Bibliography**

Brasseur, G. (1992): Volcanic aerosols implicated. *Nature* 359, 275–276.

Bureau, H., Keppler, H., and Metrich, N. (2000): Volcanic degassing of bromine and iodine: Experimental fluid/melt partitioning data and applications to stratospheric chemistry. *Earth and Planetary Science Letters* 183, 51–60.

Coltelli, M., Del Carlo, P., and Vezzoli, L. (1998): Discovery of a Plinian basaltic eruption of Roman age at Etna volcano, Italy. *Geology* 26/12, 1095-1098.

Houghton, B.F., Wilson, C.J.N., Del Carlo, P., Coltelli, M., Sable, J.E., and Carey, R. (2004): The influence of conduit processes on changes in style of basaltic Plinian eruptions: Tarawera 1886 and Etna 122 BC. *Journal of Volcanology and Geothermal Research* 1137, 1–14.

Perez, W. and Freundt, A. (subm.): The youngest highly explosive basaltic eruptions from Masaya Caldera Complex (Nicaragua): stratigraphy and hazard assessment. In: Rose, W.I. (ed.) *Volcanic Hazards in Central America* Geological Society of America Special Paper.

Ranero, C.R., Phipps Morgan, J., McIntosh, K., and Reichert, C. (2003): Bending-related faulting and mantle serpentinization at the Middle American trench. *Nature* 425, 367–373.

Robock, A. (in press.): Climatic impact of volcanic emissions. In: Sparks, R.S.J. and Hawkesworth, C. (eds.): *State of the Planet*, AGU monograph.

Rüpke, L.H., Phipps Morgan, J., Hort, M., and Connolly, J.A.D. (2002): Are the regional variations in Central American arc lavas due to differing basaltic versus peridotitic slab sources of fluids? *Geology* 30 (11), 1035–1038.

Self, S., Zhao, J.-X., Holasek, R.E., Torres, R.C., and King, A.J. (1996): The Atmospheric Impact of the 1991 Mount Pinatubo Eruption. In: Newhall, C.G. and Punongbayan, R.S. (eds): *Fire and Mud: Eruptions and Lahars of Mount Pinatubo, Philippines*, Washington University Press, Seattle, WA.

Solomon, S., Garcia, R.R., and Ravishankara, A.R. (1994): On the role of iodine in ozone depletion. *Journal of Geophysical Research* 99D, 20491–20499.

Sparks, R.S.J., Barclay, J., Jaupart, C., Mader, H.M., and Philipps, J.C. (1994): Physical aspects of magma degassing I. Experimental and theoretical constraints on vesiculation. *Reviews in Mineralogy* 30, 413–445.

Walker, G.P.L., Self, S., and Wilson, L. (1984): Tarawera, 1886, New Zealand - a basaltic plinian fissure eruption. *Journal of Volcanology and Geothermal Research* 21, 61–78.

Williams, S.N. (1983): Plinian airfall deposits of basaltic composition. *Geology* 11, 211–214.



## **Chapter 2**

# **Fontana Tephra: a basaltic plinian eruption in Nicaragua**

**Heidi Wehrmann<sup>1</sup>, Costanza Bonadonna<sup>2,3</sup>, Armin Freundt<sup>1,4</sup>,  
Bruce F. Houghton<sup>3</sup>, Steffen Kutterolf<sup>1</sup>**

1. SFB 574 at Kiel University, Wischhofstr. 1-3, 24148 Kiel, Germany
2. Department of Geology, University of South Florida, 4202 East Fowler Ave, Tampa, FL, 33620, USA
3. Department of Geology and Geophysics, School of Ocean and Earth Science and Technology, University of Hawaii at Manoa, 1680 East-West Road, POST Building 617a, Honolulu, Hawaii 96822, USA
4. IfM-GEOMAR, RD4, Wischhofstr. 1-3, 24148 Kiel, Germany

## **Abstract**

Fontana Tephra was erupted from the Masaya area in west-central Nicaragua in the Late Pleistocene. This basaltic-andesitic plinian eruption evolved through (1) an initial sequence of short highly explosive pulses emplacing thinly-stratified fallout lapilli, (2) a surge debouching to the southwest while fallout took place in the north-westerly dispersal sectors, (3) a series of quasi-steady plinian episodes depositing massive fallout beds of highly-vesicular scoria lapilli. The plinian episodes were repeatedly interrupted by (4) phreatomagmatic pulses, evidenced by layers of higher lithic contents and scoria clasts with quenched rims, as well as by proximal cross-bedded fine-medium lapilli pyroclastic surge deposits, which left pale ash partings at distal locations. The terminal phase of the eruption (5) comprised numerous sub-plinian eruption pulses in which varying amounts of external water were involved, forming a well-stratified sequence of lapilli beds.

Erupted tephra volumes, column heights and wind velocities have been estimated for three different vent scenarios, because no firm source location could be identified. The total erupted tephra volume is between 1.4 and 1.8 km<sup>3</sup>, much lower than previous estimates for this eruption; these are minimum values since distal ashes are not exposed. Eruption column heights ranging between 24 to 30 km for the plinian eruptive phases were obtained from comparing distribution data with modelling results. Consistent results from different approaches suggest that these models, which were developed for rhyolitic plinian eruptions, also provide good approximations for basaltic plinian eruptions considering all sources of uncertainty.

**Keywords:** basaltic plinian eruption, tephra volume, eruption parameters

## 2.1 Introduction

### 2.1.1 Mafic plinian volcanism

Two classic papers (Williams 1983; Walker *et al.* 1984) suggested for the first time that basaltic magma can be erupted with the explosive intensity necessary to produce plinian fall deposits. Few significant developments have taken place in the 20 years that have elapsed except for the detailed documentation of another example, the 122 BC eruption of Etna described by Coltelli *et al.* (1995). In this study we re-examine the reportedly largest and most powerful of these documented violent basaltic eruptions, which produced Fontana Tephra in Nicaragua. Explosive basaltic events more commonly take the form of hawaiian lava fountains or strombolian eruptions, or phreatomagmatic surtseyan to vulcanian eruptions (Simkin and Siebert 1994). Such eruptions are characterised by low magma discharge rates which limit both eruption column heights and lateral dispersal of tephra. Plinian basaltic volcanism is the most dangerous, yet least well studied type of basaltic activity. Such intense explosive eruptions have far-reaching impacts, due to their wide dispersal areas and high emissions of volcanic gases. The risk to communities is exacerbated further because the rapid ascent rate of basaltic magma means that the warning time for a basaltic plinian eruption (time between onset of unrest and onset of eruption) may be as short as a few hours. In addition, because such eruptions are atypical of most volcanism at basaltic centers, their precursors may be misunderstood until too late.

The factors that facilitate the eruption of basaltic magma in a highly intense plinian fashion remain largely unknown. More typically open-system magma ascent and degassing leads to variably efficient separation of low-viscosity melt and gas phases to produce lava effusion or hawaiian and strombolian eruptions (Head and Wilson 1987; Jaupart 2000; Jaupart and Vergnolle 1989; Mangan and Cashman 1996; Mangan *et al.* 1993; Parfitt 2004; Parfitt and Wilson 1995; Seyfried and Freundt 2000; Vergnolle and Jaupart 1986; Wilson and Head 1981). The majority of basaltic eruptions worldwide fit this model, but plinian and subplinian eruptions are less compatible with the model, due to their sustained and intense character. Preliminary results from ongoing studies show that basaltic magma interacted with rhyolitic country rock during the 1886 AD Tarawera eruption (Houghton *et al.* 2004)



whereas the 122 BC Etna eruption appears to have been controlled mostly by inherent magmatic processes (Coltelli *et al.* 1998). Yet, no common factor explaining the high intensity of eruption has been identified.

Our present re-investigation of Fontana Tephra - the Fontana Lapilli of Williams (1983b) and Masaya Lapilli Bed of Bice (1985) - addresses another question, which is especially relevant for the hazard assessment at basaltic volcanoes: how do basaltic plinian eruptions evolve? Part of this problem is to decide if commonly employed models for tephra dispersal that were designed for silicic plinian eruptions can be applied successfully to basaltic plinian fallout and to case studies where areal coverage of exposures is incomplete. We have divided Fontana Tephra into 7 units (A-G) and document the lithology, areal thickness, and maximum-grain-size distribution of each to infer the position of the now-buried vent and changes in eruptive style, and to determine eruption parameters such as ejected volume, column height and discharge rate.

### **2.1.2 Geologic setting and previous work on Fontana Tephra**

The volcanic front of western Nicaragua is part of the Central American Volcanic Arc. West-central Nicaragua, including the capital Managua and the cities of Masaya and Granada, is densely populated and exposed to hazards from near-by volcanoes, particularly from Masaya volcano. The Masaya volcanic system comprises the younger Masaya composite cone with its active Santiago crater (McBirney 1956; Walker *et al.* 1993; Rymer *et al.* 1998) and the six by eleven km Masaya Caldera, from which several highly explosive eruptions within the past c. 6000 years produced widespread basaltic deposits (Perez and Freundt this volume; Bice 1985; Williams 1983b), which are slightly less silicic (c. 50 % SiO<sub>2</sub>) than the basaltic-andesitic Fontana Tephra (53 % SiO<sub>2</sub>). Tuffaceous sediments and a well-developed palaeosol separate Fontana Tephra from the concordantly overlying Lower and Upper Apoyo tephtras, in turn separated by an incipient palaeosol and yielding overlapping <sup>14</sup>C-ages of 23,890±240 and 24,650±120 a BP, respectively (Kutterolf *et al.* in prep.). We estimate the age of the Fontana eruption as c. 30 ka BP, largely in agreement with Bice's (1985) estimate of 35-25 ka BP, as well as with a preliminary estimate by Kutterolf *et al.* (in prep.) in the same range inferred from marine

tephrostratigraphy offshore Nicaragua.

Bice (1980; 1985) described Fontana Tephra as a uniform, non-bedded, non-graded, and well-sorted black basaltic scoria deposit with a distinctive thin, black basal ash. He also noted parallel whitish bands cutting through the deposit, which he interpreted as plant ash. Based on the direction of increasing deposit thickness, Bice tentatively identified Masaya Caldera as the source of Fontana Tephra, where it is covered by younger volcanic deposits. He supported his assumption with the chemical similarity between Fontana Tephra and the younger Masaya Triple Layer and Masaya Tuff, which both stem from Masaya Caldera.

Williams (1983a;b) studied these three products of highly explosive eruptions from Masaya Caldera in detail. His data on Fontana Tephra provided a useful starting point for our investigation. Williams attributed the sheet-like geometry of the deposit to a plinian eruption with a very high eruption column estimated at 50 km and a wind velocity of 30 m/s based on the observations of the Mount St. Helens 1980 eruption. Williams calculated a tephra volume of  $12 \text{ km}^3$  from his isopach map, within the 1 mm isopach, and estimated the discharge rate as  $2 \times 10^5 \text{ m}^3/\text{s}$ , indicating that the eruption would have lasted for two hours. He suggested that the high temperature of the basaltic magma resulted in a higher eruption column than from a silicic eruption of comparable volume. Williams also observed a 73-m-thick, non-welded fallout deposit at the western Masaya Caldera wall, close to his proposed vent inside the caldera. This he interpreted as a proximal cone-building phase of fallout from sufficiently great height to facilitate cooling of the clasts and to prevent welding of the deposit. In contrast to Bice, Williams interpreted the distinctive light-coloured bands in the deposit to have formed by percolating groundwater.

Williams' quantitative estimates involve significant extrapolation of his isopach and isopleth data. Moreover, the abundance of similar-looking scoria lapilli deposits in the Masaya-Managua region requires careful identification of lithologic components and correlation of internal beds between outcrops to substantiate correlations. Our re-examination of Fontana Tephra shows that the eruption evolved through several phases of distinct eruption styles and intensities. Such details are crucial to gain a better understanding of the mechanisms of mafic plinian volcanism.

## 2.2 Fontana Tephra

We have remapped Fontana Tephra over an area of 200 km<sup>2</sup>, to the north and northwest of Masaya Caldera (Figure 2.1). The pattern of exposure of Fontana Tephra is rather unusual. The deposit is exceptionally well-exposed over only some 150 km<sup>2</sup> to the north and west of all possible source vents. No exposures exist in any of the remaining sectors and northerly exposures end at the shoreline of Lake Managua. The deposit can be subdivided readily into 7 units each of which consists of several beds with interspersed ash partings. These units differ in grain size, clast populations, and bedding characteristics. Absolute and relative thicknesses of these units vary between outcrops due to different areal dispersal patterns. Isopach and isopleth maps were constructed for the prominent units of the succession. Figure 2.2 illustrates the succession of units as found at medial exposures.

### Unit A

The base of Fontana Tephra is made up of two beds of well-sorted black, highly-vesicular, fluidally-textured hawaiian-type lapilli with very thin glass walls separating the bubbles. We found no lithic fragments in this layer which reaches 12 cm thickness at the most proximal exposures (outcrop 15 in Figure 2.1), and thins rapidly away from source.

### Unit B

Unit B is composed of dark-grey fine to medium scoria lapilli which are highly-vesicular, but less so than the hawaiian particles of unit A. At outcrop 15, unit B reaches a maximum thickness of 86 cm and is crudely bedded. At more distal locations towards the north-northwest, up to eight planar beds of alternating fine lapilli and coarse ash can be distinguished. Lithics make up less than 1 % of unit B (visually estimated).

### Unit C

To the south of the vent, the stratigraphic position between units B and D is occupied by a cross-bedded, poorly sorted deposit that is 400 cm thick at outcrop 17, the lowermost 300 cm being distinctly coarser grained than the top 100 cm, where cross-bedding is better developed. The deposit thins rapidly over 2.5 km to 30-60 cm at outcrop 19. Lapilli-size (typically 3-10 mm in diameter) scoria and lithic

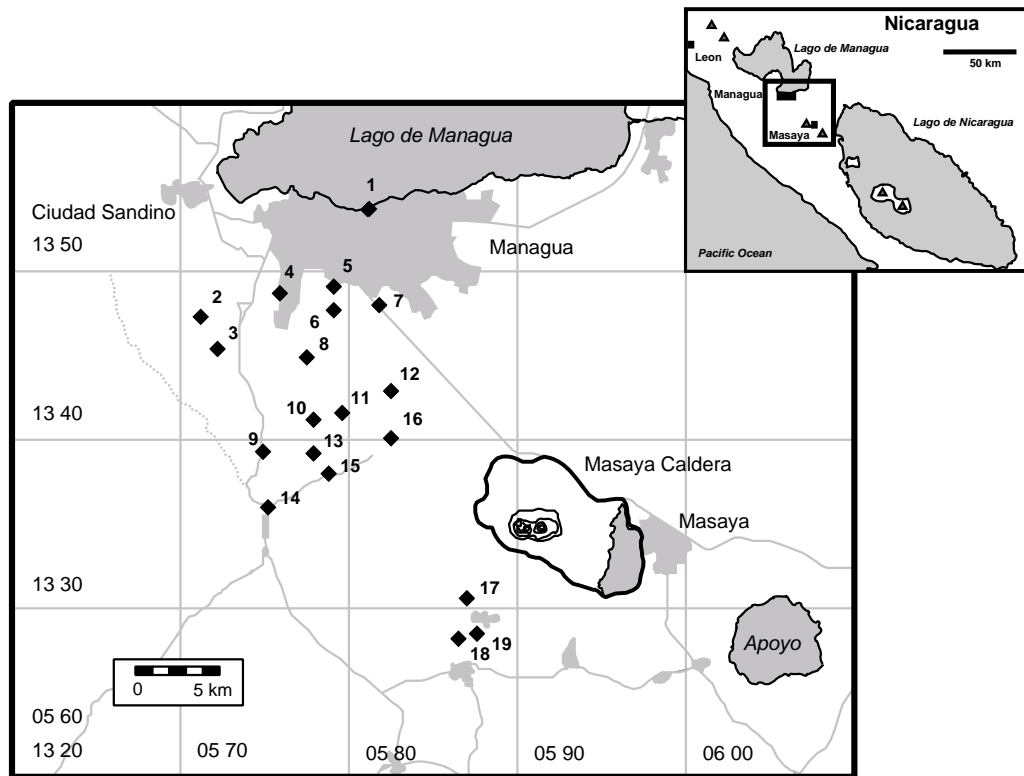


Figure 2.1: Fontana Tephra localities in the Managua-Masaya area. Map uses UTM coordinates; field area position within the Nicaraguan volcanic front is shown in the inset map of west-central Nicaragua. Major volcanic centres are marked by triangles.

particles are set in an ash matrix. The juvenile particles are ash-coated medium-grey scoria with spherical to elongated bubbles. Lithic particles reach 130 mm in diameter, account for c. 10% of the lapilli fraction, and are dominated by mafic dense lava clasts, c. 70% of which are strongly hydrothermally altered. A minor amount of rhyolitic pumice clasts is present. The topmost 10 cm consist of a grey medium-coarse ash.

No such cross-bedded deposit is found at other than these proximal localities. Instead, outcrops across the medial range to the northwest show a series of thin, poorly-sorted, horizontally bedded lithic-bearing layers of grey fine-ash-coated medium scoria lapilli in this stratigraphic position. Scoria clasts are subangular to sub-rounded, medium grey, crystal-poor, and are characterised by spherical and elongate

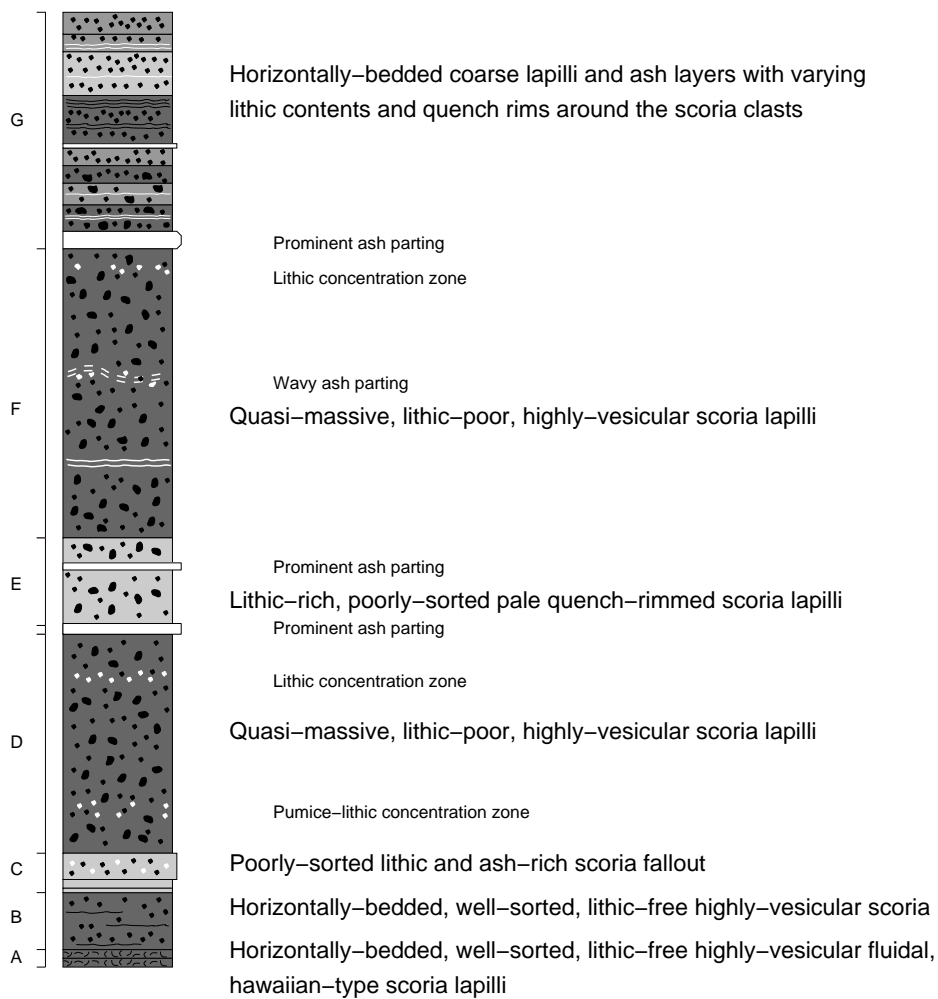


Figure 2.2: Stratigraphic section of Fontana Tephra illustrating variations in lithology and unit division.

vesicles. These layers are also matrix-supported and contain lithic clasts of mafic lava, hydrothermally altered mafic lava, as well as rhyolitic pumice. The pumices are silky white-pink with tubular bubbles. Despite extensive stratigraphic work in west-central Nicaragua, no source deposit for this pumice has been found (Kutterolf *et al.* in prep.). However, this pumice type only occurs in Fontana Tephra and is thus a valuable tool to distinguish it from other scoria lapilli deposits.

At more distal outcrops, thin, poorly-sorted ash beds occur. Those are composed of

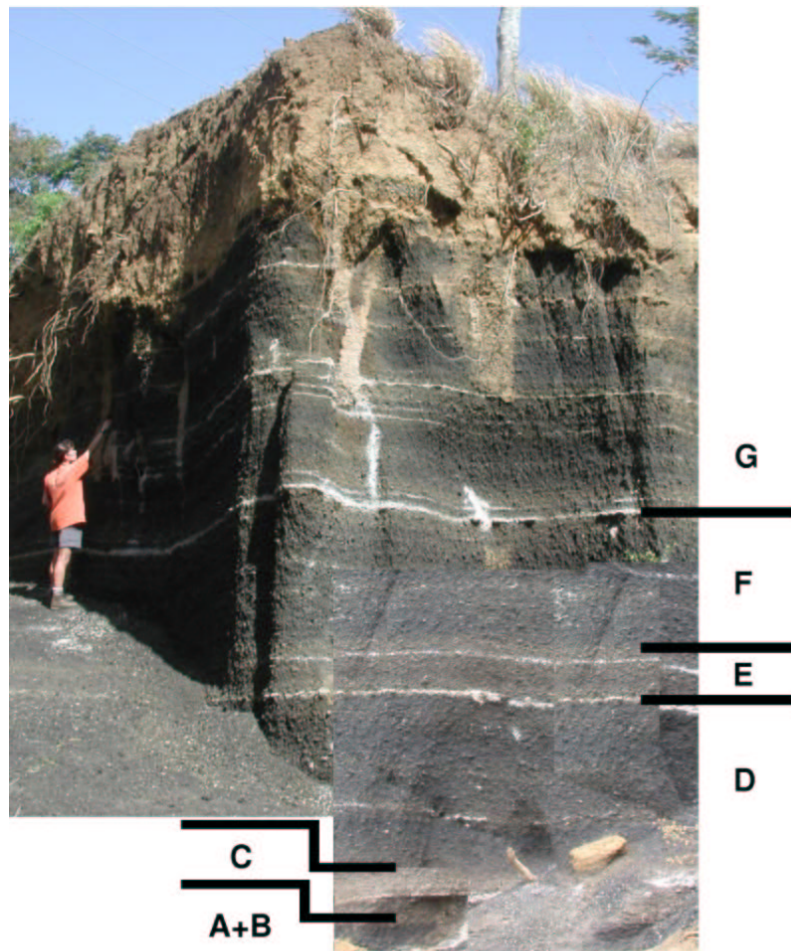


Figure 2.3: Composite photo of Fontana Tephra at outcrop 12 (Figure 2.1).

pale-grey glass shards, and a relatively large percentage (c. 10-15 %) of hydrothermally altered lithics.

#### Unit D

Unit D is a thick, massive to vaguely stratified bed of highly vesicular dark-grey scoria lapilli, which is ubiquitously present in the entire area of dispersal. The top of this unit is marked by a prominent white ash layer. Most scoria clasts are highly vesicular with spherical bubbles, however, denser clasts with irregular, coalesced bubbles are also present. The unit reaches a thickness of 137 cm at outcrop 16.

Although the lithic content of this unit amounts to less than 2 %, there are two hor-

izontal zones of higher lithic concentrations (5-7 %) in which particular lithic types occur. A zone in the lower quarter of the deposit contains rhyolitic pumice lithics of the same type as in unit C. A second zone at about 5-10 cm below the top of unit D contains conspicuous orange-coloured, hydrothermally altered fragments of older lavas and tuffs.

#### Unit E

Unit E consists of two layers of dark-grey medium scoria lapilli with medium-grey fine-ash coatings, separated by a central prominent ash parting. In contrast to the well-sorted units D and F, unit E is only moderately well sorted due to the presence of ash in interstices in the lapilli-supported deposit. Scoria clasts display a range in vesicle shapes from spherical to irregular. The unit also contains conspicuous lithics (c. 5 %) that are predominantly hydrothermally altered mafic lava. The unit crops out throughout the western to northern part of the area of dispersal, maximum measured thickness is 38 cm at outcrop 16.

#### Unit F

Unit F is a thick, quasi-massive layer of dark-grey to black, scoria lapilli. It shows weak bedding defined by intervals that are characterized by diffuse concentrations of stained or ash-coated lapilli. Highly-vesicular clasts with spherical to elongated vesicles coexist with moderately vesicular ones containing irregular bubbles. About 5 % of dark-red scoria clasts have, on average, a larger size and larger bubbles compared to the dark-grey clasts. The layer incorporates several (three to ten) weak to strong, partly wavy but mostly planar, pale and brown ash partings. In the two lithic-bearing zones, mostly hydrothermally-altered mafic lavas and tuffs make up c. 5 %. A few (< 1 %) hawaiian-type scoria lapilli are present. Like Unit E, Unit F is distributed towards the west and the north of the vent. Its greatest thickness is 140 cm.

#### Unit G

The upper part of the deposit is distinctly better stratified than the underlying units. It is made up of a series of thin (typically several cm), fine to coarse lapilli and ash layers, some of which are well-sorted lithic-poor beds of angular scoria, while others are only moderately sorted and characterised by higher lithic-contents (up to 3-5 %). At least seven ash partings are present. Although unit G reaches a thickness

of more than 3 m at proximal sites, it is commonly strongly eroded so that a consistent correlation of its component layers across the mapping area was not possible.

#### Ash partings

The entire deposit exhibits a spectacular set of ash partings (Figure 2.3) at fairly regular dm-thick intervals that easily correlate throughout most outcrops. Across most of these ash partings the grain sizes of the scoria lapilli do not change, but the pore spaces between the clasts are filled with much finer-grained white to pale grey-brown particles down to fine ash size. At one outcrop location on the dispersal axis (outcrop 13; Figure 2.1), a good exposure of Unit G shows the lateral transition of such an ash parting via gradual thickening to a strongly cross-bedded, fine-lapilli deposit.

### **2.3 Distribution of depositional units**

The pattern of preservation of Fontana Tephra places some limitations on our ability to constrain the dispersal of the eruption products. Isopach and isopleth maps for the units D, E, and F are shown in Figures 2.4 and 2.5. Units D, E, and F are the best preserved units in the whole dispersal area of the Fontana deposit. Maximum scoria and lithic clast isopleths are based on the average dimension of three axes determined for the five largest clasts, respectively, as suggested by Sparks (1986).

Data for units D, E, and F have some features in common. Although dispersal axes generally point toward the northwest, elongation of contours along the axes in any reconstruction remains very limited. No outcrop data is available to close the contour lines in the southeastern through southwestern sectors. This, and the absence of proximal exposures, inhibits a straight-forward identification of the Fontana vent site. If Fontana Tephra originated from Masaya Caldera as previously assumed (Bice 1985; Williams 1983b), our isopach and isopleth data would point to a source in the northwestern part of the present caldera (vent 3). This assumption was predicated strongly on the existence of a thick proximal exposure on the Masaya Caldera wall.



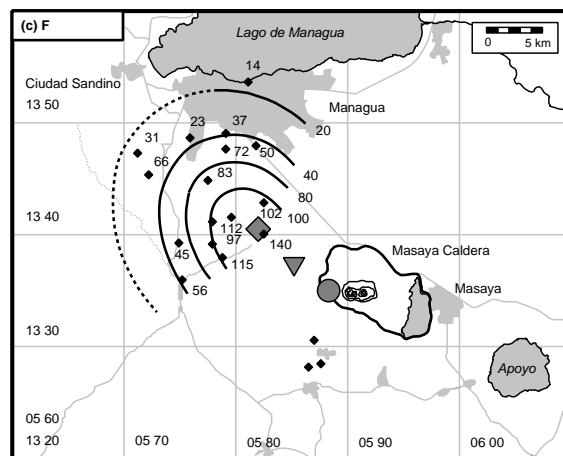
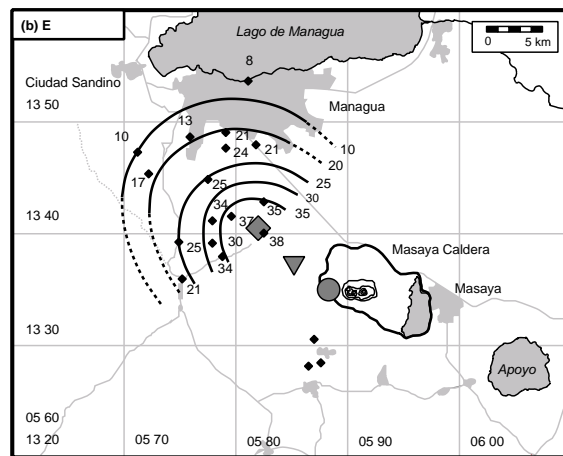
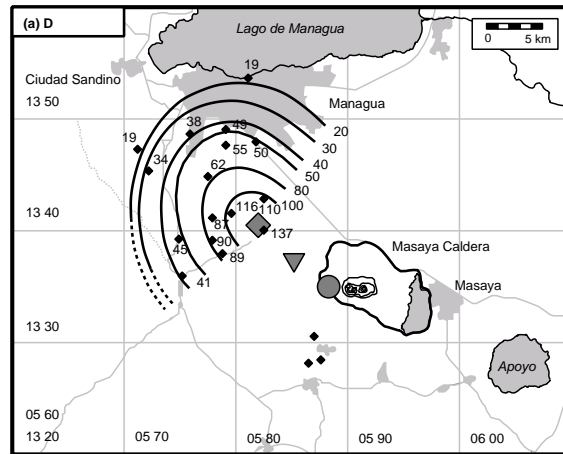


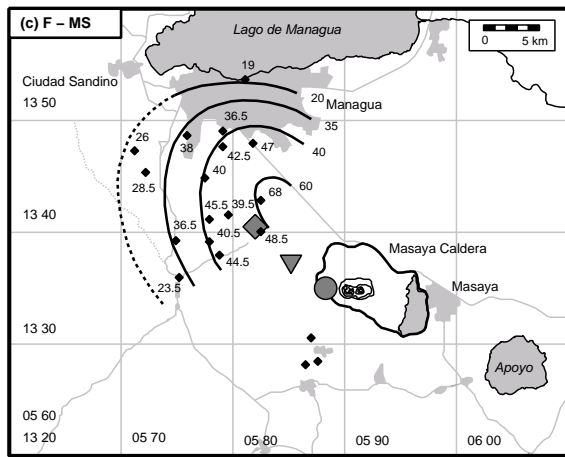
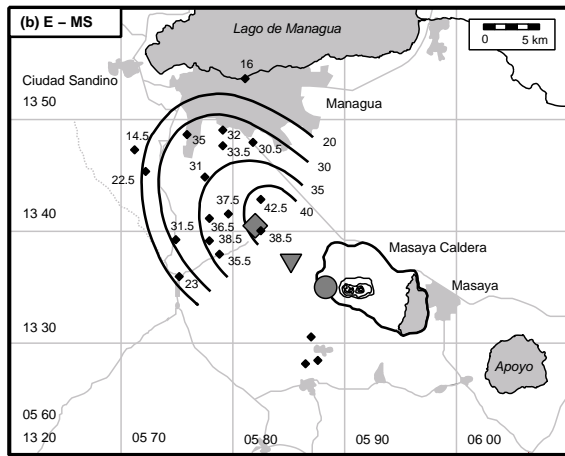
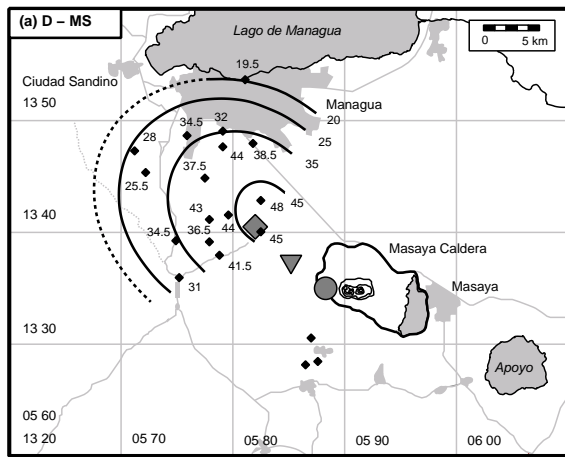
Figure 2.4: Isopach maps (in cm) for the plinian units (a) D (b) E and (c) F. Dashed lines are extrapolated contours. Large symbols mark possible vent sites discussed in the text: vent 1 (diamond), vent 2 (triangle), vent 3 (circle).

However, we found no evidence for a "proximal cone building phase" as proposed by Williams (1983a), which was critical for his reconstruction of the deposit geometry. In fact, we did not find any deposit belonging to the Fontana eruptive sequence in the north-western wall of Masaya Caldera, which is built up primarily of a scoria lapilli fallout that has been tentatively associated with the c. 2 ka old Masaya Triple Layer events (Perez and Freundt this volume), underlain by several beds of lava, breccia, phreatomagmatic deposits and other fallout tephras. The absence of the easily recognized Apoyo tephras in the caldera wall (which are abundantly exposed outside the caldera) suggests the key stratigraphic interval may be buried on the caldera rim. Without such exposures, there is no geologic evidence to prove Masaya Caldera is the source of Fontana Tephra. The chemical similarity to the c. 30 ka younger Masaya Triple Layer, invoked by Bice (1985), is not, in itself, conclusive.

We have considered therefore three contrasting geometries for the Fontana isopachs and isopleths and investigated the implications for eruptive intensity and tephra volume. The first case, which follows the usage of Bice and Williams, in extrapolating isopach contours around a vent site within Masaya Caldera, produces a rather unusual contour pattern of strong along-axis elongation close to vent yet little elongation across the medial range (e.g., vent 3, Figures 2.4 and 2.5). This is atypical of plinian dispersal patterns and would require complicated, and not very probable explanations such as an inclined lower eruption column.

Several other possible geometries exist that would place the source vent outside of Masaya Caldera. In the following sections, we discuss two other possible vent sites (Figures 2.4 and 2.5). In addition to vent 3, we have also investigated a vent position to the northwest, and outside of, Masaya Caldera (vent 2 in Figures 2.4 and 2.5). Such a vent position is more compatible with our field data and coincides with the vent area suggested for pyroclastic deposits of the Las Sierras Formation (van Wyk de Vries 1993).

Finally, we have considered near-circular isopach and isopleth contours around the location labelled as vent 1 as an extreme end member representing conditions of no or little wind during eruption.



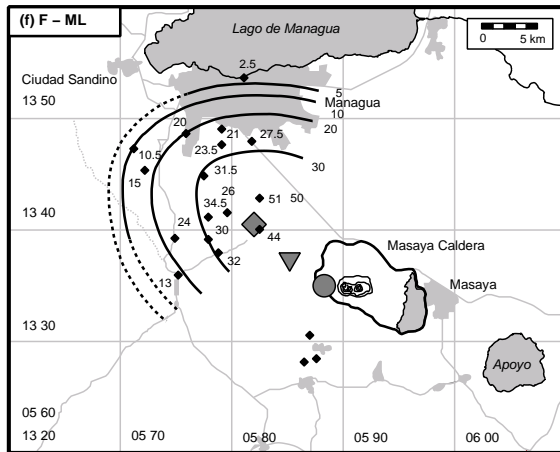
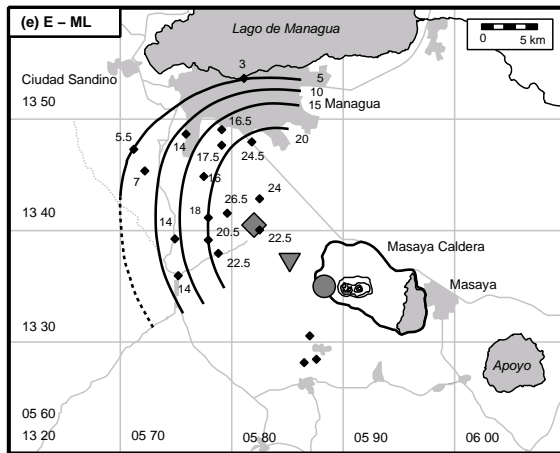
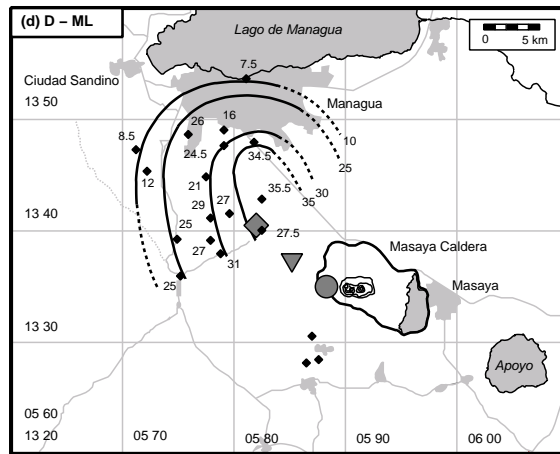


Figure 2.5: Isopleth maps (in mm) of (a-c) maximum scoria (MS) and (d-f) maximum lithic (ML). Grain size defined as the average of the three main axis of the five largest clasts, for the plinian units D, E, and F. Large symbols mark vent sites as in Figure 4.

## 2.4 Evolution of the Fontana eruption

The choice of vent position, not surprisingly, affects the estimates of eruption parameters. To give a reasonable range of values for volume, column height and maximum wind velocity at time of eruption, we apply the models of Pyle (1989), Carey and Sparks (1986) and Sparks *et al.* (1992) to our three vent scenarios. These parameters are crucial for understanding the dynamics of each eruption phase, and to assess the risk originating from future eruptions of this type. Model application must, however, be considered within the qualitative constraints on eruptive behavior deduced from the deposit characteristics.

### 2.4.1 Variations in eruptive style

The Fontana eruption was not continuous, but proceeded in numerous successive eruptive pulses, that were mainly plinian in style. The eruption began with several short, explosive events ejecting ragged and fluidal pyroclasts (hawaiian-type). These pulses were followed by release of a pyroclastic surge towards the southwest, while fallout dominated the other dispersal sectors.

Fairly continuous magma discharge characterises each of the following plinian phases (units D to F). The wide dispersal area of these units (Figures 2.4 and 2.5) suggests high eruption columns. Interbedded layers with poorer sorting, higher contents of various lithic populations, and quench-rims around the scoria clasts indicate repeated but limited interaction of the magma with limited quantities of external water. Transient access of water caused some fluctuations in the eruption but very similar dispersal characteristics of units D to F suggest that after each phreatomagmatic pulse plinian eruption columns recovered to steady conditions.

The stratified alternation between lithic-poor, well sorted dark-grey scoria layers with lithic-rich, moderately sorted pale ash-coated scoria beds, combined with strongly varying grain-size distributions in the terminal phase (unit G) indicates rapidly changing eruptive conditions and short-lived pulses.

## 2.4.2 Erupted volumes

Tephra volumes were obtained for units D, E and F from isopach maps according to Pyle (1989). This method assumes that the deposit thins exponentially away from source and allows us to extrapolate from the well-constrained medial part of the depositional fan towards the source as well as to distal locations. Volumes of fall deposits thus determined are known to represent only a minimum erupted volume as the deposit thinning is not well constrained where distal thickness data is lacking (e.g. Pyle 1995; Rose 1993; Bonadonna *et al.* 2005). However, this is also the most reliable method available to determine the volume of poorly constrained deposits. Log-linear plots of thickness versus the square root of each isopach area display subparallel straight lines for units D, E, and F in the three vent scenarios (Figure 2.6). Table 2.1 shows the resulting volume estimates for these units based on each vent scenario. Volumes obtained by summing the products of isopach area times thickness are also shown for comparison. Volumes range between 0.29 and 0.34 km<sup>3</sup> for unit D, 0.16 and 0.24 km<sup>3</sup> for unit E, and 0.31 and 0.37 km<sup>3</sup> for unit F.

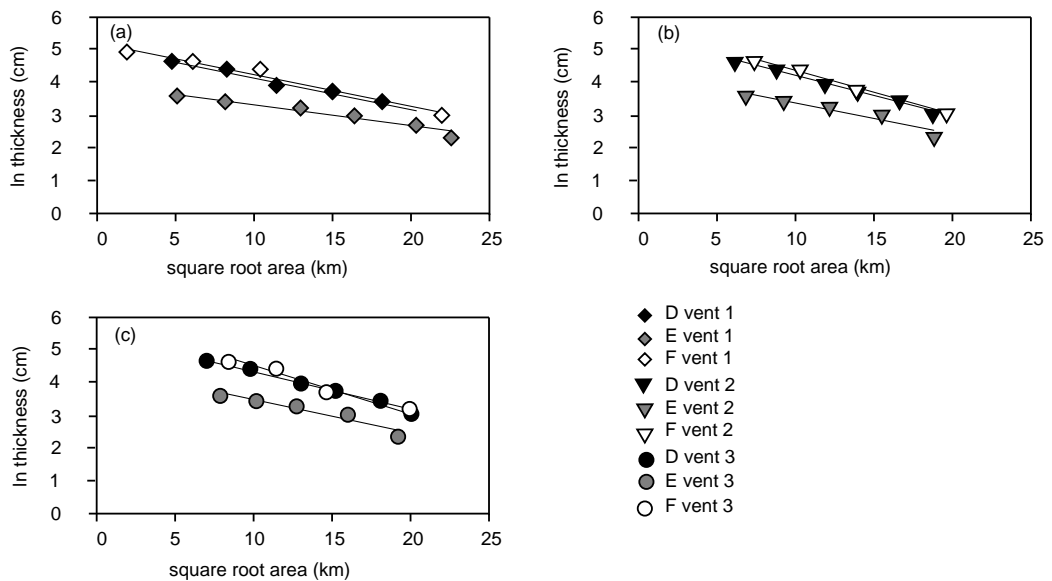


Figure 2.6: Logarithm of thickness (cm) versus square root of area (km) of the isopachs plots of units D, E, and F in the three scenarios considered in the text.

Dispersal parameters provide quantitative evidence of the plinian nature of Units D, E and F. Figure 2.7 shows a semi-log plots of thickness versus (area)<sup>1/2</sup> graph

to illustrate the bulk thickness decay of Fontana Tephra compared to a wide range of hawaiian through plinian deposits. The dispersal pattern of Fontana Tephra is very similar to the 1886 AD Tarawera and 122 BC Etna deposits, and all three basaltic tephra are clearly plinian rather than subplinian in dispersal. Thickness half-distances of  $bt = 6-11$  km and maximum clast half-distances of  $bc = 9-14$  km at medial distances plot in the plinian field of the  $bc/bt$  versus  $bt$  diagram after Pyle (1989).

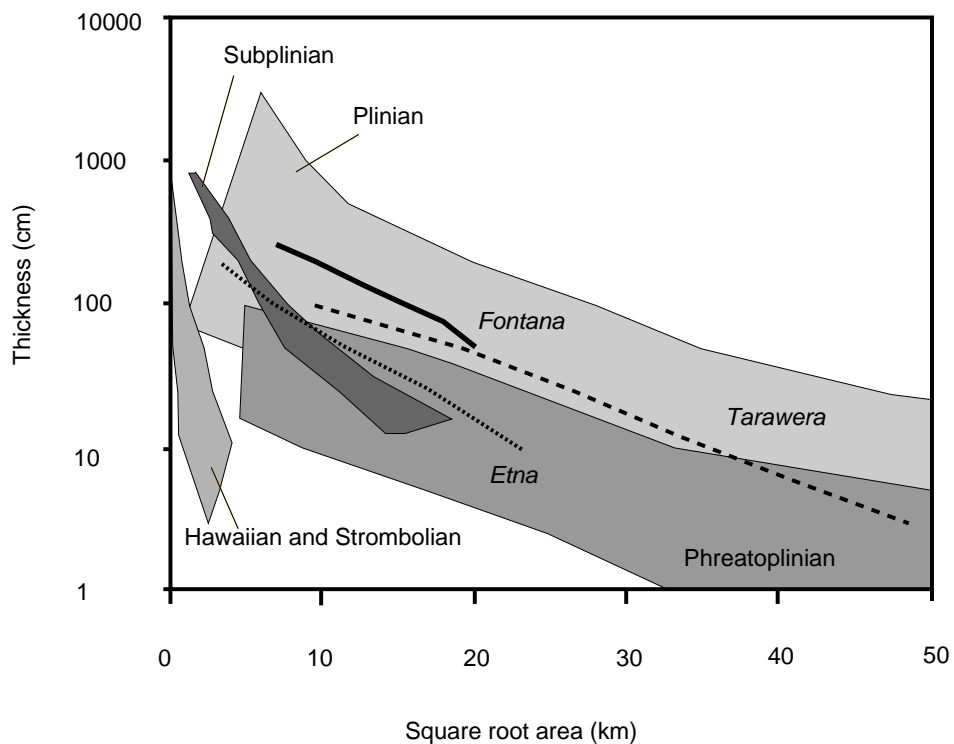


Figure 2.7: Semi-log plot of the total thickness of Fontana Tephra versus square root of the respective isopach areas, in comparison to dispersal patterns of other plinian, phreatoplinian, strombolian, and hawaiian eruptions (after Houghton *et al.* 2000), including the basaltic plinian 1886 AD Tarawera (dashed line) and 122 BC Etna (dotted line) deposits (Houghton *et al.* 2004).

Table 2.1: Inferred erupted volumes of the different fallout units

	Volume estimates after Pyle (1989)			Volume estimates cumulative		
	Vent 1	Vent 2	Vent 3	Vent 1	Vent 2	Vent 3
D	0.34	0.29	0.34	0.35	0.30	0.34
E	0.24	0.16	0.16	0.25	0.16	0.16
F	0.37	0.31	0.34	0.40	0.32	0.36
Total (incl. units A,B,C,G)	<b>1.78</b>	<b>1.36</b>	<b>1.68</b>			

### 2.4.3 Eruption column heights and wind speeds

Eruption column heights and wind conditions at the time of emplacement can be estimated by comparing the down-wind and cross-wind clast-size dispersal with theoretical modelling results (Carey and Sparks 1986). Being based on maximum clast sizes (albeit averages from five clasts), estimated column heights approximate peak values for each phase. As for the volume calculations, we contrast the three different vent locations.

Eruption column heights in the no-wind scenario (vent 1) are inferred through plots of clast diameter against the area enclosed by the respective isopleths. For the wind-affected tephra dispersal (vents 2 and 3), column heights have been determined from along-axis i.e., downwind range and half cross-wind range data for different isopleths. Results are shown in Figures 2.8 and 2.9.

During the first plinian phase D, the eruption column reached an estimated height of 26-30 km. It dropped to 25-27 km for E, then rose again to 24-29 km in the plinian phase F. In contrast to column heights, corresponding wind velocities strongly depend on the vent scenario chosen. For example, using unit D, wind velocity is zero for vent 1, 7-18 m/s for vent 2 and 12-30 m/s for vent 3. Similarly large differences result for the other units. For each of the vent 2 or vent 3 scenarios, however, wind strength and direction did not apparently change during eruption from unit D through unit F.



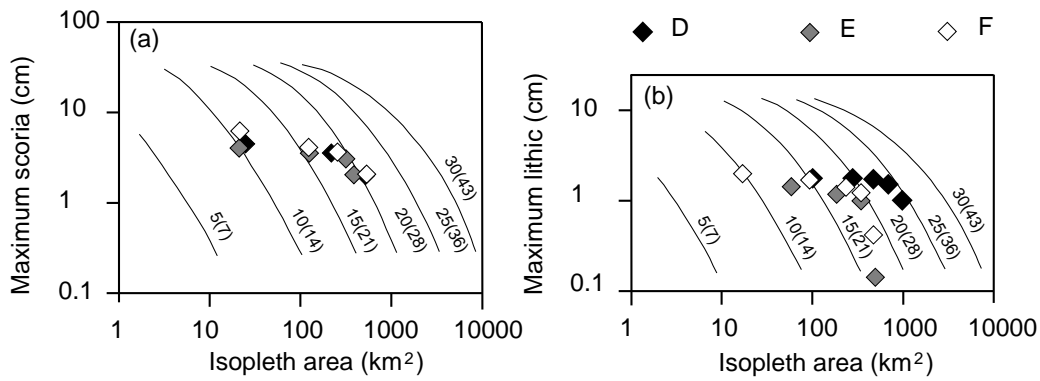


Figure 2.8: Diagrams of isopleth area versus clast size (a) of scoria (density of c. 1000 kg/m<sup>3</sup>) and (b) of lithics (c. 2500 kg/m<sup>3</sup>) for units D, E, and F in a no-wind scenario. Values along the lines correspond to column height at neutral buoyancy level and total column height (in parentheses) as predicted by the analytical model of Carey and Sparks (1986).

Data from different isopleths of a single unit do not parallel the model curves in Figures 2.8 and 2.9 but follow a shallower trend such that larger grain sizes indicate lower column height and wind speed. This deviation cannot be explained by limited availability of field data alone, especially not because the isopleths used in these plots are fairly well-constrained. It rather indicates that the eruption model may encounter some limitations when applied to dispersal of mafic fallout tephra as further discussed below.

Another approach to estimate eruption column heights uses the plume-sedimentation model of Sparks *et al.* (1992). In contrast to the model above, in which data from maximum clasts indicate maximum column heights, the sedimentation model uses a whole grain-size distribution and thus indicates the average column height. The model of Sparks *et al.* (1992) does not account for wind advection, variation of particle Reynolds number, variation of particle density and aggregation processes, which have been proved crucial to our understanding of tephra dispersal (Bonadonna and Phillips 2003). However, we have applied the model of Sparks *et al.* (1992) to support our determination of eruption parameters, but we are planning to carry out a detailed investigation for dispersal of tephra from basaltic plinian eruptions to account for all these factors.

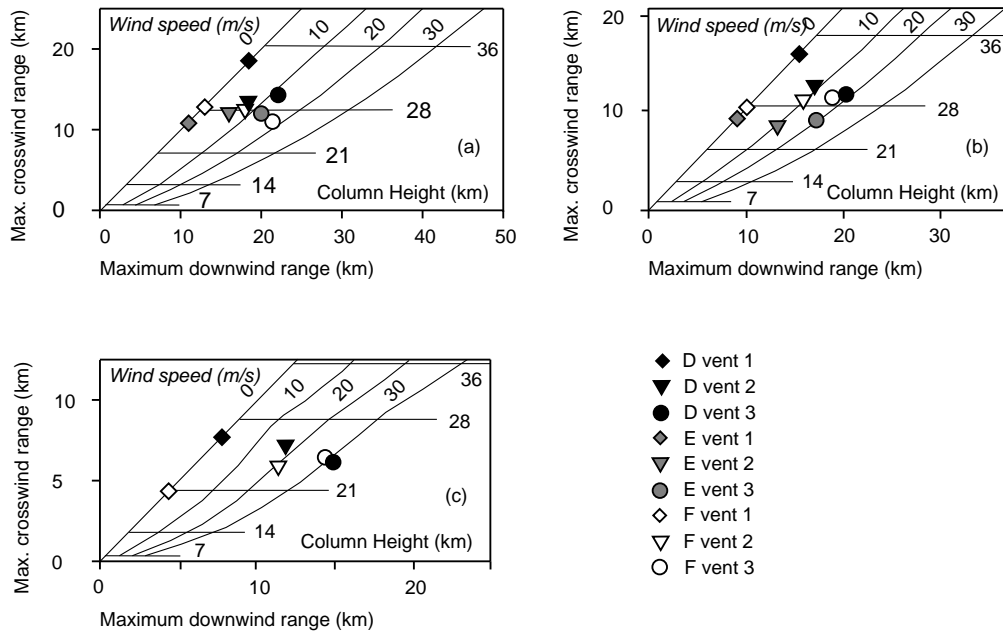
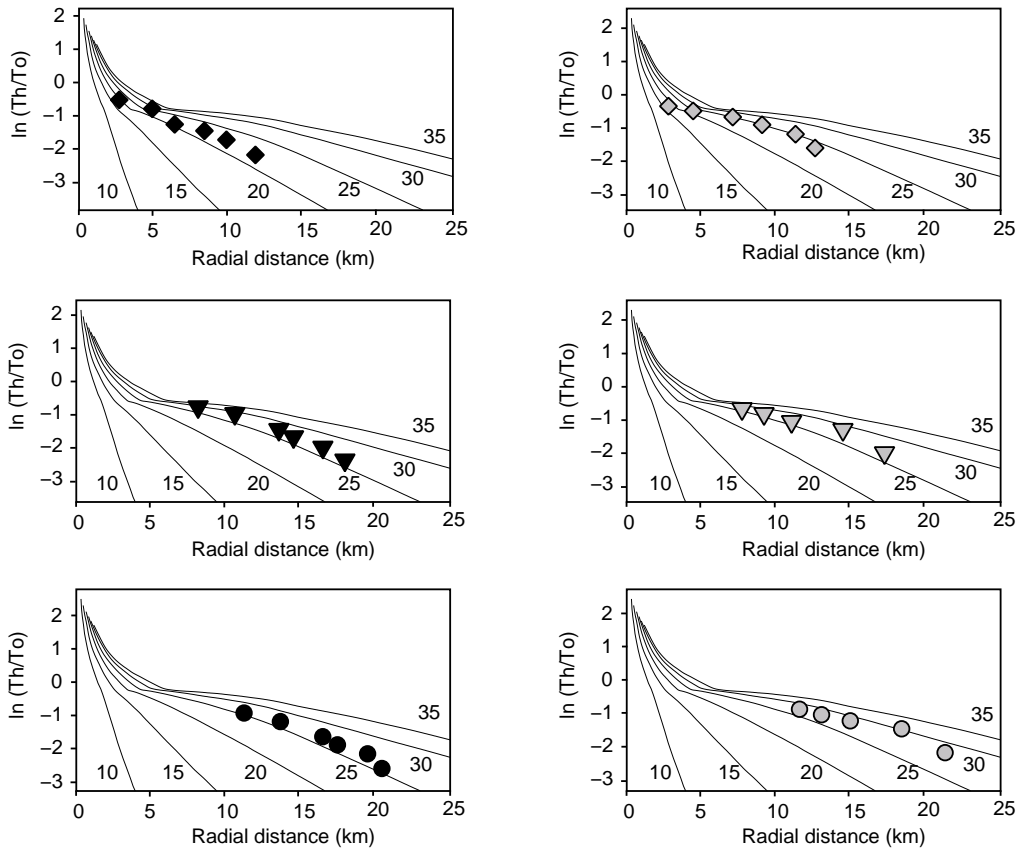


Figure 2.9: Diagrams of crosswind range vs downwind range for lithics ( $2500 \text{ kg/m}^3$ ) of (a) 8 mm, (b) 16 mm, and (c) 32 mm diameter for units D, E, and F in the three scenarios considered. Horizontal grid lines indicate eruption column heights (in km) and diagonal grid lines wind velocity (in m/s) as theoretically calculated by Carey and Sparks (1986).

The Sparks *et al.* (1992) model relates the rate of decrease of sedimentation rate away from the vent to the column height. As the sedimentation rate is proportional to the thickness of the deposit by a factor of time, we used thickness relationships to determine the respective column heights. Natural log-plots of the thickness normalised to the extrapolated maximum thickness versus radial distance from vent for the three different scenarios are presented in Figure 2.10.

During the first plinian eruptive phase D, the average eruption column ranged in height between 22 and 26 km. 25 to 28 km are inferred for phase E, whereas phase F is similar to D; the eruption column is between 21 and 26 km. Lowest values are obtained in the no-wind scenario 1, which reflects the conditions the model is designed for.



For D and F, these average column heights are a few km lower than the maximum column heights estimated above, as they should be. The gradients of the data in Figure 2.10 agree well with model expectations. However, for unit E the average column height equals the maximum column height estimated above. Moreover, while the maximum clast approach suggests lowering of the eruption column during phase E compared to phases D and F, the sedimentation model implies the opposite behaviour. These inconsistencies shed some doubt on the applicability of the models to basaltic plinian tephra.

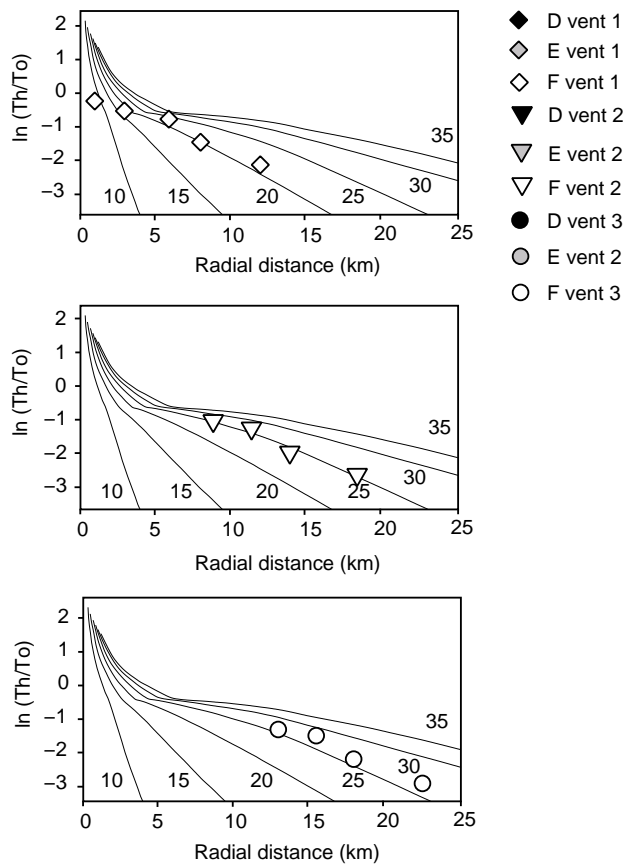


Figure 2.10: Natural log-plots of the thickness normalised to the extrapolated maximum thickness versus radial distance from vent for units D, E, and F in the three different scenarios, projected onto sedimentation rate decrease curves after Sparks *et al.* (1992). The curves reflect the expected average column heights.

## 2.5 Discussion and conclusion

### 2.5.1 Applicability of eruption models

The models of Pyle (1989); Carey and Sparks (1986); and Sparks *et al.* (1992), typically used for the determination of volume, column height and wind velocity at time of eruption have been mostly tested on rhyolitic to andesitic tephra-fall deposits. Therefore, the application of these models to Fontana Tephra provides interesting insights into their applicability to mafic plinian volcanism.

The volume results are very consistent for the three units (D, E, and F) and for the

three vent positions considered, in line with the suggestion that plotting the square root of the isopach area eliminates the effects of wind on the resulting contours for the volume calculation (Pyle 1989). Applying the model of Pyle (1989) to older deposits of limited exposure can underestimate the tephra volume for the reasons discussed by Bonadonna *et al.* (1998) and Rose (1993), but our data show that it can still give consistent results even in those situations where the position of the vent is uncertain. Our data suggest that the model can readily be applied to plinian fallout deposits of mafic composition. The resulting total volume of Fontana Tephra of 1.4 to 1.8 km<sup>3</sup> is much smaller than the estimate of 12 km<sup>3</sup> of Williams (1983b).

The results for eruptions column heights using the method of Carey and Sparks (1986) are more complex. Estimated column heights are internally consistent and are little influenced by the assumed vent position, which does, however, strongly affect estimated wind velocities. Deviations from the model curves such as of the Fontana data trends in Figure 2.8 had also been noted by Carey and Sparks (1986) in their data, with the most prominent deviation in the data of the 1886 AD Tarawera deposit, the product of another basaltic plinian eruption. They explained such deviation by the breakage of the larger clasts upon impact on the ground.

Carey and Sparks (1986) model the clast distribution assuming an eruption column reached a certain height. As far as clast dispersal from that height is concerned, the model is insensitive as to whether rhyolitic or basaltic magma was erupted. The difference in composition does, however, affect the modelled column height for any given discharge rate because basaltic magma, about 300 °C hotter than rhyolitic magma, provides greater buoyancy to the column. According to model results of Woods (1988), the basaltic column would be < 5 km higher than a rhyolitic one at otherwise identical conditions. The higher temperature of basaltic magma probably generates more vigorous turbulence to support particles in the eruption column so that the clast support envelopes calculated by Carey and Sparks (1986) may be minimum estimates in the case of basaltic magma eruption. The errors due to a basaltic composition involved in the above column height estimates for the Fontana eruption is, however, not larger than other, composition-independent uncertainties such as degree of ash-gas thermal disequilibrium or atmospheric properties (Sparks *et al.* 1997).

The plume-sedimentation model of Sparks *et al.* (1992) assumes an initial grain-size distribution which we cannot verify for Fontana Tephra. The underlying eruption column dynamics also would be affected to some extent by the higher temperature of basaltic magma. Most of all, however, cross-wind effects are not considered in the model but would shift the data in Figure 2.10 parallel to the distance axis. We have therefore only compared the gradients in the data with the gradients of the model curves, and reading column heights from Figure 2.10 is thus less precise than from Figure 2.9. The thickness decay patterns shown by the Fontana data are, however, quite compatible with the modelled results.

In summary, there are some uncertainties in comparing the Fontana field data with deposit properties derived from eruption column modelling. The observed deviations and uncertainties are, however, mainly due to deficiencies in the input parameters (e.g., ignorance of cross-wind) or in the field data (incomplete exposure) and less so to magma composition. Within the uncertainties that must be accepted with deposits of any composition, the models can be applied to basaltic plinian tephra to obtain approximate values of eruption parameters.

## 2.5.2 Conclusions

The dispersal characteristics of Fontana Tephra prove its deposition during a basaltic plinian eruption. This eruption evolved through seven phases that successively emplaced the depositional units A to G. Unsteady eruption phases at the beginning (units A to C) and end (unit G) of the eruption bracketed the major plinian activity producing units D to F. These are generally lithic-poor fallout of highly vesicular scoria lapilli but contain horizons in which distinct lithic lithologies, quench-rimmed scoria lapilli, and higher ash content attest to limited water access to an unstable conduit. Such transient disturbances could not, however, prevent the eruption from restoring stable plinian conditions. Due to a lack of proximal outcrop sites, the position of the eruptive vent for Fontana Tephra remains uncertain but is possibly not within the Masaya caldera, as previously favored. We prefer vent 2 in Figures 2.4 and 2.5 as the site most compatible with the observed tephra distribution. Based on this scenario, the eruption of the major units D, E, and F took place at wind velocities of 10-15 m/s, and the total erupted volume of all units amounts to

at least 1.4 km<sup>3</sup>. The eruption column peaked at 29-30 km height during phase D, slightly waned to 25-27 km for phase E, then reached 28 km in phase F (applying the method of Carey and Sparks 1986).

The Fontana plinian eruption was a multi-phase event that also produced pyroclastic surges extending to at least 7 km around the vent. Due to their extremely rapid lateral movement largely independent of wind velocity or direction, they endanger areas in all directions from the vent (Cas and Wright 1988). Younger basaltic plinian eruptions of the Masaya area (Perez and Freundt this volume) produced even larger surges, and show that basaltic plinian activity is not really that unusual in this volcanic setting.

The densely-populated greater Managua area, located down the prevailing winds from the Fontana source area, accommodates roughly two million people, of which more than one million live in the capital. The entire area is subject to intense population growth. Furthermore, volcano tourism is bringing increasing numbers of visitors into Masaya Caldera. The Fontana eruption led to devastation of the greater Managua region by emplacement of a several meter-thick tephra sheet, more than one meter was emplaced in the capital city itself. This is likely to happen again during future similar eruptions. Moreover, the repeated temporary waning or cessation of eruptive activity that mafic plinian eruptions show, might mislead the authorities to premature lowering of alert levels, and subsequent re-awakening or intensifying of activity might come unexpectedly.

Because such eruptions are considered atypical and not much is known about possible unrest prior to eruption, their precursors may be misinterpreted as the forerunners to relatively weak strombolian activity. The risk to communities is exacerbated because the low-viscosity of mafic magmas ascend considerably faster than their acidic counterparts (Houghton *et al.* 2004). The rapid ascent rate means that the warning time, i.e. the time elapsing between potential precursory signals and the onset of the basaltic plinian eruption, will be extremely short; Houghton *et al.* (2004) estimated it at a few hours for Tarawera 1886 AD. Taken together, Fontana Tephra, younger deposits from Masaya Caldera (Perez and Freundt this volume), and the abundance of apparently widespread mafic lapilli beds observed during reconnaissance of the Las Sierras Formation, indicate that mafic plinian-magnitude eruptions

may be a rather common exception to the rule in the Masaya area. This amplifies the need for a well-established volcano monitoring with particular regard to early-warning systems.

### **Acknowledgements**

Strong thanks are due to the staff of INETER in Managua for their enthusiastic support during our extensive field work. CB and BFH were funded by NSF-EAR-0310096 and NSF-EAR-0125719. Radiocarbon dates were generated at Leibniz Laboratory for Radiometric Dating and Stable Isotope Research, University of Kiel, Germany. This publication is contribution # 71 to the Sonderforschungsbereich 574 "Volatiles and Fluids in Subduction Zones" at University of Kiel.



# Bibliography

- [1] Bice, D.C. (1980): *Tephra Stratigraphy and Physical Aspects of Recent Volcanism Near Managua, Nicaragua*. Unpubl. PhD thesis, Univ. of California, Berkeley, 422 p.
- [2] Bice, D.C. (1985): Quaternary volcanic stratigraphy of Managua, Nicaragua: Correlation and source assignment for multiple overlapping plinian deposits. *Geological Society of America Bulletin* 96, 553–566.
- [3] Bonadonna, C., Ernst, G.G.J., and Sparks, R.S.J. (1998): Thickness variations and volume estimates of tephra fall deposits: the importance of particle Reynolds number. *Journal of Volcanology and Geothermal Research* 81/3–4, 173–187.
- [4] Bonadonna, C. and Phillips, J.C. (2003): Sedimentation from strong volcanic plumes. *Journal of Geophysical Research* 108/B7, 2340, 5–1.
- [5] Bonadonna, C. and Houghton, B.F. (in press): Total grainsize distribution and volume of tephra-fall deposits. *Bulletin of Volcanology*.
- [6] Cas, R.A.F. and Wright, J.V. (1988): *Volcanic Successions - modern and ancient*. London, 528 p.
- [7] Carey, S. and Sparks, R.S.J. (1986): Quantitative models of the fallout and dispersal of tephra from volcanic eruption columns. *Bulletin of Volcanology* 48, 109–125.
- [8] Coltelli, M., Del Carlo, P., and Vezzoli, L. (1998): Discovery of a Plinian basaltic eruption of Roman age at Etna volcano, Italy. *Geology* 26/12, 1095–1098.

- [9] Head, J.W. and Wilson, L. (1987): Lava fountain heights at Pu'u O'o, Kilauea, Hawaii: indicators of amount and variations of exsolved magma volatiles. *Journal of Geophysical Research* 92, 13715–13719.
- [10] Houghton, B.F., Wilson, C.J.N., and Pyle, D.M. (2000): Pyroclastic fall deposits. In: Sigurdsson, H. *et al.* (eds.) *Encyclopedia of Volcanoes*, Academic Press, San Diego, 555–570.
- [11] Houghton, B.F., Wilson, C.J.N., Del Carlo, P., Coltelli, M., Sable, J.E., and Carey, R. (2004): The influence of conduit processes on changes in style of basaltic Plinian eruptions: Tarawera 1886 and Etna 122 BC. *Journal of Volcanology and Geothermal Research* 1137, 1–14.
- [12] Jaupart C. (2000): Magma ascent at shallow levels. In: Sigurdsson, H. *et al.* (eds.) *Encyclopedia of Volcanoes*, Academic Press, San Diego, 237–245.
- [13] Jaupart, C. and Vergnolle, S. (1989): The generation and collapse foam layer at the roof of a basaltic magma chamber. *Journal of Fluid Mechanics* 203, 347–380.
- [14] Kutterolf, S., Freundt, A., Wehrmann, H., Perez, W., Schmincke, H.-U., and Strauch, W. (in prep.): 40,000 years of highly explosive eruptions around Managua, Nicaragua: time sequence, eruption dynamics, and hazard implications. *Bulletin of Volcanology*.
- [15] Mangan, M.T. and Cashman, K.V. (1996): The structure of basaltic scoria and reticulite and inferences for vesiculation, foam formation, and fragmentation in lava fountains. *Journal of Volcanology and Geothermal Research* 73/1–2, 1–18.
- [16] Mangan, M.T., Cashman K.V., and Newman S. (1993): Vesiculation of basaltic magma during eruption. *Geology* 21, 157–160.
- [17] McBirney, A. and Williams, H. (1965): *Volcanic history of Nicaragua*. Univ. of California Publications in Geological Sciences 55, Berkeley, 65 p.
- [18] Papale, P. and Rosi, M. (1993): A case of no-wind plinian fallout at Pulu-lagua caldera (Ecuador): implications for model of clast dispersal. *Bulletin of Volcanology* 55, 523–535.

- [19] Parfitt, E. (2004): A discussion of the mechanisms of explosive basaltic eruptions. *Journal of Volcanology and Geothermal Research* 134, 77–107.
- [20] Parfitt, E.A. and Wilson, L. (1995): Explosive volcanic eruptions - IX: The transition between Hawaiian-style lava fountaining and Strombolian explosive activity. *Geophysical Journal International* 121, 226–232.
- [21] Perez, W. and Freundt, A. (this volume): The youngest highly explosive basaltic eruptions from Masaya Caldera Complex (Nicaragua): stratigraphy and hazard assessment.
- [22] Pyle, D.M. (1989): The thickness, volume and grainsize of tephra fall deposits. *Bulletin of Volcanology* 51, 1–15.
- [23] Pyle, D.M. (1995): Assessment of the minimum volume of tephra fall deposits. *Journal of Volcanology and Geothermal Research* 69, 379–382.
- [24] Pyle, D.M. (2000): Sizes of volcanic eruptions. In: Sigurdsson H. *et al.* (eds.): *Encyclopedia of volcanoes*, Academic Press, San Diego, 263–269.
- [25] Rymer, H., van Wyk de Vries, B., Stix, J., and Williams-Jones, G. (1998): Pit crater structure and processes governing persistent activity at Masaya Volcano, Nicaragua. *Bulletin of Volcanology* 59, 345–355.
- [26] Rose, W.I. (1993): Comment on another look at the calculation of fallout tephra volumes. *Bulletin of Volcanology* 55, 372–374.
- [27] Seyfried, R. and Freundt, A. (2000): Analog experiments on conduit flow, eruption behaviour, and tremor of basaltic volcanic eruptions. *Journal of Geophysical Research* 105, 23727–23740.
- [28] Simkin, T. and Siebert, L. (1994): *Volcanoes of the World*: Smithsonian Institution and Geoscience Press, 349 p.
- [29] Sparks, R.S.J. (1986): The dimensions and dynamics of volcanic eruption columns. *Bulletin of Volcanology* 48, 3–15.
- [30] Sparks, R.S.J., Bursik, M.I., Ablay, G.J., Thomas, R.M.E., and Carey, S.N. (1992): Sedimentation of tephra by volcanic plumes. Part 2: controls on thickness and grain-size variations of tephra fall deposits. *Bulletin of Volcanology* 54, 685–695.

- [31] Sparks, R.S.J., Bursik, M.I., Carey, S.N. Gilbert, J.S., Glaze, L.S., Sigurdson, H., and Woods, A.W. (1997): *Volcanic Plumes*, 574 p., John Wiley, New York.
- [32] Van Wyk de Vries, B. (1993): *Tectonics and magma evolution of Nicaraguan volcanic systems*. PhD thesis, Open University, Milton Keynes, UK.
- [33] Vergnolle, S. and Jaupart, C. (1986): Separated two-phase flow and basaltic eruptions. *Journal of Geophysical Research* 91/B 12842–12860.
- [34] Walker, G.P.L. (1973): Explosive volcanic eruptions - a new classification scheme. *Geologische Rundschau* 62, 431–446.
- [35] Walker, G.P.L., Self, S., and Wilson, L. (1984): Tarawera, 1886, New Zealand - A basaltic Plinian fissure eruption. *Journal of Volcanology and Geothermal Research* 21, 61–78.
- [36] Walker, J.A., Williams, S.N., Kalamarides, R.I., and Feigerson, M.D. (1993): Shallow open-system evolution of basaltic magma beneath a subduction zone volcano: the Masaya Caldera Complex, Nicaragua. *Journal of Volcanology and Geothermal Research* 56, 379–400.
- [37] Williams, S.N. (1983a): *Geology and Eruptive Mechanisms of Masaya Caldera Complex, Nicaragua*. Unpubl. PhD thesis, Dartmouth College, Hanover, New Hampshire, 03755 USA.
- [38] Williams, S.N. (1983b): Plinian airfall deposits of basaltic composition. *Geology* 11, 211–214.
- [39] Wilson, L. and Head, J.W. (1981): Ascent and eruption of basaltic magma on the earth and moon. *Journal of Geophysical Research* 86, 2971–3001.
- [40] Woods, A. W. (1988): The fluid dynamics and thermodynamics of eruption columns. *Bulletin of Volcanology* 50, 169–193.



## **Chapter 3**

# **Water, halogen, and sulphur degassing during the basaltic-andesitic plinian eruption of Fontana Tephra, Nicaragua**

**Heidi Wehrmann<sup>1</sup>, Armin Freundt<sup>1,2</sup>, Steffen Kutterolf<sup>1</sup>, Michael Wiedenbeck<sup>3</sup>,  
Hans-Ulrich Schmincke<sup>2</sup>**

1. SFB 574 at Kiel University, Wischhofstr. 1-3, 24148 Kiel, Germany
2. IfM-GEOMAR, RD4, Wischhofstr. 1-3, 24148 Kiel, Germany
3. GeoForschungszentrum Potsdam, Telegrafenberg C161, 14473 Potsdam

## Abstract

Fontana Tephra (1.1 Gt DRE) has been generated by a basaltic-andesitic plinian eruption in the Masaya-Managua area in west-central Nicaragua at the Central American subduction zone. Plinian episodes of the eruption alternated with phreato-magmatically-affected plinian and subplinian pulses.

Water, fluorine, chlorine, and sulphur concentrations in melt inclusions in phenocrysts, and scoria matrix glasses were determined by Secondary Ion Mass Spectrometry (SIMS). Emission of gases during the plinian and subplinian phases of the Fontana eruption are estimated at 7 Mt H<sub>2</sub>O, 30 kt F, 160 kt Cl, and 280 kt S by the petrologic method. The gas release varies through the successive eruptive phases, tending to increase as the eruption proceeds. Exsolution of F and Cl is coupled with the water release. The halogen fluid-melt distribution coefficients ( $D^{f/m}$ ) calculated from the data range at 12–18 for F, and at 7–30 for Cl. No systematic relationship between the composition and amounts of gases released and the eruptive style was found. The changes in eruptive style appear to have been governed by oscillating access of external water to the conduit. The fragmentation level as inferred from residual melt water contents fluctuated at shallow depths between 30 and 150 m below the surface. In contrast, the observed scoria vesicularities of 68–72 % indicate a greater fragmentation depth of 165–195 m, when assuming equilibrium degassing. This discrepancy is interpreted to reflect delayed disequilibrium degassing forced by predominantly homogeneous bubble nucleation requiring substantial supersaturation. This scenario is supported by the absence of microlites suitable as bubble nucleation sites. We infer that this late, catastrophic bubble nucleation combined with rapid ascent of the magma was responsible for the unusual plinian style of the mafic Fontana eruption.

**Keywords:** mafic plinian eruption, volatile degassing, distribution coefficient, bubble nucleation, fragmentation level

## **3.1 Introduction**

### **3.1.1 Volatiles**

Magmatic volatiles play a key role in controlling the dynamics of explosive volcanism. Degassing of water is the major driving force of volcanic eruptions. It strongly affects the physical properties of the melt by the manner and extent vesicles form, governing the pressure conditions in the conduit, and consequently the fragmentation regime. Degassing of volatiles such as fluorine, chlorine, and sulphur may substantially affect atmospheric chemistry. Plinian eruptions during which volatiles are injected high into the stratosphere may therefore have climatic effects (e.g. Brasseur 1992).

Here we will document volatile emissions of the large basaltic-andesitic plinian Fontana eruption in west-central Nicaragua, and the role of the volatiles in governing the eruption mechanism. Water exsolution is of particular interest in this case, since the reason for the highly explosive eruptive behaviour of mafic magmas is still poorly understood.

### **3.1.2 The Fontana eruption**

Fontana Tephra is a widespread fan of basaltic-andesitic scoria lapilli that was deposited by a Late-Pleistocene, highly explosive eruption from a vent in the Masaya area (Nicaragua) (Figure 3.1). This region is part of the Central American Volcanic Arc (CAVA), one of the most active subduction zones of the Earth (Walker *et al.* 2003). The c. 30 km thick crust of the Cocos plate is subducted beneath the Caribbean plate.

The Fontana eruption displayed a fairly wide range of eruptive styles and intensities (Figure 3.2). The eruption started with several short, but highly explosive pulses, emplacing well-bedded layers of hawaiian-type (unit A) and highly-vesicular scoria lapilli (unit B). Then a violent surge was released, simultaneous with continuing fallout activity (unit C), giving way to a longer-duration plinian event (unit D) that included weak pulses of ash emission. Subsequently, interaction with near-surface groundwater affected the next plinian fallout phase (unit E), which in turn was followed by a second long-lasting dry plinian episode (unit F). The eruption ended with



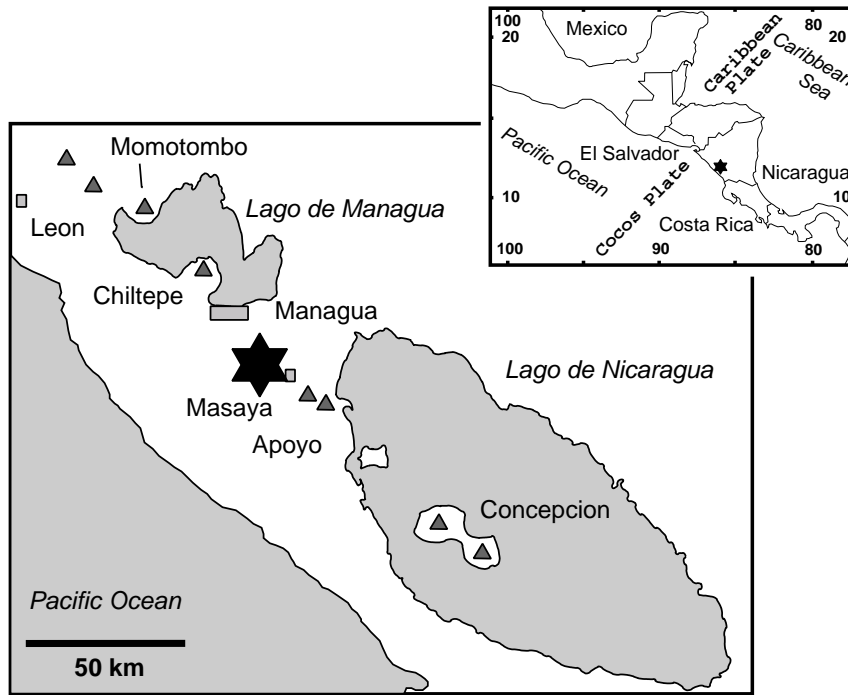


Figure 3.1: Map of Central America (inset) and west-central Nicaragua, showing the Fontana Tephra vent location (black star). Major volcanic centres are marked by triangles.

a succession of short, but widely distributed subplinian pulses variably affected by interaction with water (unit G). Wehrmann *et al.* (subm.) discuss the evolution of the eruption in more detail. These authors determined eruption column heights of 24–30 km during the main plinian phases that produced  $0.8 \text{ km}^3$  of the total erupted tephra volume of  $1.4 \text{ km}^3$  (1.1 Gt DRE).

## 3.2 Methods

### 3.2.1 Sampling and sample preparation

Fresh scoria clasts were taken from the stratigraphic units of the plinian and subplinian fallout deposits, representing successive phases of the eruption sequence. We determined the compositions of bulk rock, matrix glass, phenocrysts, and melt inclusions in the phenocrysts.

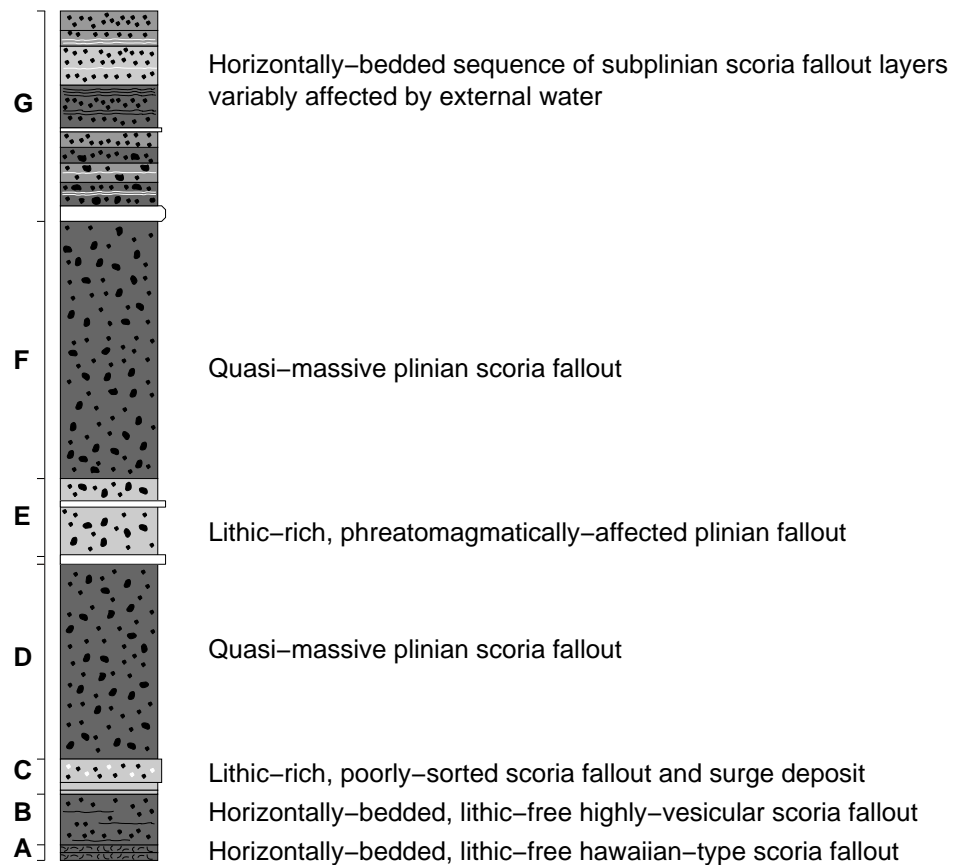


Figure 3.2: Generalised stratigraphic column of Fontana Tephra units illustrating changes in eruptive style.

We restricted our measurements of melt inclusions to those that are dominated by glass (i.e. more than 90%) and are not visibly affected by cracks. Most analysed inclusions were free of daughter crystals, and contained, if any, only small shrinkage bubbles. The melt inclusions were not reheated prior to analysis. The predominant host mineral phase was bytownite. A minor amount of olivine-hosted inclusions were also analysed. Clear and fresh glass shards were selected for matrix glass analyses.

### 3.2.2 Electron microprobe analyses (EMA)

Chemical analyses of major elements, and fluorine, chlorine, and sulphur were carried out on polished thin sections of the scoria clasts, using a CAMECA SX 50 wavelength dispersive electron microprobe at IfM-Geomar, Kiel. Major element compositions of melt inclusions and matrix glass were determined at 15 kV accelerating voltage and a beam current of 10 nA, with counting times of 20 s. The beam was defocused to 10  $\mu\text{m}$  to minimise analytical Na loss. Data were normalised on a water-free basis. Analytical conditions for volatile elements were 15 kV, and 30 nA; counting times were increased to 60 s to optimise analytical precision. For analyses of plagioclase and clinopyroxene, conditions were set to 15 kV, 20 nA, and 20 s. The beam current was increased to 30 nA at a voltage of 15 kV for olivines.

### 3.2.3 Secondary ion mass spectrometry (SIMS)

The concentrations of H, C, F, S, Cl and Br were measured with the Cameca ims 6f SIMS at the GeoForschungsZentrum Potsdam, using a 10 kV, 1 nA  $^{133}\text{Cs}^+$  primary beam focused to a c. 10  $\mu\text{m}$  diameter on the polished sample surface. Prior to analysis the epoxy-embedded samples of hand-picked crystals and glass shards were ultrasonically cleaned in high-purity ethanol, coated with 35 nm gold, and stored for several days in the instruments' multi-sample, high-vacuum air lock. The instrument was operated at high mass resolving power of  $M/dM$  4500 which is required to remove isobaric molecular interferences from the bromine peak. Charge compensation employ electron flood using a normal incidence electron flood gun. The approach unfortunately results in an elevated hydrogen background signal which was partially suppressed by employing a 60  $\mu\text{m}$  diameter field-of-view aperture. The instrument was operated with a 50 V energy band pass to which no offset was applied.

The actual analyses used the peak stepping sequence 0.95 background (0.1 s integration),  $^1\text{H}$  (4 s)  $^{12}\text{C}$  (10 s),  $^{19}\text{F}$  (2 s),  $^{30}\text{Si}$  (2 s),  $^{32}\text{S}$  (4 s),  $^{35}\text{Cl}$  (2 s) and  $^{81}\text{B}$  (4 s). Twenty cycles of this sequence, along with a three minute, unrastered preburn, resulted in a total analysis time of 18 minutes. We did not have a single glass reference sample characterised for all of the target elements and therefore employed a suite of calibrants. These reference samples were analysed to determine the relative sensitivity factors (rsf) for the various elements against  $^{30}\text{Si}$  at the beginning and end of each day; the day to day reproducibility was acceptable over the six-day analytical

run. The rsf for H<sub>2</sub>O was calculated based on measurements of a 1833-11 reference material; the standard deviation of the analyses was below 20 %. For the rsf of F, S, and Cl we employed a TRD-80 reference material, which was compositionally the most similar to our samples. The analytical standard deviations were 12.5 % for F, and 8 % for both S and Cl. Four other reference materials (CFA 47, P103-2, 1840-3, and WOK 16-2) were kept in the analytical run to keep additional control on the data quality; a SCO olivine was used for background monitoring. The carbon concentration numbers proved unusable due to sample surface contamination, and, therefore, these data are not presented here. This contamination was presumably related to the epoxy which had to be used to embed and polish the porous samples.

### **3.3 Volatiles**

#### **3.3.1 Melt composition and crystallinity**

Most scoria clasts are composed of clear, microlite-free to microlite-poor brown glass, although some scoria clasts contain moderate amounts of microlites in the matrix glass. Phenocrysts and glomerocrysts constitute less than 5 modal %. Bytownite is the most common mineral phase. Bytownite phenocrysts are euhedral to subhedral, and reach sizes of 1 mm, averaging 0.3-0.5 mm. Most bytownites contain many melt inclusions, irregularly distributed in the crystals. Olivine and clinopyroxene occur in minor amounts ( $\ll$  1 %). These crystals are generally small (0.1 mm), rarely up to 0.7 mm. Singular melt inclusions were observed in olivine crystals, while clinopyroxenes tend to be melt inclusion free. Neither Fe-Ti oxides, nor any hydrous mineral phases have been found. The texture of the scoria clasts ranges from highly vesicular with spherical to elongated bubbles to moderate to highly vesicular with irregularly shaped, deformed and coalesced bubbles.

The Fontana magma, when normalised to anhydrous composition, is a basaltic andesite. Samples from different stratigraphic heights in the deposit do not vary in major and trace element concentrations. Moreover, major-element compositional differences between melt inclusions and matrix glass are limited: the melt inclusions show slightly elevated MgO and K<sub>2</sub>O (Figure 3.3a), and slightly lower Na<sub>2</sub>O and CaO concentrations compared to the matrix glass. SiO<sub>2</sub> and FeO concentrations of inclusions and matrix glasses are identical (Figure 3.3b), suggesting that only

minor bulk crystallisation occurred between melt inclusion entrapment and eruption. The Fontana magma is the product of differentiation along a tholeiitic trend as derived from the alkali-iron-magnesium ratios. Melt inclusions in bytownite and olivine are chemically indistinguishable, indicating that plagioclase co-precipitated with olivine.

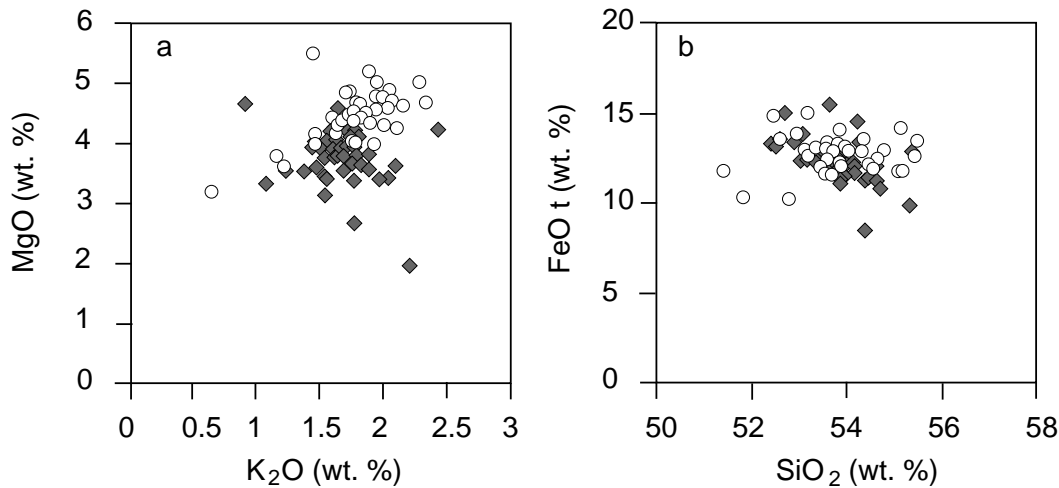


Figure 3.3: Major element variation diagrams for melt inclusions (open circles) and matrix glasses (filled diamonds) of Fontana Tephra, showing that only limited magma differentiation occurred between melt inclusion entrapment and eruption.

### 3.3.2 Quantification of volatile release

We have applied the "petrologic method" to assess the amount of volatiles released during the Fontana eruption: gas emissions are calculated by comparing the volatile content of undegassed and degassed quenched melts. Melt inclusions in minerals reflect the composition of the magma at the time of crystallisation of the respective host mineral phase at the reservoir pressure, while matrix glasses represent the melt fraction degassed during eruption. This difference is then scaled by the mass of the magma erupted during the respective eruptive phase. The petrologic method is currently the only method available for quantifying the gas output of past eruptions. The total sulphur output is generally underestimated. The values presented here should therefore be considered as minimum estimates. However, as the discrepancy between the gas emission inferred from satellite observations and that derived

by the petrologic method strongly decreases from rhyolitic towards mafic magmas (Wallace 2001), the underestimation may be minor for the Fontana eruption.

### **Water**

The release of water, based on average concentrations, varies at the different eruptive stages (Figure 3.4a). In the first two phases of the plinian activity (units D and E), water emission makes up c. 0.65 wt. % of the magma erupted, then culminates to 0.8 wt. % in the third plinian phase (unit F), followed by a slight lowering to 0.75 wt. % during the terminal subplinian activity (unit G). These variations are a result of average initial melt water concentrations rising from 1 wt. % to 1.2 wt. %. All samples show average residual water contents of 0.36 wt. %; standard deviations around the mean are c. 20 %.

### **Fluorine**

Little difference is discernible between F concentrations in inclusion glass and matrix glass in the lower dry plinian deposit (unit D), suggesting that insignificant amounts of the fluorine exsolved in the first plinian eruptive phase. Values for both melt inclusions and matrix glasses range between 300 ppm and 500 ppm, with a standard deviation of c. 30 %. As the eruption proceeds, a slight and progressively increasing F degassing can be noted. The data scatter is much smaller (3–15 %), melt inclusion F abundances rise from average 350 ppm to 440 ppm, while matrix glasses augment to a lesser extent from average 320 ppm to 380 ppm (Figure 3.4b).

### **Chlorine**

Chlorine abundances as measured by ion microprobe show some scatter, but the data agree well with the values obtained by electron microprobe. Concentrations range between 900 and 1600 ppm for the melt inclusions, and between 800 and 1500 ppm for the matrix glasses. Initial melt Cl contents, as well as the total Cl release show a gradual increase stratigraphically upwards, while the residual Cl in the melt is highest in the two dry plinian eruptive phases (units D and F), and lowest in the water-affected plinian phase (unit E) (Figure 3.4c).

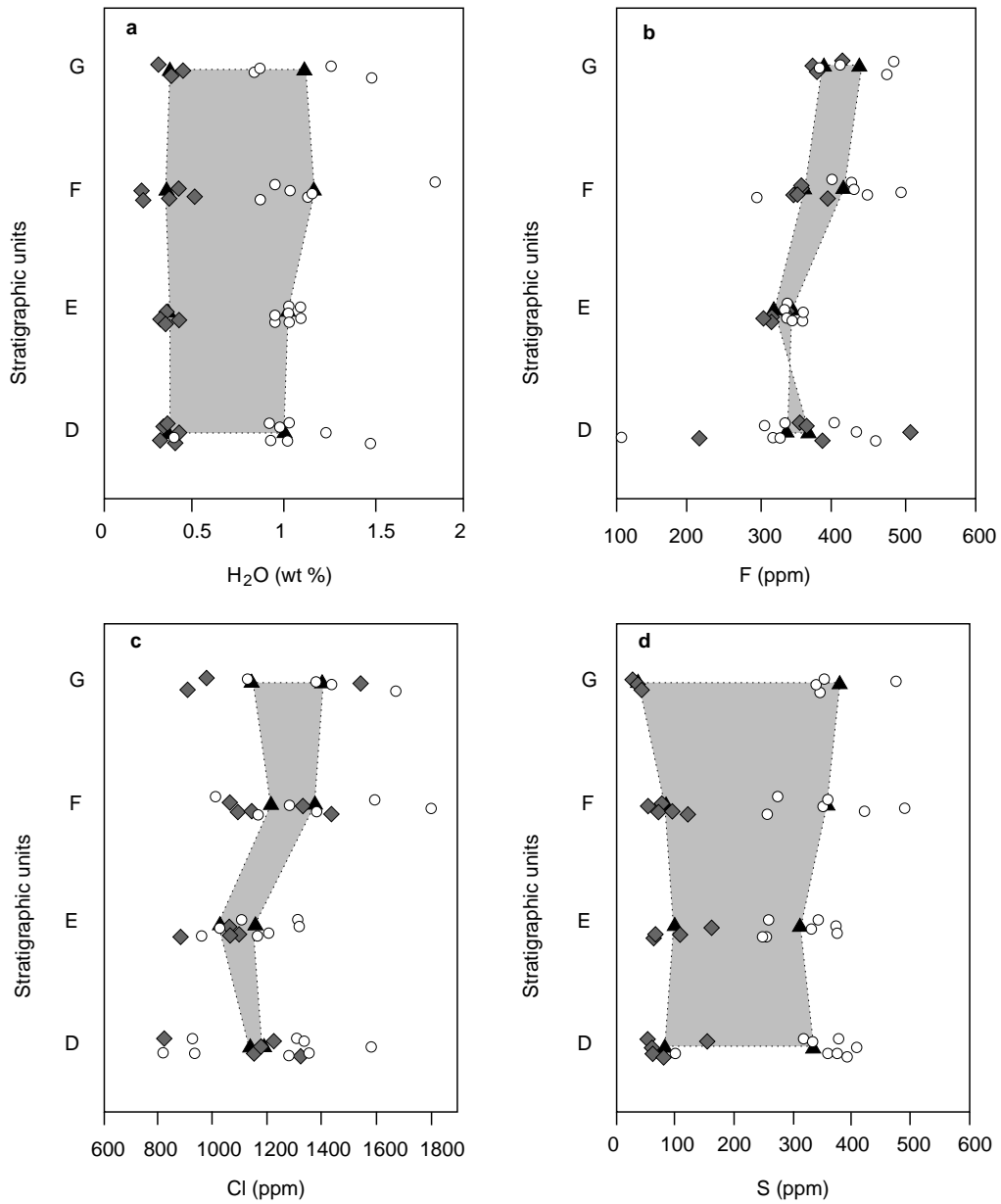


Figure 3.4: Concentrations of (a) H<sub>2</sub>O, (b) F, (c) Cl, and (d) S in melt inclusion (open circles) and matrix glasses (filled diamonds). Triangles indicate the respective average concentrations. The difference (shaded area) between the average concentrations represents the volatile fraction released during the respective eruptive phases. Note the different scales.

## Sulphur

The concentrations of sulphur, measured by ion microprobe, reach 250–490 ppm in the melt inclusions throughout the eruptive sequence; values tend to be somewhat higher in upper stratigraphic levels. Matrix glasses are degassed to c. 80 ppm in the dry plinian deposits (units D and F), while they remain at 60–160 ppm in the external-water affected plinian layer (unit E). S-degassing is strongest in the terminal subplinian phase (unit G), of which matrix glass values are as low as 30 ppm (Figure 3.4d).

## Total gas release

Multiplying the percentages of volatile emission with the respective erupted masses of the deposit's subunits leads to the total volatile output. These data are summarised in Table 3.1. Overall, the largest part of the total gas release can be credited to the long-lasting terminal subplinian activity, that also represent the relative strongest emission of S and Cl. Relative water and fluorine release, in contrast, peaked during the third (dry) plinian phase, while the first plinian phase shows lowest values for absolute as well as relative F and Cl emission quantities. There is a covariation between the release of F and Cl with H<sub>2</sub>O in the successive eruption phases, indicating partitioning of F and Cl into an aqueous fluid phase (Figure 3.5).

Table 3.1: Gas release (kt) during the consecutive phases of the eruption.

	Water	Fluorine	Chlorine	Sulphur
D	1490	0	12.2	58.4
E	840	3.3	16.3	26.7
F	2050	13.7	39.8	68.3
G	2660	17.6	92.4	122.6
<b>Total</b>	<b>7040</b>	<b>34.6</b>	<b>160.7</b>	<b>276.0</b>

## 3.4 Volatile solubility and exsolution conditions

Some volatile species, such as water, exsolve from the melt and partition into a fluid or gas phase upon supersaturation. Supersaturation is achieved when (1) the



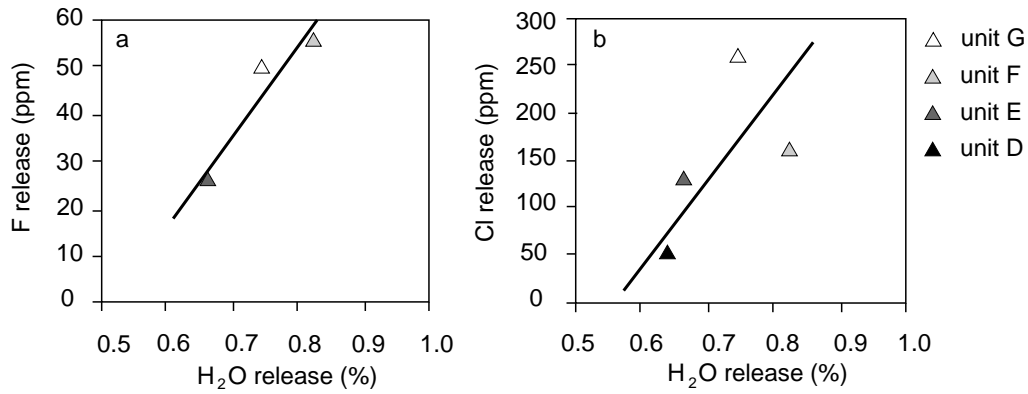


Figure 3.5: Diagrams of released (a) F, (b) Cl fractions versus degassed water fraction. The covariation underscores partitioning of the halogens into the aqueous fluid phase.

magma decompresses during ascent, and (2) when volatile-free crystals fractionate from the melt, which therefore experiences a relative enrichment of those volatiles. Other volatiles, such as F and Cl partition into a fluid phase as soon as it becomes available, irrespective of their saturation state. In the following section, we will illuminate several aspects of degassing dynamics of the various volatile species that were analysed during the course of this study.

### 3.4.1 Magma chamber conditions - temperature and pressure

Magma chamber temperatures can be calculated based on the melt MgO and Al<sub>2</sub>O<sub>3</sub> mole fractions applying the formula  $T (^{\circ}\text{C}) = 1348 X_{\text{MgO}} + 1069 X_{\text{Al}_2\text{O}_3} + 935.1$  (Wallace and Carmichael 1992). This geothermometer yields a temperature between 1118 and 1146 °C for the Fontana magma chamber, averaging at 1130 °C. Another approach to determine the magma chamber temperature relates the melt water contents to the major element melt composition at assumed pressure conditions (Sisson and Grove 1993). The clinopyroxene–melt geobarometer of Putirka (1996; 2003) yields magma chamber pressures of 220–370 MPa. For this pressure range and melt inclusion water contents, the Fontana melt had a temperature between 1077 °C and 1140 °C.

Application of the clinopyroxene–melt, olivine–melt, and plagioclase–melt geother-

ometers of Putirka (2003) leads to a temperature evolution from 1125–1141 °C at the time of clinopyroxene crystallisation through c. 1090 °C at the time of olivine crystallisation to 1037–1069 °C for plagioclase crystallisation. In summary, the Fontana magma had a temperature of c. 1150 °C at depth to c. 1070 °C when it began to erupt.

### 3.4.2 Water saturated reservoir?

The solubility of water has been calculated by the method of Moore *et al.* (1998), which renders water solubility curves through a defined pressure range at assumed magma chamber temperatures, for a given major element magma composition. For the Fontana melt, the initial melt water contents as measured by SIMS have been projected onto these solubility curves, giving that water saturation was reached at a pressure of at least 3–35 MPa (Figure 3.6). Since the magma chamber pressure exceeded this value by an order of magnitude, the melt in the reservoir was strongly water undersaturated. Saturation was reached at lower pressure when the magma ascended to shallower levels in the crust, which will be further discussed below.

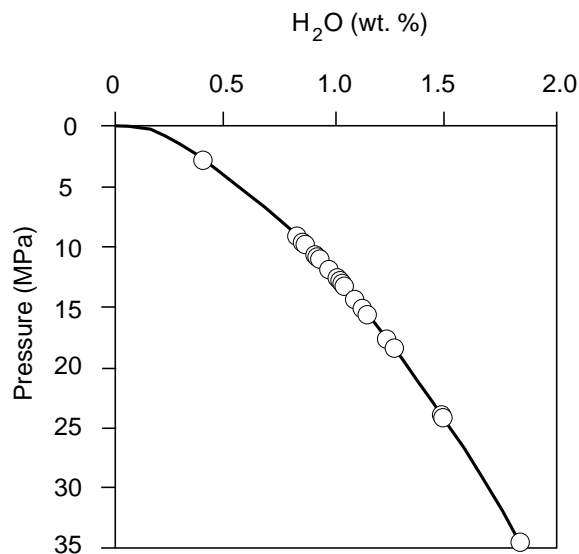


Figure 3.6: H<sub>2</sub>O saturation pressure derived from melt inclusion water contents, calculated after Moore *et al.* (1998).

### 3.4.3 Fluorine release?

The observation of no fluorine release in the lowest plinian unit (D) of Fontana Tephra agrees well with data of e.g. Villemant and Boudon (1999), who were able to show that F was not involved into magmatic degassing processes of the 650 a BP Mt. Pelee eruption. However, Fontana Tephra displays an increase of fluorine release upwards through the deposit from 0 ppm to 60 ppm. As shown in Figure 3.5a, the F exsolution during the later phases of the eruption (units E-G) linearly correlates with the water release. Fluid-melt partition coefficients  $D^{f/m}$  have been calculated from the ratio of the F concentration in the fluid,  $C_F^f$ , to the F concentration in the melt,  $C_F^m$ . The  $C_F^f$ -values were derived from the amounts of volatiles released during eruption as quantified above: the released water is considered to represent the amount of aqueous fluid phase present prior to eruption, and the fraction of F that exsolved from the melt is considered to have entirely partitioned into this aqueous fluid phase.  $C_F^m$ -values are provided by the measured melt inclusion F concentrations. For the consecutive later phases (units E-G) of the Fontana eruption, the  $D^{f/m}$ -values rise from 12.1 to 18.3; although the total F release of the entire eruptive sequence in relation to the total formation of an aqueous fluid leads only to a distribution coefficient of 11; still much higher than that of  $<1$  reported by Villemant and Boudon (1999).

### 3.4.4 Chlorine partitioning

We have calculated the Cl-solubility in anhydrous Fontana melt at 0.1 MPa and at 200 MPa, after Webster *et al.* (1999). The measured melt inclusion Cl contents of the Fontana magma remain by at least a factor of five below the solubility limits (Figure 3.7). Despite the strong undersaturation in the Fontana melt, we observe a release of Cl during the eruption as described in section 3.3.2. Like F, the Cl exsolution during eruption shows a linear covariance with the water fractionation (Figure 3.5b). The fraction of released Cl per fraction degassed water is about twice as high than for F, indicating a higher partition coefficient. Still, partitioning of Cl into the aqueous fluid phase remains incomplete, and c. 87 % of the initial Cl have been retained in the melt. Fluid-melt partition coefficients of Cl calculated from our data range between 7 and 29 for the successive eruptive phases, with a balance of 20 for the entire eruption. This corresponds to about 2 % of Cl in the fluid.

These  $D^{f/m}$ -values agree well with those of "roughly 20" presented by Gerlach *et al.* (1996) for the dacitic 1991 AD Pinatubo eruption, and that of 8.1 experimentally derived by Bureau *et al.* (2000) in albite melts. Webster (1992) presented a set of  $D^{f/m}$  values ranging from 8.4 to 200. All of the literature values presented above, except those of Pinatubo, are derived from evolved melts with  $H_2O$  contents significantly higher (several wt. %) than that of Fontana Tephra. The  $D^{f/m}$ -values of the Fontana melt are presented here to provide examples for a natural basaltic-andesitic eruption.

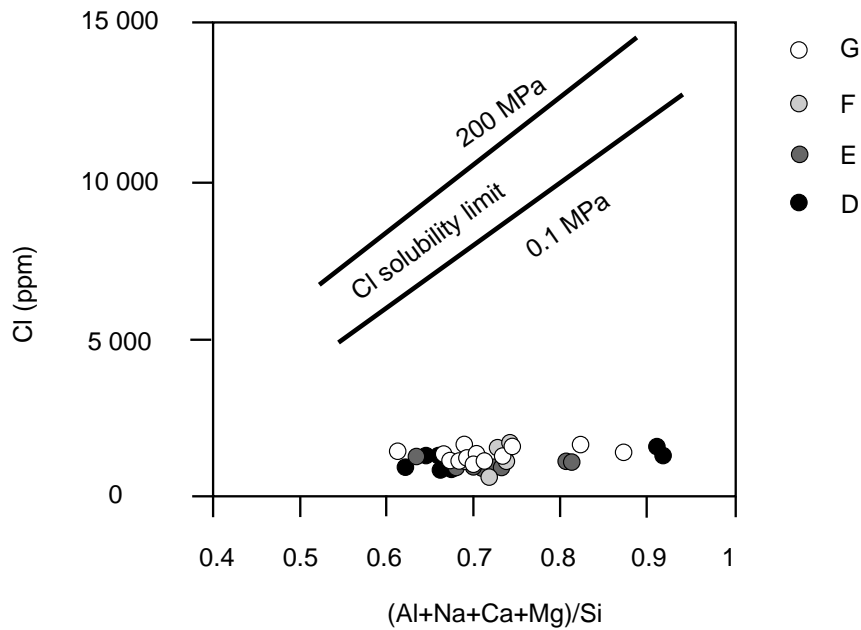


Figure 3.7: Measured melt inclusions Cl concentrations (circles) in relation to calculated Cl-solubility calculated after Webster *et al.* (1999), illustrating that the initially dissolved Cl in the Fontana melt was much below the dry melt solubility limit.

### 3.4.5 Excess sulphur?

With the support of remote sensing observations it has been shown that many eruptions release amounts of sulphuric gases that greatly exceed the estimates from the petrologic method. This results from a sulphurous fluid phase that had been present in the melt at the time of melt inclusion entrapment (e.g. Westrich and Gerlach

1992; Wallace 2001). Generally, it remains difficult to determine if such fluid existed, and it is yet unknown to what extent accumulation of S vapour in the preeruptive melt is common. Figure 3.8 depicts the discrepancy between S release estimates via remote sensing techniques and conventional petrologic method for various recent eruptions over a range of magma compositions (Wallace 2001). If these trendlines are applicable to Fontana Tephra, the S emission of the Fontana eruption as estimated from the petrologic method is by about one order of magnitude lower than petrologically predicted for a basaltic-andesitic eruption of such volume. Furthermore, this comparison supports the presence of an unknown amount of a free sulphurous fluid, and therefore S saturation in the Fontana magma reservoir.

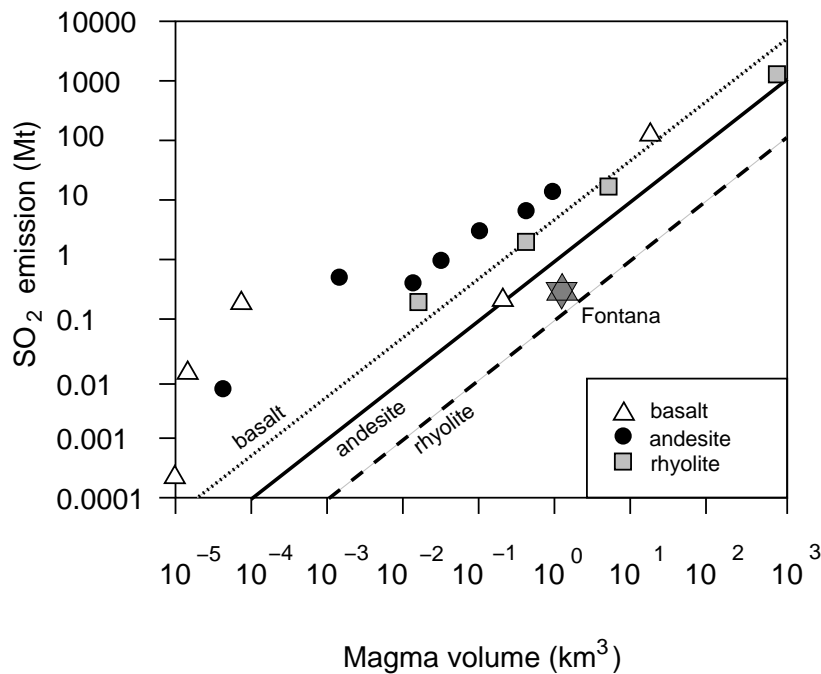


Figure 3.8: Sulphur release of Fontana Tephra (large grey star) compared to a range of other eruptions; total S release is given as SO<sub>2</sub> after Wallace (2001).

Recently, advances have been made to relate the S solubility to magma chamber pressure, temperature, oxygen and sulphur fugacity, proportions of different-valence iron species, amounts of dissolved CO<sub>2</sub> in the melt etc (e.g. Scaillet and Pichavant 2003; Moretti *et al.* 2003). In basaltic, water-poor systems, the predom-

inant form of sulphur is sulphide, occurring under reducing conditions, while rhyolitic, oxidising conditions favor the S speciation as sulphate (Carroll and Webster 1994; Wallace and Carmichael 1992). However, the determination of the solubility of S in silicate melts remains complex because of the presence of the different S species that are likely to coexist (Wallace 2001), and because the importance of the various parameters relative to each other is not yet well understood. Scaillet and Pichavant (2003) point out that the oxygen fugacity exerts only a minor control on the S solubility. However, earlier studies agree on the effect of  $fO_2$  on the Fe partitioning, which is closely linked with the S solubility (e.g. Carroll and Webster 1994; Wallace and Carmichael 1992). For the Fontana melt, no  $CO_2$  concentrations are available, and we could not attempt to calculate the  $Fe^{2+}$ - $Fe^{3+}$  ratio and the  $fO_2$  since appropriate mineral phases are lacking. The absence of Fe-Ti oxides, as well as anhydrite or phyrrothite minerals in the Fontana melt, however, suggest that the oxidation state of the magma was at the transition from reducing to oxidising conditions. This would correspond to a  $\Delta$  NNO value of about -0.5 after Moretti *et al.* (2003), at which the S solubility reaches a minimum, further facilitating a formation of a sulphurous fluid phase in the magma reservoir.

## **3.5 Eruption dynamics**

Explosive magmatic eruptions involve exsolution of volatiles by decompression during magma ascent. Bubbles nucleate and grow, the magmatic foam undergoes dramatic vertical expansion and, when the conditions for fragmentation are reached, disintegrates into the erupted pyroclast-gas-mixture. Intense fragmentation and high exit velocities typical of plinian eruptions are commonly attributed to bubble overpressure developing in highly-viscous melts (e.g. Mader 1998). However, the low-viscous magma of Fontana Tephra also produced a plinian eruption, and it is therefore interesting to analyse how degassing of this magma evolved.

### **3.5.1 Homogeneous versus heterogeneous bubble nucleation**

During homogeneous bubble nucleation, degassing of decompressing magma is retarded until some volatile supersaturation is reached (Navon and Lyakhovsky 1998), when bubbles finally nucleate and grow contemporaneously at similar rates, lead-

ing to good sorting in the bubble size distribution. In contrast, during heterogeneous bubble formation, crystal and microlite surfaces act as nucleation sites for the bubbles and can dramatically decrease the supersaturation required (Navon and Lyakhovsky 1998). Near-equilibrium volatile exsolution then proceeds rather gradually, adapting to the decreasing pressure during magma ascent. Fe-Ti oxides are very efficient as vesicle nucleation sites, whereas feldspars show little or no effect (Navon and Lyakhovsky 1998). Fontana Tephra contains little amounts of microlites, and only few % phenocrysts, mostly plagioclase and no Fe-Ti oxides. This suggests a predominance of homogeneous bubble nucleation during the Fontana magma ascent.

### **3.5.2 Scoria porosity and fragmentation depth**

The fragmentation depth can be constrained from the porosity of the scoria clasts assuming equilibrium degassing (Cervantes and Wallace 2003), hence ignoring the necessity of supersaturation. The vesicularity of the Fontana scoria clasts ranges between 68 and 72 %, averaging at 70 %. Projection of these vesicularity values onto the depth versus porosity curve for ascending basaltic magma with an initial water content of 1.3 wt % and an assumed lithostatic pressure gradient yields shallow fragmentation at 4.5-5.3 MPa pressure (165–195 m depth) for the Fontana eruption (Figure 3.9). This approach assumes that the analysed lapilli did not experience further expansion after fragmentation (Gardner *et al.* 1996).

### **3.5.3 Residual water and fragmentation depth**

Another approach to determine the fragmentation level compares the residual melt water contents with the corresponding saturation pressure calculated for the Fontana magma composition after Moore *et al.* (1998). Again, it is assumed that no further degassing occurred in the analysed lapilli after fragmentation as the lapilli were instantaneously quenched during eruption. Due to some scatter in the thermometric results above, saturation pressures are calculated here for two bracketing temperatures. The residual water contents in the Fontana matrix glass of 0.2-0.5 wt. %, with an average of 0.36 wt. %, correspond to saturation pressures of 0.8-3.8 MPa, with an average of 2.1 MPa at 1075 °C, and to 0.9-4.2 MPa, averaging at 2.2 MPa at 1150 °C (Figure 3.10). Equating pressure at fragmentation with the saturation

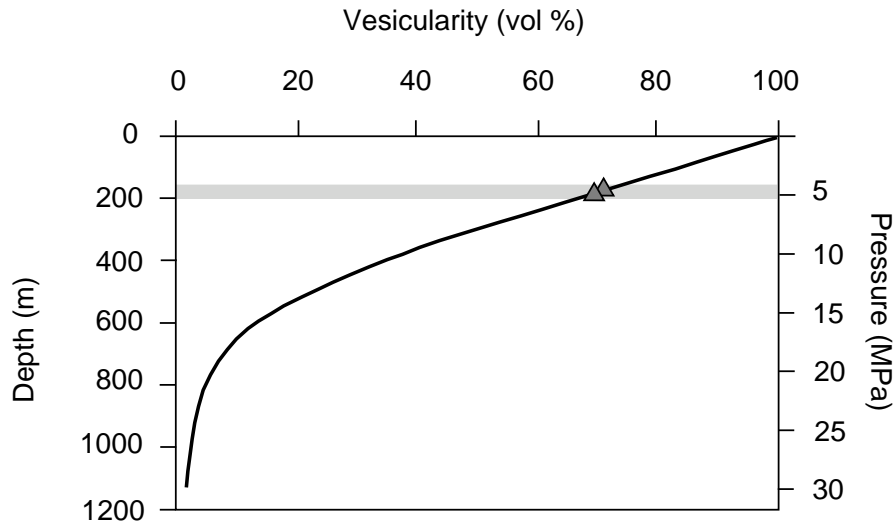


Figure 3.9: Pressure at fragmentation derived from comparing observed average lapilli vesicularities of Fontana Tephra (triangles) with the depth-vesicularity relation of ascending basaltic magma with an initial H<sub>2</sub>O content of 1.3 wt. % and assuming equilibrium degassing under a lithostatic pressure gradient (after Cervantes and Wallace 2003). It is also assumed that magma vesiculation stopped upon fragmentation.

pressure, fragmentation depths ranged between 30 and 150 m but mostly centered around 70–85 m below surface. These variations in pressure at the fragmentation level obtained both from porosity and residual water data may be indicative of fragmentation level fluctuations or variable disequilibrium degassing.

The comparison of the results from both methods in Figure 3.11 shows that the fragmentation depth obtained from the residual water contents is significantly lower than that indicated by the scoria porosity. The vesicularity approach presumes heterogeneous bubble nucleation by which degassing constantly equilibrates with the decreasing pressure. Figure 3.12 illustrates qualitatively how, in comparison, porosity would evolve with pressure in the case of homogeneous bubble nucleation beginning when considerable supersaturation is reached. The initial increase in porosity with decreasing pressure would be steeper due to stronger diffusion. At higher porosities both curves converge yet for a given porosity the pressure would be lower in homogeneous than in heterogeneous nucleation case; the pressure would, in fact,



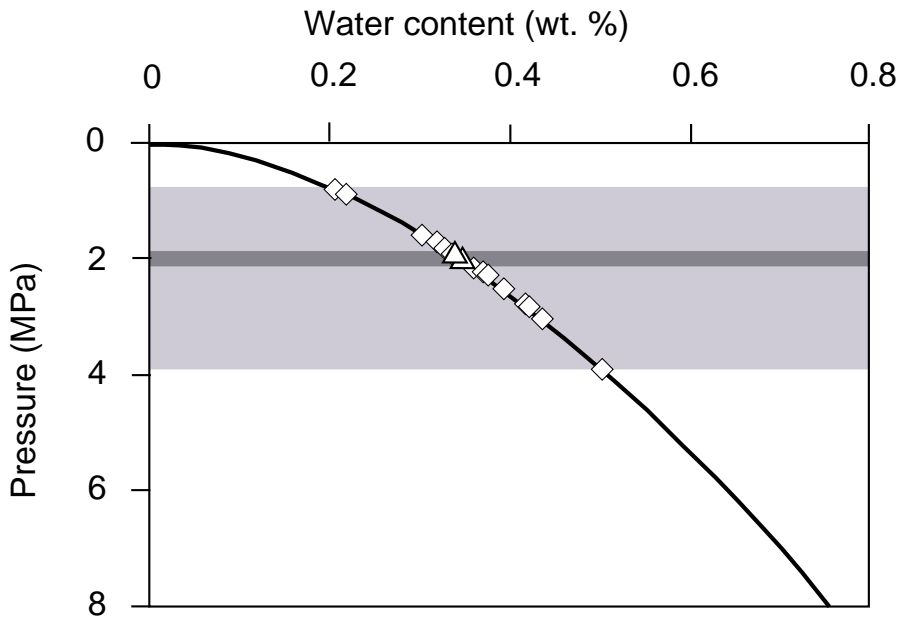


Figure 3.10: Pressure at fragmentation level derived from comparing the residual melt water contents (open diamonds) with the water solubility curve for the Fontana melt calculated after Moore *et al.* (1998). The pale shaded area covers the range in which the fragmentation pressure fluctuated, the dark bar and larger triangles represent the average values.

have the value indicated by the residual water content. The actual supersaturation would be much higher than the c. 2-3 MPa pressure difference observed here at 70 % porosity.

Alternatively, the pressure difference between the two methods could be explained by bubble separation from the melt. If bubbles escaped from their parental batch of low-viscosity melt by buoyancy rise, the remaining foamy batch would have a lower porosity than appropriate for its residual water content. However, efficient gas–melt separation can only occur in slowly rising (<0.5 m/s) basaltic magmas (Wilson and Head 1981; Sparks 2003), whereas the plinian nature of Fontana Tephra implies rather high magma ascent rates.

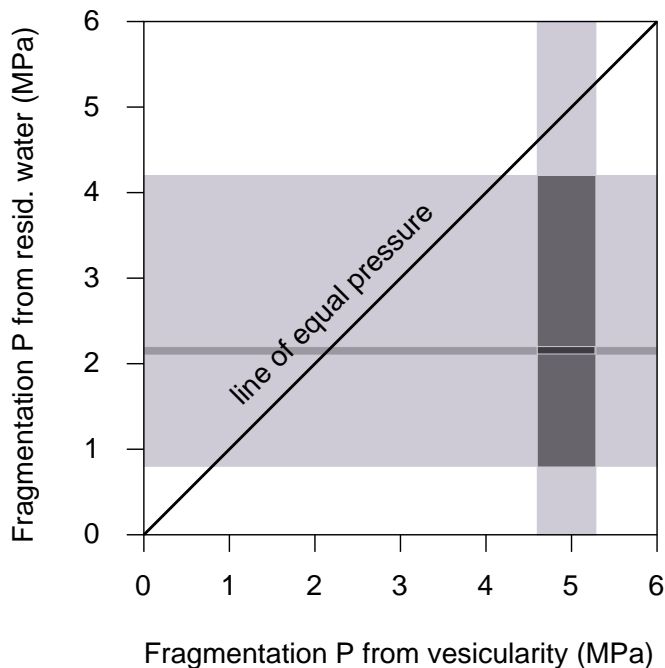


Figure 3.11: Comparison of fragmentation pressure estimates by the two methods in Figure 9 and Figure 10. Pale shaded areas reflect the entire span of pressures, while dark shading gives the average. The overlapping dark grey and black shaded areas show clearly that the scoria vesicularity yields a larger fragmentation pressure than the matrix glass H<sub>2</sub>O contents.

### 3.5.4 Causes of the plinian style of the basaltic-andesitic eruption

The Fontana magma rising from its mid-crustal reservoir (9–15 km depth) had a monotonous basaltic-andesitic composition, a high temperature and low phenocryst content, and hence a low viscosity. Build-up of gas overpressure due to bubble expansion hindered by high viscosity (e.g. Sparks 1978; Barclay *et al.* 1995) cannot be invoked here. An increase of melt viscosity, thus contributing to the magma explosivity, can be caused by intensive precipitation of microlites (e.g. Klug and Cashman 1994). High microlite abundances have been observed e.g. in the magma of the basaltic plinian 1886 AD Tarawera eruption (Sable *et al.* 2003), the Fontana melt, however, did not contain large amounts of microlites. Also, the dissolved water content of c. 1.2 wt.% of the Fontana melt was rather low compared, for ex-

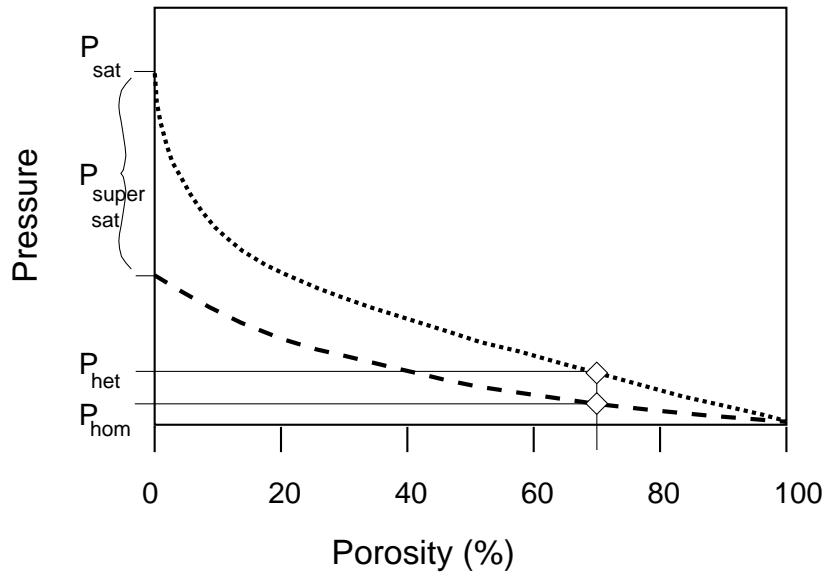


Figure 3.12: Qualitative illustration of vesicularity–pressure relationships during heterogeneous (dotted line) and homogeneous (dashed line) bubble nucleation. Homogeneous bubble nucleation would delay the vesiculation such that a given porosity will be reached at a lower pressure compared to heterogeneous (near-equilibrium) bubble nucleation.

ample, to the explosively erupting basaltic magmas at Fuego volcano in Guatemala, which contained 4-6 wt. %  $H_2O$ . (Sisson and Layne 1993; Roggensack 2001).

We therefore propose that the plinian nature of the Fontana eruption was related to the condition of homogeneous bubble nucleation as derived above. Combining rapid magma ascent and decompression of the magma, facilitated by buoyancy and low viscosity, with the accumulation of substantial supersaturation in the scarcity of heterogeneous bubble nucleation sites implies catastrophic degassing at shallow depth in the conduit (Figure 3.13). This, in turn, would have three effects:

1. large vertical expansion rates of the magma, thereby
2. intense fragmentation, and
3. high exit velocity at the vent.

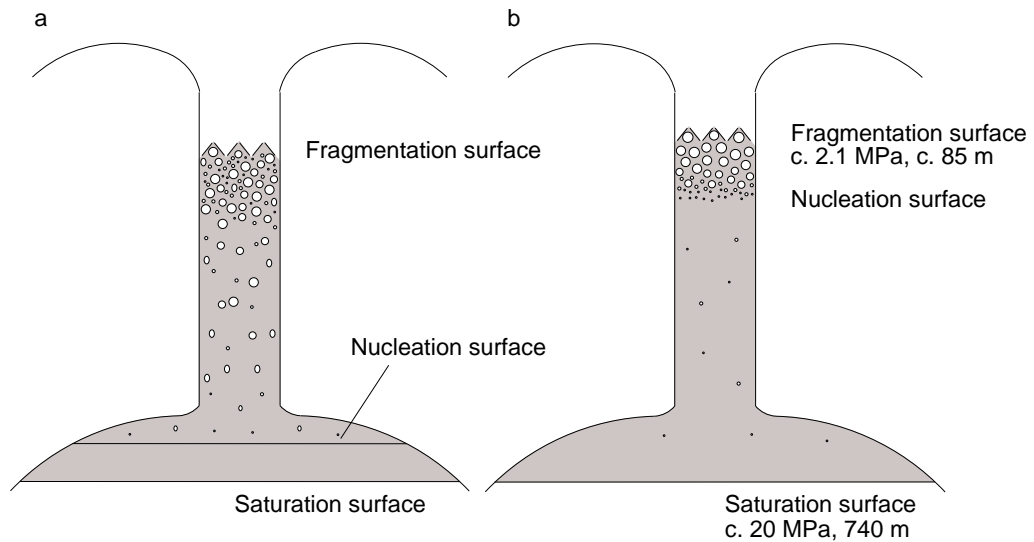


Figure 3.13: Schematic conduit cross-sections of (a) ascending magma characterised by heterogeneous bubble nucleation, at which early bubble formation starts at deep levels and the exsolving volatiles constantly adjust to the pressure regime, and (b) the Fontana magma ascent, dominated by homogeneous bubble nucleation at shallow levels, associated with strong volatile oversaturation and pressure disequilibrium.

High temperature, fine fragmentation and high gas-thrust velocity are the ingredients required to produce high convective eruption columns by which tephra is dispersed at plinian dimensions.

### 3.6 Conclusions

We analysed  $H_2O$ , F, Cl, and S concentrations in melt inclusions in minerals, and matrix glasses of the basaltic-andesitic Fontana Tephra with the aims (1) to quantify the amounts of volatiles released during eruption, (2) to better understand volatile exsolution processes, and (3) to attempt to relate these processes to the unusual eruptive behaviour.

1. During the plinian and subplinian phases of the Fontana eruption, 7 Mt  $H_2O$ ,

30 kt F, 160 kt Cl, and 280 kt S have been released. Gas emission varied non-systematically through the successive eruptive phases, but generally strengthened towards the end of the eruption.

2. F and Cl exsolved in correlation with water by partitioning into the aqueous fluid phase once it became available. We determined partition coefficients,  $D^{f/m}$  of 12-18 for F and 7-30 for Cl from our measured concentrations.
3. Furthermore, we propose a new model to explain the plinian eruptive style of mafic magmas, based on our volatile-chemical and petrographical observations. Post-fragmentation melt water concentrations suggest a fragmentation pressure fluctuating between 0.8 and 4 MPa, corresponding to depths of 30–150 m. Assuming that the scoria vesicularity resulted from equilibrium degassing, higher pressures of 4.5–5.3 MPa at 165–195 m depth are inferred. Delayed, homogeneous bubble nucleation, however, can account for this offset and is supported by the scarcity of microlites in the melt, especially of Fe-Ti oxide microlites, which would have acted efficiently as bubble nucleation sites. The consequence is a large volatile supersaturation, followed by sudden massive bubble formation resulting in rapid acceleration and intense fragmentation of the magma. High temperature, fine grain size, and high eruptive velocity would then favour a buoyant plinian plume. Further constraints to support this scenario may be obtained through detailed measurements of scoria porosities and bubble size distributions.

## Acknowledgements

We are grateful to Adam Kent, Maxim Portnyagin, and Thor Hansteen for providing SIMS reference materials. Ilona Schäpan was of great help during the SIMS analyses, Mario Thöner assisted with the EMA. We thank Keith Putirka for the geothermobarometry software, and Gordon Moore for water solubility modeling software. Muchas gracias tambien al personal del INETER, en Nicaragua, por apoyarnos durante el trabajo de campo. This paper is contribution to the Sonderforschungsbereich 574 at the University of Kiel, Germany.

# Bibliography

- [1] Brasseur, G. (1992): Volcanic aerosols implicated. *Nature* 359, 275–276.
- [2] Bureau, H., Keppler, H., and Metrich, N. (2000): Volcanic degassing of bromine and iodine: Experimental fluid/melt partitioning data and applications to stratospheric chemistry. *Earth and Planetary Science Letters* 183, 51–60.
- [3] Carroll, M.R. and Webster, J.D. (1994): Solubilities of sulfur, noble gases, nitrogen, chlorine, and fluorine in magmas. In: *Volatiles in Magmas* (Carroll, M.R. and Holloway, J.R. (eds.), *Reviews in Mineralogy* 30, 231–279.
- [4] Cervantes, P. and Wallace, P. (2003): Magma degassing and basaltic eruption styles: a case study of ~ 2000 year BP Xitle volcano in central Mexico. *Journal of Volcanology and Geothermal Research* 120, p. 249–270.
- [5] Gardner, J.E., Thomas, R.M.E., Jaupart, C., and Tait, S. (1996): Fragmentation of magma during Plinian volcanic eruptions. *Bulletin of Volcanology* 58, 144–162.
- [6] Gerlach, T.M., Westrich, H.R., and Symonds, R.B. (1996): Preruptive Vapor in Magma of the Climactic Mount Pinatubo Eruption: Source of the Giant Stratospheric Sulfur Dioxide Cloud. In: Newhall, C.G. and Punongbayan, R.S. (eds): *Fire and Mud: Eruptions and Lahars of Mount Pinatubo, Philippines*, Washington University Press, Seattle, WA, 415–433.
- [7] Klug, C. and Cashman, K.V. (1994): Vesiculation of May 18, 1980, Mount St. Helens magma. *Geology* 22, 468–472.
- [8] Mader, H.M. (1998): Conduit flow and fragmentation. In: Gilbert, J.S. and Sparks, R.S.J. (eds): *The physics of explosive volcanic eruptions*. Geological Society, London, Special Publications, 145, 51–71.

- [9] Moore, G., Vennemann, T., and Carmichael, I.S.E. (1998): An empirical model for the solubility of H<sub>2</sub>O in magmas to 3 kilobars. *American Mineralogist* 83, 36–42.
- [10] Moretti, R., Papale, P., and Ottonello, G. (2003): A model for the saturation of C–O–H–S fluids in silicate melts. In: Oppenheimer, C., Pyle, D.M., and Barclay, J. (eds): *Volcanic Degassing*. Geological Society, London, Special Publications, 213, 81–101.
- [11] Navon, O. and Lyakhovskiy, V. (1998): Vesiculation processes in silicic magmas. In: Gilbert, J.S. and Sparks, R.S.J. (eds): *The physics of explosive volcanic eruptions*. Geological Society, London, Special Publications, 145, 27–50.
- [12] Putirka, K., Johnson, M., Kinzler, R., Longhi, J., and Walker, D. (1996): Thermobarometry of mafic igneous rocks based on clinopyroxene-liquid equilibria, 0-30 kb. *Contributions to Mineralogy and Petrology* 123, 92–108.
- [13] Putirka, K., Mikaelian, H., Ryerson, F.J., and Shaw, H. (2003): New clinopyroxene-liquid thermobarometers for mafic, evolved and volatile-bearing lava compositions, with applications to lavas from Tibet and the Snake River Plain, ID. *American Mineralogist* 88, 1542–1554.
- [14] Roggensack, K. (2001): Unraveling the 1974 eruption of Fuego volcano (Guatemala) with small crystals and their melt inclusions. *Geology* 29, 911–914.
- [15] Sable, J.E., Houghton, B.F., Wilson, C.J., and R.J. Carey (2003): Complex proximal geometry of fall deposits from a plinian eruption: implications for eruption dynamics. *AGU Fall Meeting*, San Francisco.
- [16] Scaillet, B. and Pichavant, M. (2003): Experimental constraints on volatile abundances in arc magmas and their implications for degassing processes. In: Oppenheimer, C., Pyle, D.M., and Barclay, J. (eds): *Volcanic Degassing*. Geological Society, London, Special Publications, 213, 23–52.

- [17] Sisson, T.W. and Grove, T.L. (1993a): Experimental investigations of the role of H<sub>2</sub>O in calc-alkaline differentiation and subduction zone magmatism. *Contributions to Mineralogy and Petrology* 113, 143–166.
- [18] Sisson, T.W. and Grove, T.L. (1993b): Temperatures and H<sub>2</sub>O contents of low-MgO high-alumina basalts. *Contributions to Mineralogy and Petrology* 113, 167–184.
- [19] Sisson, T.W. and Layne, G.D. (1993): H<sub>2</sub>O in basalt and basaltic andesite glass inclusions from four subduction-related volcanoes. *Earth and Planetary Science Letters* 117, 619–635.
- [20] Villemant B. and Boudon, G. (1999): H<sub>2</sub>O and halogen (F, Cl, Br) behaviour during shallow magma degassing processes. *Earth and Planetary Science Letters* 168, 271–286.
- [21] Walker, G.P.L., Self, S., and Wilson, L. (1984): Tarawera, 1886, New Zealand - A basaltic Plinian fissure eruption. *Journal of Volcanology and Geothermal Research* 21, 61–78.
- [22] Walker, J.A., Roggensack, K., Patino, L.C., Cameron, B.I., and Matías, O. (2003): The water and trace element contents of melt inclusions across an active subduction zone. *Contributions to Mineralogy and Petrology* 146, 62–77.
- [23] Wallace, P.J. (2001): Volcanic SO<sub>2</sub> emissions and the abundance and distribution of exsolved gas in magma bodies. *Journal of Volcanology and Geothermal Research* 108, 85–106.
- [24] Wallace, P.J. and Carmichael, I.S.E. (1992): Sulfur in basaltic magmas. *Geochimica et Cosmochimica Acta* 56, 1863–1874.
- [25] Webster, J.D., Kinzler, R.J., and Mathez, E.A. (1999): Chloride and water solubility in basalt and andesite melts and implications for magmatic degassing. *Geochimica et Cosmochimica Acta* 63/5, 729–738.
- [26] Wehrmann, H., Bonadonna, C., Freundt, A., Houghton, B.F., and Kutterolf, S. (subm.): Fontana Tephra: a basaltic plinian eruption in Nicaragua. in: Rose, W.I. (ed.): *Volcanic Hazards in Central America*. GSA Special Paper.



[27] Westrich, H.R. and Gerlach, T.M. (1992): Magmatic gas source for the stratospheric SO<sub>2</sub> cloud from the June 15, 1991, eruption of Mount Pinatubo. *Geology* 20, 867–870.

## **Chapter 4**

# **Bromine and iodine concentrations in volcanic glasses determined by Synchrotron-XRF: origin and partitioning of heavy halogens in basaltic-andesitic and rhyolitic arc magma systems**

**Heidi Wehrmann and Armin Freundt**

SFB 574 at IFM-GEOMAR, Wischhofstr. 1-3, 24148 Kiel, Germany

## **Abstract**

Significant amounts of heavy halogens can be cycled through subduction zones as documented by synchrotron-XRF analyses of melt inclusions in two Nicaraguan tephras of rhyolitic and basaltic-andesitic composition. The positive correlation of Br and I concentrations with the Ba-La ratio suggests marine sediments subducted with the downgoing slab to be the dominant source of Br and I, since high Ba/La-value are interpreted as strong slab-sediment signals.

Both heavy halogens partitioned into the magmatic fluid phase before and during eruption. The two large plinian eruptions injected the halogens high into the stratosphere (c. 30 km) where they may have acted as catalysts for ozone depletion.

**Keywords:** Bromine, iodine, sediment recycling, subduction, gas release, explosive eruptions

## 4.1 Introduction

Bromine and iodine concentrations in volcanic glasses provide insights into magmatic processes, material transfer through subduction zones, and possible atmospheric impacts of explosive volcanism.

We have studied volcanic glasses and melt inclusions from two Plinian eruptions in West-Central Nicaragua: the Late-Pleistocene basaltic-andesitic Fontana Tephra, and the c. 12 ka BP rhyolitic Upper Apoyeque Tephra. Fontana Tephra, c.  $1.4 \text{ km}^3$  (1.1 Gt DRE) of scoria, was erupted near Masaya Caldera. Upper Apoyeque Tephra erupted from the Chiltepe Volcanic Complex north of Managua, the total erupted volume is about  $2 \text{ km}^3$  (2 Gt DRE). Here we will quantify the heavy halogen output and discuss origin and partitioning behaviour of Br and I in the evolution of the respective magmas.

Snyder and Fehn (2002) and Snyder *et al.* (2002) analysed volcanic surface waters (i.e. crater lakes, fumaroles, hot springs etc.) for bromine and iodine cycles in subduction systems, to assess inventories of different source reservoirs, as well as element balances in relation to the respective time scales of element cycling through subduction zones. We complement their results derived from quiescent degassing by our results from explosive degassing.

## 4.2 Geologic setting

Chiltepe and Masaya volcanic complexes are part of the Central American Volcanic Arc (CAVA), which results from subduction of the Cocos Plate under the Caribbean Plate. The convergence rate of this subduction zone is about 8.8 cm/year (Kimura *et al.* 1997). At Nicaragua, the slab dip reaches 65 degrees, the steepest along the CAVA.

This subduction system is of erosive rather than accretionary nature, implying significant transport of sediment to depth with the downgoing plate. This subducted sediment component has been inferred by Carr *et al.* (2004) to reach its maximum beneath Nicaragua as reflected by high Ba/La values in volcanic rocks. Also the isotopic compositions of Nicaraguan magmas show peaks of subducted crust and

sediments within the variations along the arc (Hoernle *et al.* 2003). Intense bend-faulting of the downgoing plate offshore Nicaragua may facilitate deep penetration of seawater (Ranero *et al.* 2003). Seawater is a reservoir rich in I, Br, and Cl elements, which may thus be deposited in the subducting plate.

## 4.3 Methods

Techniques to determine bromine and iodine through in-situ spot analyses in volcanic glasses are not yet routine due to concentrations near detection limits and/or lack of suitable reference material. Heavy halogens in geologic samples have previously been analysed by proton-induced X-ray emission (PIXE), a high-resolution microbeam technique, and by instrumental neutron activation analysis (INAA), operating on bulk samples. Few standards are available for in-situ secondary ion mass spectrometry (SIMS) analyses of Br in volcanic glasses, however, no reference material is yet recognised for SIMS-measurements of I.

We analysed Br and I by synchrotron X-ray fluorescence, which is a non-destructive microbeam technique that operates without need of reference materials and enables high-resolution in-situ measurements of heavy halogens in volcanic glasses, crystals, and melt inclusions. This technique has undergone a rapid development and is still subject of continuous improvement; nevertheless, it has advanced to a powerful tool in trace element and volatile analysis of geologic samples during the past two decades (Lechtenberg *et al.* 1996).

### 4.3.1 Synchrotron X-ray fluorescence analyses (SyXRF)

Our analyses were performed at Hasylab/Desy, beamline L in Hamburg, Germany, using white synchrotron light. Photon rays were generated from positrons with energies of 4.6 GeV at a bending magnet with 12.12 m radius; the rays are emitted in a tangential direction into the beam pipe (Hansteen *et al.* 2000). The sample holder was inserted into the synchrotron beam in a 45 degree geometry. The beam diameter measured 12  $\mu\text{m}$ , counting times were set to 1000 s. This setup allows spatially high-resolution measurements and reduces detection limits to 0.2-10 ppm, depending on the atomic weight of the target elements. In homogeneous materials, detection limits for Br and I are < 3 ppm and < 1.1 ppm, respectively, while for com-

pound melt inclusion measurements (see below), they range between 5 and 39 ppm for Br and between 1 and 45 ppm for I. Fe was used as reference element to compute element concentrations by fundamental-parameter approach (Hansteen *et al.* 2000; Lechtenberg *et al.* 1996), presuming a glass density of  $2600 \text{ kg m}^{-3}$  for Fontana Tephra, and  $2350 \text{ kg m}^{-3}$  for Upper Apoyeque Tephra.

For melt inclusion measurements, the signals of inclusion and host crystal were initially counted jointly. Subsequently, the inclusion signal was extracted by comparison to the respective pure host crystal composition. Because the host crystal exerts a shield effect on the secondary radiation emitted from the melt inclusion, this calculation requires to measure the size and the depth of the melt inclusion inside the mineral. These geometric measurements were carried out with an electron microprobe through surface focussing on a backscattered electron image and subsequent determination of the top and the base of the inclusions in transmitted light.

### **4.3.2 Sample preparation**

Only fresh, unaltered pumice and scoria clasts were selected. Measurements were performed on c.  $110 \mu\text{m}$ -thick double-polished wafers of epoxy-embedded scoria, pumice, and melt inclusions in plagioclase and orthopyroxene. The samples were mounted on mylar-clamped sample holders, carefully avoiding any remnants of adhesives within the beam path.

To minimise the analytical error of the melt inclusion measurements, only inclusions larger than the beam diameter were selected. Also, only inclusions with very small ( $< 10 \text{ vol.}\%$ ) or no visible exsolution bubbles were analysed, although such bubbles may have been removed by preparation in some cases.

## **4.4 Data quality and results**

### **4.4.1 Limitations of the analytical method**

The analytical error of the synchrotron XRF-instrument itself is very small,  $< 5 \%$  in glasses, and  $< 10 \%$  in inclusions for elements with an atomic number ( $Z$ )  $> 35$ .

Measurements of homogeneous materials such as matrix glasses and crystals can therefore be considered very accurate. During the course of this study, the same samples were also analysed for Br by Secondary Ion Mass Spectrometry (SIMS). Those analyses produced Br concentrations in the same order of magnitude as the SyXRF measurements, although the SIMS analyses of standards produced scattered concentrations exceeding the typically accepted limits for reproducibility.

SyXRF analyses of inclusions need to be corrected for inclusion volume and depth of inclusion in the host mineral. The analyses thus suffer an additional uncertainty from such geometric measurements. To give an idea on how strongly over- and underestimates of volume or depth would affect the results, Figure 4.1 shows the error obtained from recalculating an analysis while arbitrarily assuming that the inclusions were 5  $\mu\text{m}$  thicker or thinner, or situated at 3 or 10  $\mu\text{m}$  greater or shallower depths in the host crystal than actually measured.

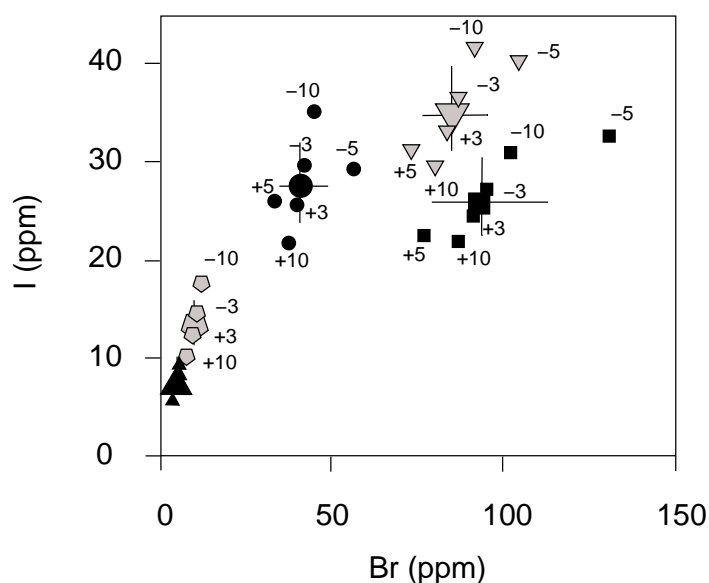


Figure 4.1: Five example analyses recalculated for different geometric dimensions to illustrate their effect on element concentrations: 0=true analysis; -5=inclusions 5  $\mu\text{m}$  smaller, +5=inclusion 5  $\mu\text{m}$  larger, -10=inclusion shifted 10  $\mu\text{m}$  up, -3=inclusion shifted 3  $\mu\text{m}$  up, +3=inclusion shifted 3  $\mu\text{m}$  down, +10=inclusion shifted 10  $\mu\text{m}$  down.

The shield effect of the host crystals is a non-linear function of thickness. It appears to be fairly negligible for 3  $\mu\text{m}$  depth modification, at which the typical error does not exceed 10 %. Projecting the inclusion to 10  $\mu\text{m}$  shallower depth intensifies the analytical signal by up to 25 % for Br; and typically 15–35 % for I, except for one very shallow inclusion that is projected up to the surface; in that case the I-error reaches 60 %. Shifting it to 10  $\mu\text{m}$  greater depths has a smaller effect (maximum 20 % for Br, 15–25 % for I with the one exception of 50 %). However, it is fairly unlikely to misjudge the inclusion depth by more than a few  $\mu\text{m}$ .

The error is related to the true inclusion size: for theoretical inclusion thickness variations, the error increases as the inclusions decrease in size. In large inclusions of more than 25  $\mu\text{m}$  thickness, the error is restricted to typically 10 % with a maximum of 22 % at a very deep-seated inclusion, while the respective error ranges at 15–25 % and may even reach 40 % for the smaller inclusions of 12–18  $\mu\text{m}$ .

In summary, the least sensitivity to geometrical errors is shown by large inclusions that are situated at shallow to moderate depths in the host crystal. However, as not all inclusions comply with such preference, we made an attempt to determine the inclusions' setting inside the crystal as accurately as possible.

#### **4.4.2 Possibility of sample contamination**

Several processes of sample contamination were discussed by Muramatsu and Wedepohl (1998). For example, hydrothermal alteration by percolating iodine-enriched fluids can cause accumulation of I in a rock surface. Moreover, exposure of the rock to coastal atmosphere can lead to wind-induced I-contamination of the sample surface even at medial distances (up to 250 km) from sea. Due to the chemically and geologically similar behaviour of Br and I (Martin *et al.* 1993) and the much higher concentration of Br (67 ppm) than I (52 ppb) in sea water, these processes may potentially lead to contamination with Br. For the two Nicaraguan tephra, this aspect is of minor importance. Central Nicaragua lies in a zone of prevailing easterly winds, and hence the two volcanic centres investigated have an upwind-distance of more than 300 km to the ocean (Caribbean Sea) for most of the time, while the Pacific Ocean, c. 50 km away, is located in a downwind direction.



Another possible source of Br and I are wind-transported plumes from quiescent degassing of active volcanoes nearby, amounts of which are currently investigated by Frische *et al.* (in prep.)

However, most of the Br and I contents of rocks recorded in other studies are by at least three orders of magnitude lower than those of the two Nicaraguan tephras studied here. Hence, the potential contamination by fluids or winds will be less significant, although we cannot rule out cumulative effects. As mentioned above, no possibly contaminated surface parts of the rocks have been included in the analyses.

#### **4.4.3 Br and I abundances**

Concentrations of Br in the Fontana matrix glasses range between 10 and 150 ppm. In most inclusions, Br concentrations were below the detection limits, measurable inclusions have concentrations of 5–18 ppm, one exceptionally high inclusion reached 75 ppm. Fontana matrix glasses display a narrow range of 2 and 8 ppm of I; the inclusions range between 6 and 113 ppm with an average of 32 ppm. For Upper Apoyeque Tephra, matrix glasses scatter between 5 and 300 ppm Br, inclusions contain 13–250 ppm Br. The I contents in the matrix glass are 3–18 ppm, whereas inclusions range from 1–37 ppm with a mean concentration of 20 ppm. Overall, the abundances of bromine and iodine are greater in the rhyolitic Upper Apoyeque Tephra than in the basaltic-andesitic Fontana Tephra.

There is a covariation of Br and I concentrations in the Fontana as well as in the Upper Apoyeque matrix glasses (Figure 4.2b), although the correlation is less well constrained in the latter case. In both tephras, the Br-I ratio increases from the inclusions (1 for Fontana, 3 for Upper Apoyeque) to c. 10–11 in the matrix glass (Figure 4.2 a+b).

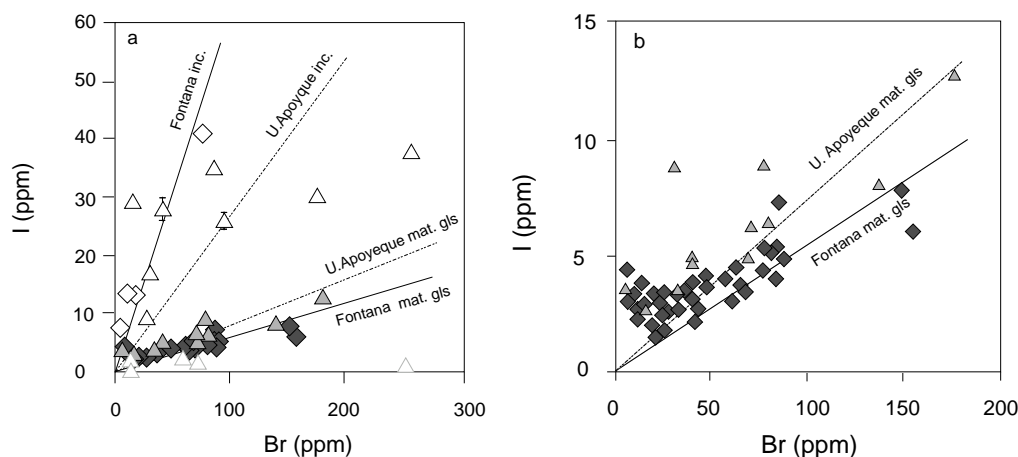


Figure 4.2: Iodine vs. bromine abundances in melt inclusions (open symbols) and matrix glasses (filled symbols) of the basaltic-andesitic Fontana Tephra (diamonds), and the rhyolitic Upper Apoyeque Tephra (triangles). (a) Br-I ratio of about two in the Fontana inclusions, of seven in the Upper Apoyeque inclusions. Of the five inclusions in Upper Apoyeque Tephra that have very low I concentrations, one shows an hourglass structure; the other four inclusions are situated on cleavage planes of their host plagioclase and orthopyroxene crystals, which, in both cases, may have facilitated leakage of volatile elements out of the inclusions. These inclusions have not been considered for the ratio determination. The instrument's analytical error is smaller than the symbols in the illustration; the  $3\mu\text{m}$  depth variation error is exemplarily presented for two inclusions. (b) blown-up section of (a) to illustrate the Br-I linear variation in matrix glasses, showing a constant ratio of about ten (Upper Apoyeque Tephra), and eleven (Fontana Tephra).

## 4.5 Discussion

### 4.5.1 Bromine and iodine exsolution

#### Exsolution mechanisms

Halogens exsolve to variable extent during explosive volcanic eruptions and are released as free gas phases. While Cl is known to exsolve mainly by partitioning into an aqueous fluid phase, little is yet known about Br and I exsolution mechanisms. Halogens in general tend to have high fluid/melt partition coefficients. As determined through laboratory experiments by Bureau *et al.* (2000), the  $D^{f/m}$ -values are

six times higher for I ( $D^{f/m}=104$ ) than for Br ( $D^{f/m}=17.6$ ); while  $D^{f/m}$ -value of Br is about twice that of Cl ( $D^{f/m}=8.1$ ). The  $D^{f/m}$ -value of I during the Fontana eruption is c. 1700, calculated from the data presented here combined with the water release of the Fontana eruption as estimated by Wehrmann *et al.* (in prep.(a)), assuming that I, like Cl, partitioned into the aqueous fluid phase.

Figure 2a and b shows that the decrease in concentration from inclusions to matrix glasses is much larger for I than for Br. This agrees with the strong  $D^{f/m}$ -difference, which implies a larger affinity of I over Br to enter the fluid phase. Moreover, the stronger relative depletion of I over Br from inclusions to matrix glasses in Fontana Tephra compared to Upper Apoyeque Tephra may have two reasons: (1)  $\frac{D_I}{D_{Br}}$  in the basaltic-andesitic Fontana Tephra is larger than in the rhyolitic Upper Apoyeque Tephra; and (2) fractionation of Br in the same range as I may have been limited by less aqueous fluids available in case of Fontana Tephra.

The residual contents of Br and I in the matrix glasses indicate incomplete degassing. The variations in the matrix glass Br and I concentrations may be due to interruption of the gas exsolution process by quenching during eruption, or may be a result of differing diffusion rates of the elements through the melt.

### **Exsolved bromine and iodine masses**

To determine the amount of Br and I released during eruption, we applied the petrologic method. This method is based on the difference of the element abundances between the inclusions and the matrix glasses, considered to represent relatively undegassed and degassed melt, respectively. This difference is then scaled by the total erupted magma mass to obtain the total heavy halogen output. We used mean values of our unambiguous measurement results to estimate the average initial as well as residual heavy halogen contents.

Fontana Tephra ejected a total amount of 1.1 Gt of basaltic-andesitic scoria (Wehrmann *et al.* in prep.(a)), Upper Apoyeque Tephra ranged at 2 Gt total erupted pumice mass (Wehrmann *et al.* in prep.(b)). Combined with the volatile release-percentages, the Fontana eruption emitted 32 kt of iodine, which is about 90% of its initially dissolved I amount. The Upper Apoyeque eruption injected 25 kt of iodine

into the stratosphere, roughly 64 % of the initial I content. Bromine emission during the Upper Apoyeque eruption is 84 kt, making up 33% of the originally dissolved Br. We refrain from attempting to quantify the bromine release of the Fontana eruption because the number of good quality measurement results on the inclusions was not adequate to enable reliable statistics.

### **Possible climate effects**

Eruption columns of large plinian eruptions can extend high into the stratosphere where the volcanically injected heavy halogen gases may behave as major catalysts for destroying ozone, and hence, may substantially contribute to possible climate-relevant processes. Br, in this respect, is known to be about two orders of magnitude more efficient than Cl (Bureau *et al.* 2000). Solomon *et al.* (1994) suggest that the strength of I in ozone destruction may be up to thousand times greater than that of Cl. However, they emphasise that the ozone destruction is probably a coupling effect of I with Br and Cl in a way that I accelerates the photochemical reactions of Br and Cl. Thus, for both Br and I, the ozone-depleting effect can be considerable even at low element abundances (Bureau *et al.* 2000; Solomon *et al.* 1994).

### **4.5.2 Origin of bromine and iodine**

Br and I concentrations measured here are significantly higher than those reported from other igneous rocks, that reach up to 60 ppb of I in bulk rock and glass across a wide range of rock types (Muramatsu and Wedepohl 1998). Up to 6 ppm of Br in rhyolitic bulk rock (Villemant and Boudon 1999), and 1 to 12 ppm of Br in andesite glasses (int. ref. mat. CFA47 and StHs6/80) have been reported. This leads to the question as to the source of the high Br and I concentrations in the Nicaraguan volcanics.

The composition of magmas at subduction zones is controlled by a variety of potential halogen sources: (a) the hydrated subducted crust and mantle, (b) the subducted marine sediments, (c) the mantle wedge, (d) assimilated crust, and (e) possibly fluids in a hydrothermal system.

## **Iodine**

Snyder and Fehn (2002), Snyder *et al.* (2002), and Muramatsu and Wedepohl (1998) emphasise that marine sediments are by far the largest reservoir of iodine in the earth's crust, accumulated through settling of detrital organic material. Concentration in such sediments can reach 3.9 ppm in deep-sea clays to 30 ppm in marine carbonates (Muramatsu and Wedepohl 1998). Déruelle *et al.* (1992), however, present an average of 55 ppm I in marine sediments. These values are by two to three orders of magnitude greater than in seawater (Snyder and Fehn 2002), which usually contains 52 ppb iodine (Déruelle *et al.* 1992). In contrast, the amount of I in the mantle is estimated to be very low, a value of 10 ppb has been presented by McDonough and Sun (1995).

Hydrothermal fluids are often the medium to transport halogens to the surface. These mixtures of water from dehydration of the subducting slab, meteoric waters, and intruded sea water can yield high iodine concentrations. However, also in hydrothermal fluids, I-enrichment has only been reported from sediment hosting systems (Muramatsu and Wedepohl 1998).

Theoretically, I can be mobilised from the mantle wedge. However, to account for the significantly higher iodine concentrations in the resulting magma, selective channeling of large amounts of the element would be necessary. The mantle wedge seems thus to be an unlikely source for the I in the magma (Snyder *et al.* 2002). Déruelle *et al.* (1992) also expressed that the difference between surface reservoirs and mantle is too large to be explained by conventional models of terrestrial differentiation pointing to simple extraction from the mantle. In summary, the earth's sediment shell appears to be the major contributor of iodine to subduction systems (Snyder *et al.* 2002). High I concentration in volcanic rocks is not the signature of an iodine-rich primitive source, but may be indicative of organic matter recycled into the mantle (Déruelle *et al.* 1992).

## **Bromine**

Similarly to I, accumulation of Br in marine sediments has been attributed to decay of organic materials on the ocean floor, marine sediments being strongly Br-enriched compared to terrestrial organic sediments (Martin *et al.* 1993). In the

marine sediments, Martin *et al.* (1993) observed Br concentrations up to 205 ppm. Other potential sources for the Br found in the Fontana and Upper Apoyeque melts show orders of magnitude lower Br abundances and will therefore contribute a minor part to the eruptive Br output: primitive mantle is estimated to contain 50 ppb Br (McDonough and Sun 1995), while the continental crust shows values of 1 ppm Br (Wedepohl 1995).

### **Fractional melting**

As indicated above, the concentrations of Br and I in the mantle are much too low to generate the high Br and I concentrations in the Fontana and Upper Apoyeque melts. Because halogen elements behave incompatibly in most mineral phases, primary melts tend to greatly enrich halogens during partial melting. The concentration of the halogen in the melt,  $C_L$ , in the case of fractional melting is

$$\frac{C_L}{C_0} = \frac{1}{D}(1 - F)^{\frac{1}{D}-1} \quad (4.1)$$

where  $C_0$  is the concentration of the halogen in the original solid,  $D$  is the bulk partition coefficient, and  $F$  describes the melt–fraction.

For a partition coefficient of 0.01 ( $D$ ) and 1 % ( $F$ ) melting of mantle material with 10 ppb I and 50 ppb Br, the resulting melt would reach I concentrations of 370 ppb and Br concentrations of 1.8 ppm. Even if only 0.000001 % of the mantle melted fractionally, the relative enrichment of I would remain below 1 ppm, and that of Br below 5 ppm. Consequently, the mantle alone cannot have been the only parent material of the Fontana and Upper Apoyeque melts. If the heavy halogens are derived from the wedge, the wedge would have to be strongly metasomatised by Br- and I-rich fluids from the slab. Those fluids most likely are derived from subducted sediments.

Figure 4.3 shows a good positive correlation of I and Br with the Ba-La ratio. High Ba-La ratios have been attributed to a strong sediment input into subduction systems. At the Central American Volcanic Arc, several geochemical studies have been carried out to characterise the material input into the subduction zone. These studies show a strong sediment signature peaking in Nicaraguan volcanic rocks, reflected

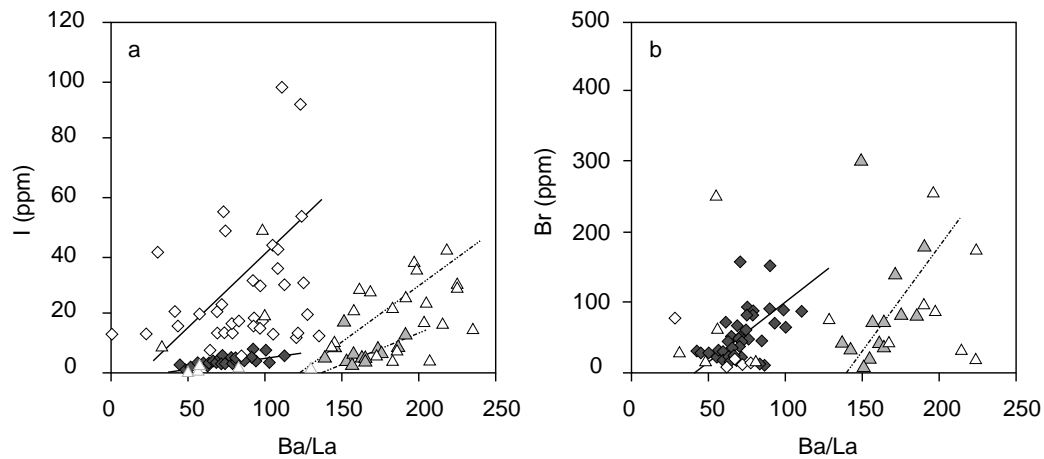


Figure 4.3: (a) I and (b) Br versus Ba-La ratio of Fontana Tephra matrix glasses (filled diamonds), Fontana Tephra inclusions (open diamonds), Upper Apoyeque Tephra matrix glasses (filled triangles), and Upper Apoyeque inclusions (open triangles). The strong positive correlation for each eruption underlines the sediment signature. Differences between I and Br contents of inclusions and matrix glasses represent the fraction degassed upon eruption.

in high Li contents, high Ba-La ratios, low La-Yb ratios, and isotopic composition (e.g. Carr *et al.* 2004; Hoernle *et al.* 2003; Patino *et al.* 2000), which is in line with the results of this study.

## 4.6 Conclusion

SyXRF has proved to be a useful technique to measure heavy halogens in enriched volcanic glasses. Determination of volcanic halogen abundances yields information about the source materials where magma is generated. The Earth's mantle is largely depleted in both Br and I. As the two examples of Central Nicaraguan tephras have shown, high heavy halogen concentrations are related to a substantial input of marine sediments into the subduction zone. On a larger scale, along-arc variations of Br and I contents in volcanic rocks may provide a useful tracer of variations in the sediment-input along subduction zones.

Halogens are transported to the Earth's surface mainly through volcanic activity.

Large-magnitude subaerial plinian eruptions are able to inject halogens high into the stratosphere, where reactive Br and I radicals will act as catalysts for stratospheric ozone destruction. Br is considered to be about hundred times more efficient than Cl. Estimates of the strength of I compared to Cl reach a factor of thousand. Hence, the effect may be substantial even when absolute numbers appear small. In addition, possible interactions between halogen species that intensify the effects cannot be ruled out, and little is yet known about residence times of the elements at the various stratospheric altitudes. The effect of heavy halogens on stratospheric chemistry might still be underestimated, and Br and I should be considered for hazard assessments that include climatic aspects.

### **Acknowledgements**

Credit is due to Thor Hansteen of IfM-Geomar, Kiel, and to Frank Lechtenberg of Hasylab, Hamburg, for technical support with the SyXRF analyses. Hans-Ulrich Schmincke and Steffen Kutterolf made helpful comments on an earlier draft of this manuscript. This publication is contribution # 79 to the Sonderforschungsbereich 574 at Kiel University.



# Bibliography

- [1] Bobrowski, N., Hönninger, G., Galle, B., and Platt, U. (2003): Detection of bromine monoxide in a volcanic plume. *Nature* 423, 273–276.
- [2] Boness, M., Heumann, K.G., and Haack, U. (1991): Cl, Br and I analysis of metamorphic and sedimentary rocks by isotope dilution mass spectrometry. *Contributions to Mineralogy and Petrology* 107, 94–99.
- [3] Bureau, H., Keppler, H., and Metrich, N. (2000): Volcanic degassing of bromine and iodine: Experimental fluid/melt partitioning data and applications to stratospheric chemistry. *Earth and Planetary Science Letters* 183, 51–60.
- [4] Carr, M.J., Feigenson, M.D., Patino, L.C., and Walker, J.A. (2004): Volcanism and geochemistry in Central America: progress and problems. In: Eiler, J. (ed.): *Inside the Subduction Factory*, Geophysical Monograph Series, 138, 324 p.
- [5] Déruelle, B., Dreibus, G., and Jambon, A. (1992): Iodine abundances in oceanic basalts: implications for Earth dynamics. *Earth and Planetary Science Letters* 108, 217–227.
- [6] Frische, M. *et al.* (in prep.): Variations in trace gas emissions from fumaroles of Nicaraguan subduction zone volcanoes: Dynamics of permanently active volcanoes.
- [7] Hansteen, T.H., Sachs, P.M., and Lechtenberg, F. (2000): Synchrotron-XRF microprobe analysis of silicate reference standards using fundamental-parameter quantification. *European Journal of Mineralogy* 12, 25–31.
- [8] Hoernle, K., Sadofsky, S., Nichols, H., Portnyagin, M., Bogaard, P.v.d., and Alvarado, G. (2003): Volatile, trace element and isotopic variations of mafic

arc volcanic rocks from Nicaragua and Costa Rica. *AGU Fall Meeting*, San Francisco.

- [9] Jambon, A., Déruelle, B., Dreibus, G., and Pineau, F. (1995): Chlorine and bromine abundances in MORB: the contrasting behaviour of the Mid-Atlantic Ridge and East Pacific Rise and implications for chlorine geodynamic cycle. *Chemical Geology* 126, 101–117.
- [10] Kimura, G., Silver, E., Blum, P. *et al.* (1997): Proc. ODP, Init. Repts., 170, College Station, TX (Ocean Drilling Program): 458.
- [11] Lechtenberg, F., Garbe, S., Bauch, J., Dingwell, D.B., Freitag, J., Haller, M., Hansteen, T.H., Ippach, P., Knoechel, A., Radtke, M., Romano, C., Sachs, P.M., Schmincke, H.-U., and Ullrich, H.-J. (1996): The X-ray fluorescence measurement place at beamline L of Hasylab. *Journal of Trace Microanalytical techniques* 14, 561–587.
- [12] Martin, J.B., Gieskes, J.M., Torres, M., and Kastner, M. (1993): Bromine and iodine in Peru margin sediments and pore fluids: Implications for fluids origins. *Geochimica et Cosmochimica Acta* 57, 4377–4389.
- [13] McDonough, W.F. and Sun, S.-S. (1995): Composition of the Earth. *Chemical Geology* 120, 223-253.
- [14] Muramatsu, Y. and Wedepohl, K.H. (1998): The distribution of iodine in the earth's crust. *Chemical Geology* 147, 201–216.
- [15] Patino, L.C., Carr, M.J., and Feigson, M.D. (2000): Local and regional variations in Central American arc lavas controlled by variation in subducted sediment input. *Contributions to Mineralogy and Petrology* 138, 265–283.
- [16] Ranero, C.R., Phipps Morgan, J., McIntosh, K., and Reichert, C. (2003): Bending-related faulting and mantle serpentinization at the Middle American trench. *Nature* 425, 367–373.
- [17] Snyder, G.T., Fehn, U., and Goff, F. (2002): Iodine isotope ratios and halide concentrations in fluids of the Satsuma–Iwojima volcano, Japan. *Earth and Planetary Space Science* 54, 265–273.

- [18] Snyder, G.T. and Fehn, U. (2002): Origin of iodine in volcanic fluids:  $^{129}\text{I}$  results from the Central American Volcanic Arc. *Geochimica et Cosmochimica Acta* 66/21, 3827–3838.
- [19] Solomon, S., Garcia, R.R., and Ravishankara, A.R. (1994): On the role of iodine in ozone depletion. *Journal of Geophysical Research* 99D, 20491–20499.
- [20] Villemant, B. and Boudon, G. (1999):  $\text{H}_2\text{O}$  and halogen (F, Cl, Br) behaviour during shallow magma degassing processes. *Earth and Planetary Science Letters* 168, 271–286.
- [21] Webster, J.D., Kinzler, R.J., and Mathez, E.A. (1999): Chloride and water solubility in basalt and andesite melts and implications for magmatic degassing. *Geochimica et Cosmochimica Acta* 63/5, p. 729–738.
- [22] Wedepohl, K.H. (1995): The composition of the continental crust. *Geochimica et Cosmochimica Acta* 59, 1,217-1,239.
- [23] Wehrmann, H., Freundt, A., Kutterolf, S., Wiedenbeck, M., and Schmincke, H.-U. (in prep.(a)): Water, halogen, and sulphur degassing during the basaltic-andesitic plinian eruption of Fontana Tephra, Nicaragua
- [24] Wehrmann, H., Freundt, A., Kutterolf, S., Wiedenbeck, M., and Schmincke, H.-U. (in prep.(b)): Volatile release from the rhyolitic Upper Apoyeque eruption, Nicaragua.

## **Chapter 5**

### **Summary and Conclusion**

Physical and volatile-chemical processes of the Late-Pleistocene Fontana eruption have been investigated during the course of this study. Additionally, aspects of heavy halogen chemistry of the 12 ka BP Upper Apoyeque Tephra were elucidated. Both tephras originated from vents in west-central Nicaragua, part of the erosive Central American subduction zone. In this chapter, the most important findings arising from this study are compiled:

1. Basaltic-andesitic plinian eruptions may evolve through numerous eruptive phases of differing style as evidenced by the Fontana Tephra deposit. The Fontana eruption initiated with a sequence of short, but highly explosive pulses, depositing well-bedded, lithic-free, highly-vesicular fluidal scoria. Subsequently, a surge was released towards the southwest of the vent, while fallout continued in the northwesterly dispersal sectors, emplacing poorly sorted, lithic-rich scoria. This activity was followed by longer-duration plinian episodes forming thick, quasi-massive layers of highly-vesicular scoria with intercalated beds of phreatomagmatically-affected fallout. The eruption terminated through a series of subplinian pulses in which varying amounts of external water were involved, resulting in a stratified succession of highly-vesicular scoria lapilli. These changes in eruptive style are predominantly a result of changing access of external water to the conduit. The repeated interruptions of the quasi-steady fallout behaviour by release of laterally-transported pyroclastic surges, and the subsequent recovering to plinian activity are of great importance for local authorities when managing the hazard and risk emerging from such a volcano to the densely populated areas nearby.
2. The volume of the Fontana eruption is much lower than previously estimated, it ranges between 1.4 and 1.8 km<sup>3</sup>. Column heights during the Fontana eruption reached 24–30 km.
3. Physical eruption models, that were developed for rhyolitic plinian eruptions, have proved to be applicable also to mafic plinian eruptions. This has been derived from the consistency of the results obtained from different models to determine eruption column heights.
4. The plinian style of the Fontana eruption may have been triggered by a delayed homogeneous bubble nucleation in the conduit, which is indicated by a

displacement of the fragmentation level to lower pressure indicated by residual melt water contents, with respect to equilibrium degassing. Further evidence for such process taking place in the Fontana conduit is provided by the scarcity of microlites suitable as bubble nucleation sites, which had prevented bubbles from nucleating in adjustment to the gradually decreasing pressure upon magma ascent.

5. The Fontana eruption released 7 Mt H<sub>2</sub>O, 30 kt F, 160 kt Cl, 280 kt S, and 32 kt I; the Upper Apoyeque eruption emitted 84 kt Br and 25 kt I. Because of the high eruption columns of up to 30 km, these volatiles have been transported high into the stratosphere, where they may have had an impact on climate and atmospheric chemistry. Especially heavy halogens are known to be very efficient in their function as catalysts for destroying stratospheric ozone.
6. Halogen fluid-melt distribution coefficients,  $D^{f/m}$ , calculated from Fontana's melt inclusion and matrix glass halogen and water data, are 12–18 for F, 7–30 for Cl, and 1700 for I.
7. Synchrotron-XRF has proved to be a useful technique to determine concentrations of Br and I in enriched volcanic glasses.
8. Heavy halogen concentration in the basaltic-andesitic Fontana Tephra and the rhyolitic Upper Apoyeque Tephra are unusually high (several tens of ppm), yielding information about the magma source materials: supported by a positive correlation of Br and I with Ba-La ratios, these high heavy halogen abundances prompt to a substantial contamination of the magma by fluids derived from marine sediments at the Nicaraguan segment of the Central American subduction zone. Br and I in volcanic rocks may therefore generally be used as tracers for sediment input into subduction zones, and for possible along-arc variations thereof.



# Appendix



Table A-I: Major element composition (wt. %) of Fontana matrix glasses, determined by electron microprobe analysis (EMA), normalised to 100 % volatile-free; \*original values retained

Unit	SiO2	TiO2	Al2O3	FeO	MnO	MgO	CaO	Na2O	K2O	Cr2O3	P2O5	Total*
D	53.22	1.22	14.74	12.69	0.28	4.21	8.76	2.89	1.73	0.01	0.24	97.17
D	53.15	1.18	14.81	12.86	0.27	4.11	8.15	3.39	1.81	0.00	0.26	96.60
D	52.52	1.40	14.54	13.14	0.21	4.17	8.65	3.37	1.65	0.00	0.35	97.49
D	52.40	1.28	14.86	13.33	0.21	4.21	8.90	2.87	1.58	0.00	0.37	98.53
D	52.59	1.19	14.21	13.64	0.23	4.59	8.76	2.82	1.65	0.03	0.29	97.91
D	53.14	1.12	14.82	12.93	0.25	4.26	8.57	3.00	1.70	0.02	0.19	97.53
D	53.67	1.53	14.98	12.69	0.29	3.88	8.22	2.67	1.68	0.03	0.36	97.30
D	53.08	0.94	14.22	13.81	0.33	4.23	7.93	2.68	2.43	0.07	0.29	97.27
D	52.40	1.17	14.89	13.33	0.31	4.27	8.57	3.02	1.62	0.00	0.39	98.23
D	53.76	1.49	14.97	12.27	0.28	3.81	8.43	2.79	1.89	0.05	0.27	98.09
D	52.91	1.16	14.68	13.42	0.23	4.22	8.50	2.70	1.79	0.00	0.39	96.95
D	53.84	1.10	14.67	12.80	0.29	4.10	8.44	2.72	1.73	0.00	0.31	97.70
D	53.84	1.27	15.02	11.97	0.27	4.04	8.62	2.91	1.73	0.00	0.33	97.35
D	53.58	1.26	14.88	12.41	0.29	3.90	8.64	3.24	1.55	0.00	0.24	97.37
D	53.44	1.33	14.87	12.58	0.33	3.79	8.43	3.29	1.60	0.00	0.34	97.88
D	53.80	1.15	14.72	12.61	0.27	3.90	8.43	3.25	1.66	0.00	0.21	95.94
D	52.71	1.29	14.53	14.97	0.33	3.57	6.69	3.71	1.89	0.03	0.27	97.33
D	53.97	1.23	15.09	12.06	0.25	3.92	8.16	3.16	1.78	0.05	0.33	97.58
D	53.67	1.29	15.07	12.17	0.12	3.88	8.51	3.29	1.63	0.00	0.36	97.58
D	53.70	1.28	14.85	12.46	0.18	3.86	8.46	3.38	1.60	0.00	0.22	96.84
D	53.93	1.18	15.07	11.81	0.23	3.97	8.44	3.42	1.67	0.06	0.23	97.06
E	53.43	1.16	15.67	12.17	0.25	3.94	8.45	3.02	1.45	0.03	0.44	99.82
E	53.51	1.17	15.68	12.06	0.21	3.92	8.51	3.09	1.57	0.02	0.25	99.14
E	54.15	1.12	15.70	11.61	0.16	3.92	8.41	3.09	1.59	0.00	0.24	98.58
E	53.72	1.04	15.40	12.19	0.26	3.84	8.52	3.17	1.55	0.01	0.30	99.64
E	53.31	1.07	15.56	12.35	0.24	3.97	8.50	3.14	1.60	0.00	0.25	99.93
E	53.24	1.13	15.51	12.36	0.24	3.91	8.53	3.18	1.60	0.00	0.29	99.85
E	53.57	1.15	15.56	12.04	0.20	3.95	8.46	3.14	1.60	0.00	0.34	99.25
E	53.81	1.11	15.52	12.06	0.19	3.87	8.49	3.19	1.52	0.00	0.25	99.15
E	53.74	1.18	15.50	11.95	0.16	4.04	8.55	3.04	1.57	0.00	0.27	98.85
E	53.83	0.96	15.42	12.26	0.14	3.92	8.65	3.09	1.58	0.00	0.16	99.07
E	53.70	1.00	15.39	12.33	0.17	3.82	8.48	3.20	1.57	0.03	0.30	98.77
E	53.39	1.04	15.35	12.37	0.20	3.91	8.61	3.18	1.62	0.00	0.33	98.90
E	53.51	1.12	15.50	12.26	0.24	3.87	8.57	3.12	1.64	0.00	0.17	98.77
E	54.20	1.14	15.51	11.97	0.27	3.97	8.46	2.86	1.63	0.00	0.00	98.44
E	53.77	1.17	15.18	12.01	0.18	3.99	8.74	3.03	1.63	0.03	0.26	98.78
E	53.89	1.09	15.31	12.06	0.22	3.86	8.35	3.17	1.63	0.05	0.37	98.46
E	54.18	1.22	15.17	11.85	0.17	3.90	8.34	3.09	1.59	0.11	0.36	99.16
E	53.63	1.21	15.06	12.51	0.14	3.95	8.46	3.00	1.51	0.07	0.44	98.54
E	53.78	1.17	15.10	12.39	0.19	3.88	8.58	3.11	1.50	0.00	0.31	98.12
E	53.65	1.23	15.18	12.24	0.23	3.92	8.47	3.24	1.57	0.03	0.25	98.40
E	53.61	1.17	15.55	12.43	0.24	3.41	8.28	3.48	1.56	0.00	0.27	99.30
E	53.85	0.95	15.00	12.51	0.25	3.99	8.43	3.28	1.60	0.02	0.11	98.06
E	53.24	1.15	15.32	12.62	0.27	4.00	8.44	3.24	1.56	0.02	0.14	98.79
E	53.84	0.95	14.88	12.52	0.28	4.11	8.38	3.15	1.61	0.00	0.27	98.69
E	53.64	1.26	15.17	12.94	0.27	4.00	8.79	1.97	1.59	0.04	0.31	98.33
E	53.59	1.19	14.97	11.99	0.24	3.62	8.89	3.04	2.10	0.00	0.37	97.48
F	53.51	1.48	14.91	12.06	0.26	3.86	8.59	3.34	1.70	0.02	0.27	97.32
F	53.20	1.50	14.71	12.58	0.26	3.99	8.59	3.27	1.49	0.00	0.41	97.59
F	53.54	1.52	14.93	12.09	0.25	3.91	8.39	3.34	1.70	0.00	0.32	97.41
F	53.44	1.31	15.02	12.08	0.23	3.93	8.71	3.39	1.61	0.02	0.26	96.33
F	53.34	1.43	14.74	12.20	0.25	3.80	8.72	3.47	1.80	0.04	0.21	96.72
F	54.39	1.33	17.66	8.47	0.18	3.32	10.00	3.39	1.09	0.00	0.18	97.85
F	54.17	1.20	14.89	12.31	0.22	3.65	8.74	2.59	1.83	0.05	0.34	97.49
F	54.65	1.23	15.50	11.18	0.20	4.01	9.01	2.50	1.45	0.00	0.27	97.59
F	54.73	1.36	15.00	10.79	0.19	3.39	8.46	3.76	1.97	0.00	0.36	95.87
F	53.92	1.34	15.24	11.99	0.21	3.83	8.44	2.94	1.68	0.04	0.36	94.36
F	53.90	1.27	14.92	12.16	0.27	4.05	8.37	3.10	1.56	0.03	0.36	95.07
F	53.05	1.20	14.80	12.38	0.30	3.94	8.73	3.58	1.66	0.00	0.37	94.68
F	53.15	1.39	15.10	12.34	0.26	3.79	8.63	3.39	1.70	0.00	0.25	96.39
F	53.53	1.46	14.82	12.00	0.22	3.94	8.73	3.28	1.72	0.03	0.28	95.40

Table A-I cont.

Unit	SiO2	TiO2	Al2O3	FeO	MnO	MgO	CaO	Na2O	K2O	Cr2O3	P2O5	Total*
F	53.27	1.26	14.66	12.57	0.24	3.98	8.72	3.30	1.63	0.00	0.36	95.66
F	53.56	1.31	14.82	12.42	0.28	3.86	8.39	3.32	1.65	0.00	0.40	99.71
F	53.70	1.38	14.93	12.26	0.17	3.87	8.46	3.30	1.60	0.01	0.33	98.67
F	53.57	1.31	14.89	12.36	0.21	3.91	8.44	3.28	1.70	0.01	0.30	99.40
F	53.39	1.52	14.76	12.53	0.23	3.95	8.27	3.32	1.70	0.00	0.32	99.54
F	53.86	1.28	16.17	11.02	0.14	3.53	8.74	3.54	1.39	0.00	0.34	99.87
G	53.97	1.44	15.77	11.37	0.17	3.54	8.58	3.55	1.24	0.04	0.34	100.39
G	54.04	1.13	15.56	11.59	0.19	3.87	8.56	3.21	1.58	0.02	0.23	100.70
G	54.48	1.26	15.42	11.41	0.25	3.77	8.19	3.36	1.54	0.02	0.29	100.56
G	53.91	1.25	15.82	11.42	0.31	3.77	8.42	3.21	1.62	0.00	0.28	100.15
G	53.58	1.47	15.63	12.21	0.19	3.73	8.19	3.18	1.55	0.00	0.25	100.36
G	53.69	1.29	15.43	11.97	0.22	3.82	8.39	3.15	1.69	0.00	0.35	100.04
G	53.49	1.41	15.45	12.01	0.28	3.92	8.31	3.19	1.58	0.00	0.34	100.22
G	54.11	1.36	15.41	12.06	0.28	3.66	8.22	2.94	1.76	0.00	0.20	99.84
G	55.32	1.15	16.36	9.81	0.18	3.58	8.48	3.39	1.48	0.00	0.25	100.37
G	53.46	1.39	15.44	12.29	0.18	3.91	8.30	3.19	1.54	0.00	0.30	100.30
G	53.88	1.26	14.78	12.68	0.25	4.00	8.26	2.95	1.63	0.01	0.30	98.76
G	53.71	1.35	14.61	12.61	0.18	4.06	8.49	2.99	1.65	0.02	0.32	99.04
G	53.67	1.34	14.82	12.74	0.25	3.97	8.43	2.86	1.56	0.01	0.35	99.62
G	53.63	1.29	15.59	12.33	0.23	3.55	8.31	3.09	1.70	0.00	0.27	100.82
G	54.65	1.17	15.13	12.01	0.20	3.62	7.89	3.16	1.84	0.00	0.33	100.17
G	53.81	1.33	15.43	11.78	0.24	3.37	8.22	3.72	1.78	0.00	0.32	98.82
G	55.06	1.29	16.13	11.43	0.17	3.48	7.70	2.60	1.76	0.00	0.37	99.16
G	54.26	1.82	14.84	13.30	0.25	3.45	7.74	2.42	1.55	0.00	0.37	100.05
G	53.84	1.29	15.44	11.19	0.24	4.66	9.28	2.85	0.92	0.00	0.29	100.51
G	54.23	1.61	14.64	14.52	0.26	3.42	6.83	2.03	2.04	0.02	0.41	100.53
G	54.42	1.42	15.45	11.27	0.14	3.16	8.28	3.96	1.55	0.08	0.28	99.87
G	53.66	1.38	15.23	12.81	0.26	3.88	8.18	2.73	1.60	0.00	0.26	98.80
G	53.69	1.34	15.46	12.27	0.24	3.87	8.40	2.83	1.65	0.00	0.24	98.39
G	53.97	1.40	15.21	12.16	0.24	3.78	7.97	3.27	1.64	0.00	0.35	98.75
G	54.02	1.17	15.37	12.09	0.27	3.83	7.89	3.45	1.66	0.00	0.25	98.05
G	53.30	1.40	14.94	14.63	0.29	3.91	7.86	1.80	1.58	0.00	0.30	97.99
G	52.95	1.33	15.09	12.06	0.12	3.49	7.32	4.94	2.27	0.00	0.42	98.42
G	53.40	1.43	15.41	12.29	0.24	3.93	8.49	2.77	1.75	0.00	0.30	97.75
G	53.24	1.20	14.55	12.84	0.25	4.07	8.72	3.10	1.65	0.06	0.32	98.02
G	52.87	1.38	14.91	12.98	0.21	4.04	8.41	3.17	1.60	0.05	0.38	98.72

Table A-II: Major element composition (wt. %) of Fontana melt inclusions, determined by EMA, normalised to 100 % volatile-free; \* original values retained

Unit	SiO2	TiO2	Al2O3	FeO	MnO	MgO	CaO	Na2O	K2O	Cr2O3	P2O5	Total*
D	54.77	1.21	14.43	12.95	0.22	3.99	8.07	2.01	1.94	0.00	0.40	94.88
D	53.99	1.32	13.93	13.09	0.35	4.62	7.79	2.51	2.16	0.00	0.24	96.63
D	53.82	0.97	14.83	12.26	0.27	4.34	8.14	3.24	1.89	0.00	0.22	96.83
D	53.38	1.30	14.55	13.06	0.29	4.33	8.39	2.71	1.68	0.00	0.33	96.83
D	53.58	1.18	15.12	12.32	0.27	4.17	8.51	2.95	1.62	0.01	0.26	96.25
D	55.48	1.19	13.89	13.50	0.21	4.37	7.56	1.78	1.77	0.00	0.25	92.90
D	53.17	1.56	12.04	15.02	0.21	4.77	8.01	2.77	2.01	0.05	0.38	96.80
D	53.87	1.41	12.32	14.07	0.31	5.02	7.50	2.83	2.29	0.06	0.34	95.09
E	54.56	0.98	14.56	11.91	0.25	4.53	7.98	3.18	1.77	0.00	0.28	97.12
E	52.80	0.83	18.26	10.23	0.22	3.62	9.92	2.71	1.22	0.02	0.18	98.67
E	54.43	0.98	14.58	12.15	0.22	4.53	7.86	3.12	1.84	0.00	0.29	97.17
E	52.95	0.91	14.15	13.87	0.23	4.83	8.18	2.90	1.72	0.00	0.27	97.44
E	52.58	1.08	14.34	13.51	0.33	4.87	8.40	2.91	1.73	0.00	0.24	96.82
E	53.83	1.10	14.97	12.05	0.28	4.42	8.39	3.11	1.61	0.00	0.24	97.29
E	54.32	1.00	13.63	12.84	0.25	4.69	7.62	2.95	2.34	0.00	0.36	92.13
E	55.43	1.21	14.01	12.62	0.21	4.69	8.01	1.68	1.79	0.04	0.33	94.62
E	53.58	1.07	14.25	13.39	0.25	4.51	8.21	2.50	1.87	0.00	0.36	97.12
E	53.63	1.03	14.57	12.81	0.23	4.57	8.37	2.51	1.95	0.00	0.32	96.52
E	55.43	1.14	13.44	12.53	0.23	4.62	7.75	2.51	2.13	0.00	0.22	96.42
E	54.07	1.52	12.51	13.81	0.27	5.03	7.67	2.74	2.10	0.00	0.27	95.97
E	53.91	1.23	14.81	12.20	0.18	4.34	8.14	3.00	1.90	0.00	0.29	96.58
E	53.49	1.40	14.59	12.67	0.24	4.31	7.97	3.07	1.84	0.02	0.40	97.19
F	53.56	1.44	14.36	12.98	0.27	4.27	7.96	2.68	2.11	0.00	0.37	95.59
F	52.45	1.74	11.91	14.83	0.28	5.50	8.86	2.57	1.46	0.03	0.36	94.75
F	55.15	1.18	13.52	11.79	0.24	4.41	8.44	3.26	1.70	0.06	0.25	95.42
F	53.69	1.16	15.02	11.60	0.20	4.48	8.43	3.32	1.72	0.01	0.36	94.99
F	53.11	1.36	15.50	12.94	0.23	4.02	8.08	2.98	1.47	0.00	0.29	95.37
F	53.70	1.33	15.31	12.98	0.20	4.16	7.98	2.60	1.47	0.00	0.27	94.94
F	53.20	1.27	14.59	12.63	0.22	4.23	8.78	3.20	1.64	0.00	0.23	94.48
G	53.57	1.33	15.62	11.65	0.18	4.38	8.39	2.99	1.62	0.03	0.24	98.56
G	53.81	1.30	13.36	13.31	0.19	5.20	7.69	2.84	1.89	0.07	0.33	98.11
G	53.46	1.41	15.19	11.98	0.10	4.63	8.34	2.76	1.82	0.07	0.23	98.30
G	53.65	1.29	14.59	12.50	0.23	4.70	7.86	2.84	2.08	0.00	0.26	98.50
G	55.08	1.00	15.09	11.81	0.21	4.05	7.81	3.02	1.75	0.01	0.17	98.79
G	51.41	1.29	17.67	11.77	0.20	3.80	9.56	2.89	1.16	0.02	0.23	100.42
G	55.13	1.43	12.48	14.17	0.26	5.01	7.15	2.08	1.95	0.00	0.33	96.53
G	54.35	1.35	13.29	13.52	0.22	4.88	7.33	2.75	2.05	0.00	0.24	98.47
G	54.64	1.21	14.04	12.45	0.28	4.58	7.66	2.71	2.04	0.03	0.36	97.91
G	53.75	1.50	14.32	13.07	0.32	4.78	7.47	2.45	1.95	0.00	0.39	98.19
G	54.05	1.32	14.68	12.81	0.23	4.47	7.93	2.46	1.79	0.01	0.24	97.68
G	51.82	0.96	19.03	10.28	0.17	3.20	9.76	3.95	0.66	0.00	0.16	100.52
G	53.58	1.21	14.97	12.81	0.30	4.30	7.65	2.89	2.02	0.00	0.27	97.50
G	53.86	1.36	15.31	12.10	0.20	4.02	7.95	3.06	1.79	0.00	0.35	97.94

Table A-III: Volatile element concentrations (ppm) in Fontana matrix glasses, determined by EMA

Unit	S	Cl	Unit	S	Cl
D	50	1000	F	60	1060
D	340	880	F	30	1030
D	280	950	F	80	890
D	310	830	F	30	1100
D	260	850	F	120	1100
D	320	940	F	420	1250
D	170	1040	F	250	1270
D	190	930	F	0	1050
D	150	1050	F	20	1110
D	280	1030	F	60	1090
D	250	990	F	0	1160
D	60	1170	F	420	1340
D	130	910	F	290	1330
D	70	690	F	30	960
D	250	1190	F	50	1140
D	330	1080	F	30	1130
D	340	940	F	40	1160
D	90	1250	F	290	1400
D	140	760	F	320	1110
D	170	810	F	220	1160
D	80	860	F	140	890
D	100	930	F	180	820
E	120	910	F	180	1170
E	100	900	F	380	1220
E	90	1020	F	120	1040
E	90	940	F	70	1060
E	110	830	F	230	980
E	90	790	F	110	1090
E	40	910	G	70	1200
E	20	860	G	50	1140
E	120	870	G	70	1360
E	160	1050	G	70	960
E	90	880	G	30	1090
E	140	930	G	40	1090
E	150	800	G	170	1050
E	160	860	G	100	970
E	40	980	G	60	880
E	90	770	G	60	940
E	150	730	G	110	970
E	90	900	G	110	970
E	190	1010	G	60	970
E	30	1110	G	40	900
E	110	940	G	20	1250
E	160	1140	G	30	1110
E	200	1220	G	80	1200
E	190	1270	G	120	1210
E	90	1080	G	220	1280
E	140	1150	G	170	1230
F	110	880	G	180	1310
F	110	940	G	200	880
F	160	1010	G	20	980
F	40	1060	G	140	1220
F	210	1030	G	100	870
F	150	900	G	10	1110
F	160	1260	G	80	1090
F	180	1010	G	50	1010
F	160	1130	G	390	1190

Table A-IV: Volatile element concentrations (ppm) in Fontana melt inclusions, determined by EMA

Unit	S	Cl
D	270	1220
D	390	1080
D	350	1040
D	320	1050
D	430	1070
D	360	1060
D	380	1330
D	430	1130
E	420	1050
E	420	1170
E	430	1180
E	570	1250
E	580	1180
E	440	1060
E	410	1200
E	390	1190
E	370	1070
E	450	1200
F	300	1330
F	460	1080
F	400	990
F	360	1190
F	380	1270
F	510	1230
F	410	1110
F	260	1300
F	390	1080
F	500	1450
F	350	1070
F	360	1220
F	350	1080
F	390	1230
F	560	1370
F	400	1020
F	340	1180
G	380	1240
G	230	1230
G	370	1140
G	350	1160
G	400	1190
G	460	1340
G	350	920
G	320	1050
G	270	1240
G	320	1210
G	410	1280
G	310	1150
G	280	440
G	440	1400

Table A-V: Bulk major element composition (wt. %) of Fontana, determined by X-ray fluorescence (XRF), normalised to 100 % volatile-free; \* original values retained

Unit	SiO2	TiO2	AL2O3	Fe2O3	MnO	MgO	CaO	Na2O	K2O	P2O5	Total*
D	52.57	1.26	15.09	13.25	0.22	4.00	8.29	3.14	1.56	0.34	99.46
F	52.40	1.24	15.37	13.16	0.22	4.03	8.49	2.99	1.49	0.34	99.04
G	52.31	1.23	15.30	13.20	0.22	4.06	8.52	3.06	1.50	0.34	99.49
G	52.29	1.23	15.39	13.21	0.22	4.09	8.56	2.93	1.46	0.34	99.17

Table A-VI: Bulk trace element concentrations (ppm) of Fontana, determined by XRF

Unit	Co	Cr	Ni	V	Zn	Ce	La	Nb	Ga	Pb	Pr
D	40	20	12	394	119	28	<14	8	18	14	<4
F	40	20	11	389	119	21	<14	10	21	14	5
G	41	27	32	388	120	25	<14	8	15	11	<4
G	37	25	23	396	120	31	<14	7	16	8	<4

Table A-VI cont.

Unit	Rb	Ba	Sr	Th	Y	Zr
D	31	1078	395	<4	31	128
F	30	1071	397	<4	31	121
G	32	1008	401	<4	30	127
G	30	1015	403	<4	32	121

Table A-VII: Volatile element concentrations (H2O in wt. %; F, Cl, S, in ppm) of Fontana matrix glasses, determined by secondary ion mass spectrometry (SIMS)

Unit	H2O	F	Cl	S
D	0.39	388	1324	81
D	0.33	366	1225	155
D	0.31	215	1155	63
D	0.36	358	826	56
D	0.42	511	1176	60
mean	0.36	368	1141	83
stdev	0.05	105	188	42
E	0.42	306	1096	110
E	0.35	317	886	64
E	0.35	340	1064	163
E	0.32	316	1064	67
mean	0.36	320	1028	101
stdev	0.04	14	96	46
F	0.22	396	1433	122
F	0.37	354	1145	75
F	0.21	358	1334	54
F	0.51	350	1093	96
F	0.42	358	1065	79
mean	0.34	363	1214	85
stdev	0.13	19	161	25
G	0.44	376	1544	37
G	0.37	382	910	44
G	0.30	416	982	28
mean	0.37	391	1146	36
stdev	0.07	22	347	8

Table A-VIII: Volatile element concentrations (H2O in wt. %; F, Cl, S in ppm) of Fontana melt inclusions, determined by SIMS

Unit	H2O	F	Cl	S
D	1.04	405	929	319
D	1.49	464	1283	394
D	0.40	107	819	101
D	1.24	436	1580	408
D	0.93	330	1354	376
D	0.98	308	1335	335
D	0.92	337	1310	378
D	1.02	318	939	360
mean	1.00	338	1194	334
stdev	0.31	110	265	99
E	1.03	346	1164	255
E	1.10	339	1109	259
E	1.02	336	1319	374
E	1.03	339	1314	343
E	1.10	340	1205	376
E	0.95	361	1026	333
E	0.95	361	963	251
mean	1.03	346	1157	313
stdev	0.06	11	136	56
F	0.87	296	1168	257
F	1.13	451	1385	423
F	1.16	498	1803	490
F	1.04	433	1278	352
F	0.95	430	1593	360
F	1.85	401	1014	274
mean	1.17	418	1374	359
stdev	0.35	68	288	88
G	1.49	479	1670	348
G	0.83	382	1435	341
G	0.87	414	1381	474
G	1.27	488	1130	354
mean	1.12	441	1404	379
stdev	0.32	51	222	64



Table A-IX: Volatile element concentrations (ppm) of Fontana matrix glasses, determined by synchrotron-XRF (SyXRF)

Unit	Br	Br error	I	I error	Ba/La
A	43.0	0.8	2.8	0.2	77.9
A	6.9	0.6	4.4	0.2	85.9
A	9.7	0.7	3.4	0.2	83.9
A	7.7	0.9	3.5	0.3	87.6
A	18.3	0.6	3.0	0.2	57.4
A	21.5	0.6	3.0	0.2	55.9
A	28.3	0.7	2.6	0.2	58.7
A	32.1	0.7	3.2	0.2	67.9
A	78.8	1.1	5.3	0.3	79.7
A	84.5	1.1	5.2	0.3	78.4
A	64.1	1.0	4.5	0.3	70.2
A	87.8	1.3	4.9	0.3	91.2
D	22.2	0.7	2.8	0.2	56.6
D	7.9	0.8	3.2	0.3	64.4
D	14.8	0.8	3.8	0.3	69.6
D	21.1	0.7	2.6	0.2	61.7
D	14.5	0.7	3.0	0.2	60.2
D	21.7	0.7	2.9	0.2	68.0
D	20.2	0.6	2.2	0.2	57.4
D	25.4	0.7	2.4	0.2	64.8
D	84.8	1.2	5.4	0.3	112.3
D	84.9	1.2	4.0	0.3	81.9
D	12.1	0.6	2.3	0.2	70.4
E	26.3	0.7	2.4	0.2	44.2
E	21.0	0.6	3.0	0.2	56.8
E	57.6	0.9	4.0	0.2	76.0
E	149.5	1.7	7.8	0.4	91.9
E	20.8	0.7	3.3	0.2	57.2
E	89.1	1.1	4.9	0.3	76.8
E	14.5	0.7	3.2	0.2	74.0
E	18.1	0.7	3.3	0.2	60.7
E	47.8	0.8	4.1	0.2	67.0
E	41.0	0.7	3.2	0.2	64.9
E	20.5	0.7	3.1	0.2	57.4
F	66.5	1.0	3.7	0.3	94.2
F	14.5	0.7	3.2	0.2	69.7
F	12.0	0.7	2.7	0.3	69.3
F	18.9	0.7	2.6	0.2	73.9
F	22.4	0.6	1.6	0.1	52.5
F	43.0	0.7	2.2	0.2	77.9
F	42.3	0.8	2.4	0.2	73.5
F	37.9	0.8	3.5	0.2	73.0
F	48.0	0.8	3.7	0.2	72.0
F	19.4	0.7	2.1	0.2	61.8
F	85.6	1.1	7.2	0.4	100.3
F	42.9	0.8	2.9	0.2	72.6
F	77.7	1.1	4.4	0.3	76.7
F	14.3	0.7	3.0	0.2	66.5
F	33.2	0.7	2.7	0.2	70.8
F	25.8	0.6	1.8	0.1	46.9
F	41.9	0.8	3.8	0.2	86.3
G	19.5	0.7	2.8	0.2	71.3
G	21.9	0.7	2.6	0.2	58.5
G	20.9	0.6	2.2	0.2	64.5
G	20.3	0.6	2.2	0.2	60.7
G	26.3	0.7	3.3	0.2	60.8
G	68.4	0.9	3.4	0.2	63.0
G	61.5	1.1	3.1	0.3	101.9
G	155.8	1.9	6.0	0.4	72.6
G	24.5	0.6	1.7	0.2	51.6

Table A-X: Volatile element concentrations (ppm) of Upper Apoyeque matrix glasses, determined by SyXRF

Unit	Br	Br error	I	I error	Ba/La
lower	5.3	0.2	3.7	0.2	152.3
lower	69.3	0.3	5.0	0.1	164.4
lower	177.9	0.0	12.8	0.0	190.5
lower	137.9	0.5	8.2	0.1	172.5
upper	31.3	0.7	8.9	0.4	144.0
upper	78.1	0.9	8.9	0.4	186.0
upper	39.4	0.5	4.9	0.2	162.3
upper	302.2	0.0	17.5	0.0	150.2
upper	80.6	0.3	6.5	0.1	175.8
upper	41.1	0.5	5.0	0.2	138.4
upper	71.2	0.3	6.4	0.1	157.2
upper	16.6	0.3	2.8	0.1	155.8
upper	33.6	0.4	3.6	0.2	165.0

Table A-XI: Volatile element concentrations (ppm) of Fontana melt inclusions, determined by SyXRF

Unit	Br	Br error	I	I error	Ba/La
A	-	-	11.8	0.8	120.1
A	-	-	12.8	0.9	105.5
A	-	-	12.3	0.9	134.4
D	-	-	91.7	7.0	122.5
D	-	-	41.8	3.5	107.8
D	-	-	80.1	4.6	-
D	-	-	112.9	8.0	-
D	-	-	97.8	7.1	110.9
D	-	-	19.9	1.3	57.8
D	-	-	54.7	3.7	73.0
E	-	-	30.0	2.3	112.8
E	-	-	15.9	1.1	93.4
E	-	-	18.5	1.1	93.0
E	-	-	17.7	1.1	82.5
E	75.2	3.8	41.1	2.2	31.0
E	-	-	12.9	0.9	0.8
E	-	-	30.7	2.0	124.5
E	-	-	35.5	2.6	107.9
E	-	-	48.3	3.0	74.8
E	-	-	44.2	2.4	-
E	-	-	16.4	1.2	78.7
E	-	-	15.7	0.9	44.0
E	-	-	13.4	0.8	121.2
E	-	-	5.6	0.4	84.6
E	-	-	21.0	1.2	68.9
E	-	-	44.1	2.5	-
F	-	-	29.4	2.2	96.2
F	-	-	14.8	1.2	96.9
F	-	-	19.5	1.6	127.4
G	17.7	1.5	13.2	0.9	68.4
G	11.2	1.4	13.3	0.9	79.2
G	-	-	36.9	2.4	-
G	10.1	1.4	13.4	0.9	73.8
G	5.0	0.9	7.6	0.5	63.8
G	-	-	17.3	1.2	97.2
G	-	-	43.2	3.0	105.5
G	-	-	53.4	3.5	123.3
G	-	-	48.4	3.7	-
G	-	-	13.0	1.0	22.9
G	-	-	22.9	2.0	71.9
G	-	-	20.7	1.5	42.2
G	-	-	31.3	2.5	92.2

Table A-XII: Volatile element concentrations (ppm) of Upper Apoyeque melt inclusions, determined by SyXRF

Unit	Br	Br-Err	I	I-Err	Ba/La
lower	-	-	17.3	0.7	202.5
lower	-	-	14.8	0.9	234.3
lower	-	-	7.3	0.3	184.7
lower	-	-	5.7	0.3	171.5
lower	-	-	4.4	0.3	206.6
lower	-	-	3.5	0.2	182.1
lower	-	-	28.8	2.1	161.2
lower	41.0	5.2	27.6	2.2	168.3
lower	85.2	5.1	34.9	2.3	197.7
lower	-	-	42.0	3.5	217.5
lower	27.6	1.0	9.0	0.2	33.5
middle	15.6	0.9	29.1	0.5	224.2
middle	12.9	1.1	2.0	0.1	82.7
middle	249.6	4.2	0.6	0.1	56.6
middle	59.2	1.3	2.1	0.2	57.6
middle	-	-	22.0	0.5	182.1
middle	-	-	19.4	0.4	99.4
middle	-	-	8.6	0.7	142.7
middle	-	-	10.0	0.7	144.9
middle	-	-	24.2	1.4	203.1
middle	173.3	6.8	29.9	2.1	224.3
upper	13.1	1.5	0.0	0.0	50.4
upper	72.0	0.9	1.2	0.1	129.4
upper	93.6	3.6	25.8	1.6	190.5
upper	254.5	6.2	37.8	2.4	196.0
upper	29.5	2.6	16.7	1.3	214.6
upper	-	-	21.2	1.7	156.7

Table A-XIII: Variations in concentrations (ppm) for different geometric dimensions of selected melt inclusions, determined by SyXRF

	Inc depth- Thickness	Br	Br error	% of true value	I	I error	% of true value
Fontana							
true value	68-27	-	-	-	18.5	1.1	100
3 deeper	68-27	-	-	-	17.8	1.1	96
3 shallower	68-27	-	-	-	19.3	1.2	104
10 deeper	68-27	-	-	-	16.4	1.0	89
10 shallower	68-27	-	-	-	21.5	1.3	116
5 thicker	68-27	-	-	-	16.3	1.0	88
5 thinner	68-27	-	-	-	21.4	1.3	116
true value	20-29	10.1	1.4	100	13.4	0.9	100
3 deeper	20-29	9.5	1.4	94	12.4	0.9	92
3 shallower	20-29	10.8	1.5	107	14.6	1.0	109
10 deeper	20-29	8.2	1.2	82	10.3	0.7	77
10 shallower	20-29	12.6	1.8	125	17.8	1.2	132
5 thicker	20-29	9.5	1.4	94	12.3	0.9	92
5 thinner	20-29	10.9	1.6	107	14.7	1.0	110
true value	34-26	5.0	0.9	100	7.6	0.5	100
3 deeper	34-26	4.7	0.8	95	7.1	0.5	93
3 shallower	34-26	5.2	0.9	106	8.2	0.5	107
10 deeper	34-26	4.2	0.7	85	6.1	0.4	80
10 shallower	34-26	6.0	1.0	121	9.7	0.6	128
5 thicker	34-26	4.6	0.8	93	6.9	0.4	91
5 thinner	34-26	5.4	0.9	110	8.5	0.6	112
true value	16-49	-	-	-	13.4	0.8	100
3 deeper	16-49	-	-	-	12.3	0.8	92
3 shallower	16-49	-	-	-	14.7	0.9	109
10 deeper	16-49	-	-	-	10.1	0.6	75
10 shallower	16-49	-	-	-	18.1	1.1	135
5 thicker	16-49	-	-	-	12.6	0.8	94
5 thinner	16-49	-	-	-	14.3	0.9	107
Apogee							
true value	56-29	-	-	-	5.7	0.3	100
3 deeper	56-29	-	-	-	5.2	0.3	92
3 shallower	56-29	-	-	-	6.1	0.3	109
10 deeper	56-29	-	-	-	4.3	0.2	76
10 shallower	56-29	-	-	-	7.4	0.4	132
5 thicker	56-29	-	-	-	5.8	0.3	103
5 thinner	56-29	-	-	-	5.3	0.3	94
true value	14-12	41.0	5.2	-	27.6	2.2	100
3 deeper	14-12	40.0	5.1	98	25.7	2.1	93
3 shallower	14-12	42.1	5.3	103	29.6	2.4	107
10 deeper	14-12	38.1	4.8	93	21.8	1.7	79
10 shallower	14-12	45.0	5.7	110	35.1	2.8	127
5 thicker	14-12	34.0	4.3	83	26.0	2.1	94
5 thinner	14-12	56.8	7.2	138	29.4	2.4	106
true value	9-27	-	-	-	4.4	0.3	100
3 deeper	9-27	-	-	-	3.6	0.2	82
3 shallower	9-27	-	-	-	5.2	0.3	119
10 deeper	9-27	-	-	-	2.1	0.1	47
10 shallower	9-27	-	-	-	7.1	0.4	162
5 thicker	9-27	-	-	-	5.2	0.3	118
5 thinner	9-27	-	-	-	3.1	0.2	70
true value	33-18	85.2	5.1	-	34.9	2.3	100
3 deeper	33-18	83.4	5.0	98	33.2	2.2	95
3 shallower	33-18	87.1	5.2	102	36.7	2.4	105
10 deeper	33-18	79.9	4.8	94	29.8	2.0	85
10 shallower	33-18	92.3	5.5	108	41.5	2.7	119
5 thicker	33-18	73.5	4.4	86	31.4	2.1	90
5 thinner	33-18	104.6	6.3	123	40.2	2.7	115
true value	18-12	93.6	3.6	-	25.8	1.6	100
3 deeper	18-12	91.4	3.5	98	24.5	1.6	95
3 shallower	18-12	95.9	3.6	102	27.2	1.7	105
10 deeper	18-12	87.2	3.3	93	21.9	1.4	85
10 shallower	18-12	102.2	3.9	109	31.0	2.0	120
5 thicker	18-12	77.1	2.9	82	22.5	1.4	87
5 thinner	18-12	130.9	5.0	140	32.6	2.1	126

### **Laser-ablation inductively coupled plasma mass spectrometry (LA-ICP-MS)**

Trace element- and REE concentrations have been determined by LA-ICP-MS at the University of Frankfurt am Main (Institute of Mineralogy) with a technical setting consisting of a Merchantek LUV213™ petrographic ultraviolet (UV) laser microprobe in conjunction with a Finnigan MAT ELEMENT2™ high-resolution ICP double-focusing mass spectrometer (HR-ICP-MS) for solid microsampling and geochemical analysis. The laser beam was set up to 30µ in diameter, which operates in ultra-violet modus (UV, at 213nm) using Q-switched UV laser energy of 2 mJ and a 5 Hz repetition rate. For accuracy international standard glasses were measured every ten samples. EMA derived silica concentrations were used as internal standards. Average precision and accuracy estimates based on replicate analyses of synthetic NIST standards reference material and USGS BCR-2 glasses are below 10% for most elements.

Table A-XIV: Trace element concentrations (ppm) of Fontana matrix glasses, determined by laser-ablation ICP-MS

Unit	Li7	Be9	B11	Si29	Ca44	Sc45	Rb85	Sr88	Y89	Zr90	Nb93	In115
D	16.06	1.03	22.15	247743	56741	27.24	31.83	340	20.29	84.24	3.29	0.09
D	12.74	0.65	17.78	247743	51302	22.09	29.60	263	16.91	81.37	2.64	0.12
D	11.61	0.62	15.82	247743	46996	19.05	29.06	231	13.68	72.06	2.42	0.10
D	9.45	0.56	12.55	247743	44755	15.04	26.99	185	11.21	70.25	1.81	0.06
E	11.87	0.86	16.92	247743	48709	20.46	29.53	243	15.52	76.71	2.39	0.10
E	12.03	0.78	19.02	247743	52584	24.67	29.49	297	18.32	80.24	2.86	0.09
E	13.12	1.01	20.02	247743	51999	22.76	29.53	278	17.31	79.97	2.64	0.09
E	11.71	0.69	16.95	247743	48938	20.21	29.06	245	15.15	75.81	2.25	0.09
F	11.90	0.48	16.30	247743	48659	19.65	28.66	242	14.96	79.68	2.45	0.08
F	11.45	0.68	16.41	247743	48169	19.08	28.38	233	14.37	77.15	2.26	0.09
F	11.09	0.67	13.91	247743	47932	19.76	28.20	244	15.27	78.92	2.36	0.10
F	14.53	0.96	20.01	247743	52957	23.57	30.82	290	18.19	81.99	2.81	0.09
G	12.23	0.83	17.75	247743	49253	21.41	28.16	265	16.15	77.62	2.59	0.07
G	11.25	0.54	17.04	247743	48469	19.61	28.64	246	14.69	75.28	2.37	0.07
G	14.59	0.86	22.64	247743	53741	25.22	31.17	306	18.99	80.44	2.91	0.09
G	12.66	0.73	20.83	247743	53662	24.15	29.62	298	18.32	80.66	2.77	0.09

Table A-XIV cont.

Unit	Cs133	Ba138	La139	Ce140	Pr141	Nd146	Sm147	Eu151	Gd158	Tb159	Dy161	Ho165
D	1.04	1097	10.90	26.45	3.57	15.85	3.79	1.27	3.72	0.52	3.52	0.78
D	0.86	844	8.65	19.89	2.75	12.17	2.95	0.93	2.82	0.43	2.82	0.62
D	0.81	770	7.73	18.27	2.40	10.64	2.68	0.83	2.52	0.36	2.35	0.50
D	0.62	622	6.21	14.41	1.94	8.49	2.11	0.65	1.87	0.28	1.81	0.40
E	0.81	801	8.41	19.14	2.76	11.65	3.19	0.90	2.84	0.41	2.75	0.59
E	0.95	936	9.77	23.18	3.14	14.38	3.43	1.07	3.13	0.49	2.93	0.62
E	0.80	881	9.05	20.99	2.94	12.23	3.03	0.94	2.96	0.43	2.86	0.58
E	0.79	779	7.96	18.38	2.54	11.23	2.74	0.88	2.63	0.40	2.68	0.54
F	0.75	785	8.01	18.46	2.61	11.73	2.85	0.81	2.75	0.44	2.70	0.60
F	0.76	759	7.73	17.88	2.47	11.12	2.79	0.81	2.42	0.40	2.39	0.50
F	0.81	762	7.85	17.65	2.49	11.53	2.92	0.93	2.80	0.43	2.75	0.57
F	0.92	925	9.54	22.28	3.03	13.60	3.31	0.99	3.25	0.48	3.20	0.63
G	0.83	841	8.71	20.07	2.82	12.56	3.19	0.98	3.21	0.47	2.96	0.63
G	0.83	779	7.96	18.42	2.51	11.00	2.66	0.84	2.46	0.37	2.59	0.54
G	0.88	982	10.07	23.85	3.17	13.94	3.44	1.11	3.11	0.49	3.23	0.70
G	0.84	932	9.67	22.28	3.07	13.52	3.28	1.03	2.91	0.47	3.02	0.64

Table A-XIV cont.

Unit	Er167	Tm169	Yb172	Lu175	Hf178	Ta181	Pb208	Th232	U238
D	2.29	0.31	2.37	0.32	2.10	0.18	125.25	1.73	1.77
D	1.82	0.27	1.74	0.27	1.93	0.15	105.58	1.40	1.28
D	1.52	0.22	1.57	0.22	1.77	0.73	146.47	1.22	1.23
D	1.22	0.18	1.24	0.18	1.72	0.09	15.61	1.02	0.93
E	1.90	0.24	1.95	0.27	1.92	0.17	321.37	1.37	1.29
E	1.98	0.29	1.99	0.30	1.93	0.16	351.96	1.56	1.42
E	1.78	0.29	1.90	0.30	1.96	0.15	54.19	1.50	1.36
E	1.68	0.24	1.65	0.24	1.79	0.19	106.23	1.32	1.17
F	1.72	0.24	1.76	0.26	1.96	0.15	110.88	1.36	1.20
F	1.47	0.23	1.65	0.24	1.83	0.15	160.48	1.30	1.16
F	1.74	0.24	1.64	0.26	2.02	0.18	117.44	1.34	1.19
F	1.98	0.30	1.99	0.30	2.03	0.16	15.00	1.56	1.49
G	1.90	0.25	1.90	0.27	2.00	0.21	60.27	1.47	1.36
G	1.57	0.24	1.65	0.23	1.82	0.14	39.72	1.30	1.21
G	2.31	0.31	2.24	0.31	2.06	0.17	357.15	1.58	1.55
G	1.90	0.30	2.00	0.30	2.03	0.21	142.06	1.53	1.40

Table A-XV: Major element composition (wt. %) of Fontana olivine phenocrysts, determined by EMA

Unit	SiO2	FeO	MnO	MgO	CaO	Cr2O3	NiO	Total
D	35.05	26.18	0.49	34.91	0.31	0.00	0.05	96.99
D	35.68	26.45	0.47	34.81	0.25	0.00	0.05	97.70
D	35.11	26.29	0.42	34.91	0.27	0.00	0.11	97.11
D	35.59	27.05	0.54	34.56	0.28	0.00	0.07	98.11
D	34.34	26.96	0.46	34.49	0.25	0.00	0.09	96.60
D	34.92	26.82	0.54	34.42	0.25	0.00	0.02	96.99
D	34.62	27.52	0.50	34.38	0.27	0.00	0.03	97.33
D	35.12	26.41	0.44	34.61	0.25	0.01	0.07	96.92
D	33.50	26.39	0.51	34.50	0.27	0.00	0.05	95.23
E	37.16	25.79	0.58	34.60	0.28	0.01	0.10	98.53
E	36.56	26.71	0.44	34.59	0.28	0.00	0.03	98.62
E	37.23	25.06	0.46	35.15	0.28	0.00	0.06	98.25
E	37.15	25.10	0.41	35.05	0.29	0.00	0.03	98.04
E	35.06	26.37	0.48	34.53	0.26	0.02	0.07	96.79
F	35.27	26.21	0.44	34.85	0.31	0.00	0.05	97.15
F	32.09	26.27	0.50	34.41	0.26	0.01	0.04	93.60
F	33.55	26.68	0.45	34.56	0.27	0.00	0.00	95.52
F	33.91	27.15	0.49	33.90	0.28	0.03	0.01	95.78
F	36.45	27.17	0.48	34.41	0.27	0.00	0.05	98.84
F	36.42	27.12	0.54	34.63	0.28	0.00	0.06	99.05
F	40.27	23.47	0.47	27.94	1.28	0.00	0.07	93.51
G	37.06	26.93	0.51	35.11	0.30	0.02	0.04	99.98
G	37.22	26.16	0.43	35.18	0.29	0.00	0.05	99.34
G	37.25	26.36	0.43	35.05	0.29	0.00	0.05	99.44
G	37.14	26.21	0.51	35.04	0.29	0.00	0.07	99.27
G	37.42	26.24	0.46	35.04	0.29	0.00	0.03	99.49
G	37.13	26.22	0.44	35.17	0.28	0.01	0.08	99.34
G	37.32	26.46	0.53	35.16	0.26	0.03	0.05	99.81
G	37.40	26.25	0.50	35.22	0.24	0.02	0.06	99.70
G	37.74	28.48	0.53	30.79	0.56	0.00	0.02	98.12
G	36.90	26.76	0.51	34.54	0.26	0.00	0.00	98.99
G	37.07	26.73	0.57	34.75	0.27	0.01	0.06	99.47
G	37.26	26.42	0.53	35.23	0.26	0.00	0.04	99.75
G	36.92	26.91	0.53	34.52	0.27	0.00	0.13	99.28
G	37.12	27.02	0.54	34.73	0.27	0.00	0.08	99.76
G	37.06	26.27	0.52	35.01	0.28	0.01	0.07	99.23



Table A-XVI: Major element composition (wt. %) of Fontana clinopyroxene phenocrysts, determined by EMA

Unit	SiO <sub>2</sub>	TiO <sub>2</sub>	Al <sub>2</sub> O <sub>3</sub>	FeO	MnO	MgO	CaO	Na <sub>2</sub> O	K <sub>2</sub> O	Cr <sub>2</sub> O <sub>3</sub>	NiO	Total
F	45.81	0.47	2.64	8.60	0.24	14.85	20.49	0.28	0.00	0.05	0.03	93.45
F	45.75	0.50	3.10	8.27	0.25	14.68	20.68	0.28	0.00	0.13	0.01	93.67
F	46.42	0.58	3.39	9.21	0.29	14.54	20.32	0.28	0.00	0.10	0.00	95.13
F	46.83	0.53	3.29	9.13	0.26	14.48	20.34	0.28	0.01	0.10	0.03	95.26
F	46.23	0.43	3.24	8.11	0.23	14.96	20.59	0.25	0.00	0.17	0.04	94.25
F	47.24	0.44	3.03	8.34	0.22	15.30	20.40	0.26	0.00	0.14	0.02	95.39
G	48.74	0.51	3.74	8.44	0.25	14.82	20.85	0.30	0.00	0.23	0.00	97.88
G	50.38	0.48	3.06	9.10	0.24	15.20	20.79	0.27	0.00	0.06	0.01	99.58
G	49.74	0.49	3.06	8.73	0.29	14.96	20.79	0.29	0.00	0.06	0.00	98.41
G	48.04	0.46	3.11	8.74	0.27	15.20	20.98	0.28	0.00	0.11	0.00	97.18
G	49.67	0.48	3.19	8.54	0.14	14.97	20.86	0.28	0.00	0.17	0.00	98.29

Table A-XVII: Major element composition (wt. %) of Fontana plagioclase phenocrysts, determined by EMA

Unit	SiO2	TiO2	Al2O3	FeO	MgO	CaO	Na2O	K2O	Total
D	47.09	0.06	31.14	0.87	0.12	16.75	1.91	0.05	97.99
D	47.39	0.04	30.81	1.01	0.13	16.23	2.18	0.07	97.86
D	48.89	0.06	30.39	1.01	0.12	15.53	2.74	0.10	98.82
D	47.76	0.08	31.48	1.03	0.13	16.42	2.26	0.11	99.27
D	47.82	0.09	31.13	0.91	0.13	16.54	2.18	0.11	98.91
D	49.07	0.08	30.08	0.99	0.15	15.22	2.77	0.11	98.46
D	48.10	0.07	30.79	1.03	0.15	16.14	2.28	0.10	98.65
D	47.10	0.02	30.74	0.96	0.13	16.03	2.21	0.08	97.27
E	48.23	0.05	31.79	0.89	0.12	16.78	2.33	0.11	100.30
E	47.47	0.06	31.95	0.96	0.10	17.34	1.94	0.08	99.90
E	48.60	0.03	31.36	0.94	0.13	16.54	2.44	0.13	100.18
E	48.14	0.01	31.56	1.04	0.12	16.66	2.31	0.10	99.94
E	47.09	0.03	31.98	0.98	0.12	17.46	1.85	0.07	99.60
E	47.58	0.04	31.47	0.87	0.11	16.65	2.13	0.08	98.92
E	47.99	0.06	31.19	0.92	0.13	16.62	2.28	0.12	99.31
E	48.02	0.04	31.25	0.89	0.13	16.47	2.28	0.09	99.17
E	47.72	0.03	31.06	0.84	0.14	16.49	2.17	0.09	98.53
F	46.34	0.03	31.13	1.14	0.12	17.20	1.78	0.09	97.83
F	47.95	0.03	30.03	0.84	0.13	16.26	2.43	0.11	97.79
F	46.15	0.03	31.55	0.83	0.10	17.71	1.76	0.07	98.20
F	47.87	0.02	29.35	0.95	0.09	15.63	2.65	0.14	96.69
F	47.89	0.03	30.04	0.97	0.11	16.01	2.47	0.13	97.66
F	47.46	0.04	30.16	0.92	0.11	16.33	2.35	0.11	97.49
F	46.28	0.04	29.85	0.88	0.12	16.65	2.08	0.07	95.98
F	46.34	0.02	30.73	0.79	0.11	17.13	1.82	0.06	97.00
F	45.43	0.02	29.85	0.81	0.12	16.90	1.98	0.07	95.19
F	49.76	0.05	28.63	0.84	0.15	14.64	3.32	0.15	97.55
F	48.28	0.03	29.17	0.88	0.12	15.20	2.78	0.12	96.59
G	47.01	0.04	33.33	1.04	0.11	17.42	1.89	0.10	100.94
G	48.25	0.02	32.70	0.98	0.13	16.76	2.33	0.11	101.28
G	47.15	0.05	33.18	0.86	0.11	17.55	2.02	0.08	101.01
G	46.96	0.02	33.47	0.91	0.12	17.64	1.77	0.09	100.99
G	48.64	0.07	32.15	0.95	0.14	16.42	2.57	0.13	101.06
G	47.38	0.03	33.25	0.96	0.13	17.45	2.09	0.08	101.38
G	47.38	0.08	33.18	0.96	0.13	17.46	1.98	0.09	101.25
G	47.31	0.05	33.35	0.90	0.15	17.25	1.94	0.09	101.04
G	47.64	0.04	33.00	0.91	0.12	17.00	2.13	0.10	100.96
G	47.71	0.04	32.87	0.96	0.11	16.95	2.21	0.13	100.97
G	48.23	0.05	32.63	0.91	0.12	16.46	2.31	0.10	100.80
G	48.67	0.01	32.05	0.79	0.12	15.74	2.63	0.11	100.12
G	49.38	0.03	31.70	0.90	0.14	15.59	2.77	0.13	100.64
G	49.02	0.00	31.94	0.95	0.13	15.81	2.69	0.13	100.67
G	47.46	0.06	33.12	1.03	0.13	17.05	1.96	0.10	100.91
G	49.36	0.05	31.56	0.93	0.13	15.52	2.81	0.13	100.49
G	48.66	0.05	32.02	0.98	0.11	16.26	2.41	0.12	100.62
G	49.58	0.04	31.64	0.86	0.14	15.77	2.75	0.16	100.94
G	49.16	0.03	31.73	0.87	0.15	15.59	2.72	0.13	100.38

## Acknowledgements

Several people were of great help during the course of this study, and I would like to express my gratitude:

- The mightiest thanks goes to my supervisor Armin Freundt, for his limitless enthusiasm, encouragement, and sprightly discussions
- Big thanks to the other members of the SFB's subproject C4: Hans-Ulrich Schmincke, Steffen Kutterolf, and Wendy Perez; for the exchange of and on flying tephra and cool times in the field, in the lab and in the office; I am also grateful to the other SFB C-project groups
- Cheers to Costanza Bonadonna and Bruce Houghton for productive and enjoyable collaboration in the field, and good discussions about Fontana's eruption physics
- Wilfried Strauch and the team of Ineter in Nicaragua for their support in field logistics
- Credit is due to all those who helped with the analytical work:
  - Dr. Michael Wiedenbeck and Ilona Schäpan for enabling the SIMS measurements at the GfZ Potsdam
  - Dr. Frank Lechtenberg of Hasylab in Hamburg for taming the SyXRF-instrument
  - Mario Thöner for the assistance with the electron microprobe at IfM-Geomar
  - Dagmar Rau, Jutta Heinze, and Michael Lange, the masters of IfM-Geomar's XRF and XRD machines
- And, for sure, strong thanks to all colleagues and friends who made this time a really enjoyable one, especially to Susi, Kristin, Matthias, Christian, Dietmar, Jörg, Sony, Jürgen, Noemi, Manu, Jens, Tobi, Ken
- To my parents, and to Felix and Jenni

Hiermit erkläre ich, dass ich die vorliegende Doktorarbeit selbständig erstellt und keine anderen als die angegebenen Hilfsmittel verwendet habe. Ferner habe ich weder diese noch eine ähnliche Arbeit an einer anderen Stelle im Rahmen eines Prüfungsverfahrens vorgelegt, veröffentlicht oder zur Veröffentlichung eingereicht.

Heidi Wehrmann

## **Lebenslauf**

### **Heidi Wehrmann**

Geb. am 09.08.1973  
in Hannover  
Staatsangehörigkeit: deutsch

- 1980 - 1993      Grundschule, Orientierungsstufe und Gymnasium in Wilhelmshaven;  
Abitur im Mai `93
- Okt.`94 - Feb.`98    Universität des Saarlandes, Saarbrücken;  
Studium der Physischen Geographie, Anthropogeographie und  
Geologie; Vordiplom im Okt `96
- Mär.`98 - Feb.`00    University of Waikato, Hamilton, New Zealand;  
Master of Science (Hons) in Earth Sciences (Volcanology), Feb.`00
- seit Okt.`01        IFM-GEOMAR, Christian-Albrechts Universität zu Kiel;  
Wissenschaftliche Angestellte im Sonderforschungsbereich 574